Fall 2015

Uncertainty quantification of turbulence model closure coefficients for transonic wall-bounded flows

John Anthony Schaefer

Department:

UNCERTAINTY QUANTIFICATION OF TURBULENCE MODEL CLOSURE COEFFICIENTS FOR TRANSONIC WALL-BOUNDED FLOWS

by

JOHN ANTHONY SCHAEFER

A THESIS

Presented to the Faculty of the Graduate School of the

MISSOURI UNIVERSITY OF SCIENCE AND TECHNOLOGY

In Partial Fulfillment of the Requirements for the Degree

MASTER OF SCIENCE

in

AEROSPACE ENGINEERING

2015

Approved by

Dr. Serhat Hosder, Advisor

Dr. David Riggins

Dr. Kakkattukuzhy Isaac

ABSTRACT

The goal of this work was to quantify the uncertainty and sensitivity of commonly used turbulence models in Reynolds-Averaged Navier-Stokes codes due to uncertainty in the values of closure coefficients for transonic, wall-bounded flows and to rank the contribution of each coefficient to uncertainty in various output flow quantities of interest. Specifically, uncertainty quantification of turbulence model closure coefficients was performed for transonic flow over an axisymmetric bump at zero degrees angle of attack and the RAE 2822 transonic airfoil at a lift coefficient of 0.744. Three turbulence models were considered: the Spalart-Allmaras Model, Wilcox (2006) k-ω Model, and the Menter Shear-Stress Transport Model. The FUN3D code developed by NASA Langley Research Center and the BCFD code developed by The Boeing Company were used as the flow solvers. The uncertainty quantification analysis employed stochastic expansions based on non-intrusive polynomial chaos as an efficient means of uncertainty propagation. Several integrated and point-quantities are considered as uncertain outputs for both CFD problems. All closure coefficients were treated as epistemic uncertain variables represented with intervals. Sobol indices were used to rank the relative contributions of each closure coefficient to the total uncertainty in the output quantities of interest. Two studies were performed in this work. The main study identified a number of closure coefficients for each turbulence model for which more information will reduce the amount of uncertainty in the output significantly for transonic, wall-bounded flows. A case study demonstrated that the RAE 2822 sensitivity results of the main study are independent of the flow solver and of the computational grid topology and resolution.

ACKNOWLEDGMENTS

I would like to thank my advisor, Dr. Serhat Hosder, for his support and guidance throughout my time as a graduate student. He has always pushed me to do my best work, and he has provided me with the opportunities necessary to pursue my career goals.

I would also like to thank my committee members, Dr. David Riggins and Dr. Kakkattukuzhy Isaac for their time, instruction, and dedication towards this work.

I am very grateful for my funding support, which was provided by the Missouri S&T MAE Department, the Missouri S&T Chancellor's Fellowship Program, and NASA Grant NNX14AN17A (technical monitor: Mujeeb Malik).

Additionally, I would like to thank Bil Kleb, Jan Carlson, and Chris Rumsey of the NASA Langley Research Center for providing me with a fulfilling and rewarding internship experience. This research would not have begun or progressed successfully without their help. I would also like to thank Mori Mani, Josh Krakos, Andrew Cary, and Jason Walton of The Boeing Company for their support as I continued my graduate research on a second internship under their guidance.

Furthermore, I would like to thank Philippe Spalart, David Wilcox, Florian Menter, and Gary Coleman for their contributions to the epistemic intervals in this research. None of the results in this work would be meaningful without their contributions.

Finally, I would like to thank my family and friends for their love and support. In particular I would like to thank Tom West, Andrew Brune, Joe Gramanzini, and Harsheel Shah for their camaraderie as my fellow graduate students.

TABLE OF CONTENTS

LIST OF ILLUSTRATIONS

LIST OF TABLES

NOMENCLATURE

Symbol	Description
C_D	Drag Coefficient
C_L	Lift Coefficient
C_p	Pressure Coefficient
C_f	Skin Friction Coefficient
M	Mach Number
Re	Reynolds Number
T	Temperature
n	Number of Uncertain Variables
n_p	Oversampling Ratio
N_s	Total Number of Samples
p	Order of Response Surface Polynomial
$C_{D_{\text{press}}}$	Drag Coefficient due to Pressure
$C_{D_{\text{sf}}}$	Drag Coefficient due to Skin Friction
u	Velocity
ρ	Density
ν	Molecular Kinematic Viscosity
ν_t	Turbulent Kinematic Viscosity
μ	Molecular Dynamic Viscosity
μ_t	Turbulent Eddy Viscosity
d	Distance from Field Point to Nearest Wall
Ω	Vorticity Magnitude
α^*	Stochastic Response Function
α_i	Deterministic Component of α^*

Ψ_i	Random Variable Basis Functions of α^*
$\boldsymbol{x}$	Deterministic Vector
$\boldsymbol{\xi}$	Random Variable Vector
D	Total Variance
$S_{i_1 \ldots i_s}$	Sobol indices
$\sigma,\quad \kappa,\quad c_{b1},\quad c_{b2}$ $c_{v1},\quad c_{w2},\quad c_{w3},\quad c_{t1}$ $c_{t2},\quad c_{t3},\quad c_{t4}$	SA Closure Coefficients
$\sigma_k,\quad \sigma_w,\quad \beta^*,\quad \beta_0$ $\sigma_{do},\quad C_{lim},\quad \kappa$	W2006 Closure Coefficients
$\sigma_{k1},\quad \sigma_{w1},\quad \beta_1,\quad \beta_2$ $\beta^*,\quad \sigma_{k2},\quad \sigma_{w2},\quad \kappa$ a_1	SST Closure Coefficients

1. INTRODUCTION

This chapter outlines the research presented in this work. First, a introduction to turbulence modeling is provided, which is followed by an overview of uncertainty quantification. Next, a literature review discussing previous turbulence modeling research and uncertainty quantification approaches is presented. The objectives of the current work are then given, and subsequently the contributions of the current work are described. Finally an outline for the remainder of the thesis is provided.

1.1. TURBULENCE MODELING

Turbulence is one of the greatest unsolved mysteries of classical physics. Due to the highly complex and chaotic nature of the phenomenon, the current physical understanding of turbulence is incomplete. Efforts have been made to create turbulence models to predict turbulent flows by using computational fluid dynamics (CFD); however, the lack of physical knowledge has forced modelers to use dimensional analysis and other methods to identify several constants, called closure coefficients, which balance the model equations. The numerical values of the closure coefficients in current turbulence models are chosen by using a combination of heuristic and empirical decision making. While modelers typically use experimental data to validate their choice of closure coefficients, a turbulence model is not guaranteed to be universally valid for any arbitrary flow.

1.2. UNCERTAINTY QUANTIFICATION

Turbulence modeling is one of the primary sources of uncertainty in CFD simulations. Uncertainties in both the model form and the values of closure coefficients can yield large uncertainties in output flow quantities of interest (such as

drag coefficient, for example). This work aims to explore the second aforementioned source of uncertainty; that is, uncertainty in the output flow quantities due to uncertainty in the values of closure coefficients.

To minimize the large computational expense associated with uncertainty quantification (UQ) of high-fidelity CFD simulations with traditional sampling methods (e.g., Monte Carlo), stochastic expansions based on non-intrusive polynomial chaos (NIPC) are used as an efficient means of uncertainty propagation in this work [2]. All closure coefficients were treated as epistemic uncertain variables (i.e., uncertainty due to lack of knowledge and not due to inherent, systemic uncertainty). Sobol indices [3], which are global nonlinear sensitivity indices based on variance decomposition, were used to rank the relative contributions of each closure coefficient to the total uncertainty in the output quantities of interest. The uncertainty quantification methods employed in this work are described in detail in Chapter 4.

1.3. LITERATURE REVIEW

This section contains a literature review of previous research related to UQ and turbulence modeling. In Section 1.3.1, the demand for uncertainty quantification and sensitivity analysis of turbulence modeling is described. Several previous examples of UQ for CFD applications using stochastic expansions are presented in Section 1.3.2. Some applications of Bayesian approaches to UQ for turbulence modeling are included in Section 1.3.3. Finally a brief discussion of verification and validation is included in Section 1.3.4.

1.3.1. Demand for UQ in CFD. There is currently a high demand for turbulence modeling uncertainty quantification and sensitivity analysis. In a coordinated study between NASA, Boeing, and others, Slotnick et al. propose a vision for the capabilities of CFD technology in the year 2030, as well as a number of suggestions for how to reach that point [4]. One of the basic capabilities for the

authors' vision of CFD in 2030 includes, among other things, the management of errors and uncertainties arising from "all possible sources." These sources include physical modeling errors and uncertainties due to turbulence, as well as epistemic uncertainties due to lack of knowledge in the parameters of particular fluid flow problems. Another section of the report states that in practice, current CFD workflows contain considerable uncertainty that is often not quantified. While grid convergence studies can be performed to reduce numerical uncertainty, they can be difficult to perform because uniform mesh refinement can be too costly for most 3D problems. Accurate prediction of turbulent flows and the currently limited use of uncertainty quantification are both listed as current CFD technology gaps and impediments. The former is described as "perhaps the single, most critical area in CFD simulation capability." Slotnick et al. present four "Grand Challenge" problems for CFD, one of which is a probabilistic analysis of a powered space access configuration, including error estimates and quantified uncertainty. One of the authors' immediate recommendations is to integrate NIPC methods and other reduced-order model formulations with current CFD technology.

Some previous work has been done on this problem. Godfrey and Cliff [5] employed the sensitivity-equation method to quantify the sensitivities of the Baldwin-Lomax, Spalart-Allmaras, and Wilcox k-ω turbulence models due to modeling coefficients; however they did not quantify the uncertainty in the results. They found that σ_w is more influential to the k-ω model than σ_k (using the NASA Turbulence Modeling Resource Page [1] nomenclature), and that the most influential parameters in the Spalart-Allmaras model are c_{v1}, c_{b1}, σ, and c_{w2} when κ is held constant. Hosder et al. [6] quantified the uncertainty in nozzle efficiency for a transonic diffuser problem; however this uncertainty was due to the choice of pressure ratios, computational grids, flux limiters, and turbulence models (i.e., uncertainty in nozzle efficiency due to the

choice of either the SA or k-ω model, not due to the uncertainty in the turbulence models themselves). More work is needed to adequately address the demands of CFD Vision 2030 above.

1.3.2. UQ of CFD using Stochastic Expansions. It was demonstrated by Hosder et al. [2] that stochastic expansions based on Non-Intrusive Polynomial Chaos (NIPC) are capable of producing the same uncertainty and sensitivity information as crude Monte Carlo simulations, but at a greatly reduced computational cost. This makes NIPC very attractive for CFD applications, where the computational cost of every function evaluation may be high. One recent application of uncertainty quantification to CFD was by West and Hosder [7]. In their work, West and Hosder demonstrated an application of Point-Collocation Non-Intrusive Polynomial Chaos (NIPC) with sparse sampling as an efficient means of uncertainty propagation for both a stagnation point, convective heat transfer in hypersonic flow and a hypersonic inflatable aerodynamic decelerator during Mars entry. Their analysis consisted of 93 uncertain parameters, the sources of which include both flowfield and radiation modeling. Another application of uncertainty quantification to CFD was by Adya et al. [8]. In this work, the NIPC method was applied to the uncertainty quantification of the downstream velocity profile for a synthetic jet actuator due to uncertainties in the amplitude and frequency of the oscillation of the piezo-electric membrane used to produce the jet. In a third analysis by Hosder et al. [9], NIPC was applied to the uncertainty quantification of a transonic wing damping factor due to uncertainties in the Mach number and angle of attack. For more examples of how uncertainty quantification and polynomial chaos techniques have been used in CFD, see the review by Najm [10]. Further details on polynomial chaos theory are given by Ghanem [11] and Eldred [12].

1.3.3. UQ of Turbulence Modeling using Bayesian Approaches. Uncertainty quantification has a very important application to turbulence modeling in CFD. In a recent work by Edeling et al. [13], the authors state that "The turbulence closure model is the dominant source of error in most Reynolds Averaged Navier-Stokes simulations, yet no reliable estimators for this error component currently exist." Furthermore, "there is no consensus on the best coefficient values for most [turbulence] models, as evidenced by the wide range of coefficients seen in the literature." Current efforts to address these concerns employ Bayesian approaches. Edeling et al. describe a stochastic error estimate of turbulence models based on variability in model coefficients. Using Bayesian Model-Scenario Averaging, a stochastic estimate of the output quantities of interest in unmeasured (prediction) scenarios is obtained. In a sensitivity analysis, it was demonstrated that Von Kármán's constant was the most influential model coefficient to uncertainty in u^+ in the log layer of a flat plate boundary layer for several turbulence models; these models included, among others, the Spalart-Allmaras and Wilcox k-ω models. For almost all prediction cases, the predictions lied within one standard deviation of the experimental validation data.

Papadimitriou and Papadimitriou [14] also performed uncertainty quantification of turbulence modeling using a Bayesian approach. In their study, Papadimitriou and Papadimitriou employed Bayesian inference framework and analytical approximations to quantify the uncertainty of the Spalart-Allmaras turbulence model due to uncertainty in its closure coefficients. Specifically, this technique was applied to a flat plate and a backwards facing step problem. They determined that the most well informed parameters for the Bayesian inference were κ, c_{v1}, and c_{b1}, followed next by c_{w2} and σ. This indicates that these coefficients contribute most significantly to uncertainty in the Spalart-Allmaras model for the chosen output quantities of interest.

1.3.4. Verification and Validation. As stated by Slotnick et al. [4], "Verification is defined as the determination of whether a model is implemented correctly, whereas validation is defined as the determination of how well the model represents physical reality." Verification and validation (V&V) are not the main focus of this work, but it should be noted that uncertainty quantification and sensitivity results for turbulence models are both integral components of validation efforts. Extensive V&V studies have already been performed for CFD [1], [15], however they have mostly lacked uncertainty quantification and sensitivity analyses of turbulence models.

1.4. OBJECTIVES OF THE CURRENT WORK

Two studies were performed for this work: a main study, and a case study that expands on the results of the main study. The objectives of these studies are described in this section.

1.4.1. Objectives of Main Study. The goal of the main study was to quantify the uncertainty and sensitivity of commonly used turbulence models in Reynolds-Averaged Navier-Stokes (RANS) codes due to uncertainty in the values of closure coefficients for transonic, wall-bounded flows and to rank the contribution of each coefficient to uncertainty in various output flow quantities of interest. Specifically, three turbulence models are considered: the Spalart-Allmaras One-Equation Model (SA) [16], the Wilcox (2006) k-ω Two-Equation Model (W2006) [17], and the Menter Shear-Stress Transport Two-Equation Model (SST) [18]. Each model features its own unique set of closure coefficients, which are discussed further in Chapter 3.

FUN3D, an unstructured RANS code of NASA Langley Research Center (LaRC), was chosen as the flow solver for all simulations in the main study [19]. More information about FUN3D is included in Section 2.1. Two CFD problems are

considered in the main study. The first is an axisymmetric, transonic bump validation case from Bachalo and Johnson [20], which is discussed in detail in Section 2.3. The second CFD problem is the RAE 2822 transonic airfoil, which is discussed in detail in Section 2.4.

Uncertainty in the output quantities of interest was quantified by epistemic intervals using Point-Collocation NIPC. For example, the uncertainty in drag coefficient was quantified by the minimum and maximum response surface values calculated using NIPC. Sensitivity information was quantified by Sobol indices. These global nonlinear sensitivity indices allow for direct comparison and ranking of the effect that uncertainty in the values of closure coefficients has on the uncertainty in output flow quantities of interest.

1.4.2. Objectives of Case Study. The objective of the case study was to verify the RAE 2822 results of the main study using new computational grids of varying resolution and topology, as well as an additional flow solver. The results of computational fluid dynamics simulations can be grid-dependent, so it is common practice to perform grid studies to demonstrate grid-independence of the results. Different flow solvers are also known to sometimes produce different results. In addition to FUN3D, the Boeing-developed BCFD code was chosen as an additional RANS flow solver for the case study. More information about BCFD is included in Section 2.2.

1.5. CONTRIBUTIONS OF THE CURRENT WORK

This work has several contributions. First, it quantifies the uncertainty in CFD simulations due to uncertainty in turbulence model closure coefficients. A deterministic CFD simulation produces a single value for a given output, but there is no quantifiable measure of confidence in that value. The stochastic approach here produces a range of all possible values due to the uncertainty in the turbulence

model. In a research setting, this range can be used to determine the robustness of a turbulence model, and whether or not efforts should be made to improve the model in some way. In a design setting, it may be desirable to reduce this range, or else design a factor of safety around it. In a commercial setting, this range could be used in a cost analysis (e.g., uncertainty in drag coefficient will affect projected fuel costs).

A second contribution of this work is the quantification of sensitivity information. The turbulence modeling community has long recognized the existence of uncertainty in turbulence models, but with an overwhelming amount of sources of uncertainty it has been difficult to make a targeted attempt to reduce each model's uncertainty. The sensitivity information presented in this work demonstrates that most of the uncertainty in each turbulence model is only due to a small subset of the model's coefficients. Reducing the uncertainty in the values of the coefficients in these subsets will greatly reduce the total uncertainty of each turbulence model. The sensitivity information is valuable because it provides a guide for how resources should be invested (whether through experimentation, LES/DES, etc.) to reduce the uncertainty in turbulence models due to the uncertainty in the values of their closure coefficients. This information could also be used to aid the validation efforts discussed in Section 1.3.4.

This work serves to bridge the gap between UQ of CFD using stochastic expansions (Section 1.3.2) and UQ of turbulence modeling using Bayesian approaches (Section 1.3.3). The uncertainty quantification approach of the former has been very successful, however it has not yet been applied to turbulence modeling. The approach of the latter has also seen success, however it relies heavily upon experimental or Direct Numerical Simulation (DNS) data for the Bayesian model calibration (i.e., it cannot be applied to a new problem for which no experimental or DNS data is available). Furthermore, in the studies discussed in Section 1.3.3, the authors

assumed uniform probability density functions (PDFs) for each closure coefficient with lower and upper bounds of plus or minus some percentage of the baseline coefficient value. This approach is arbitrary and often ignores physical or experimental evidence suggesting the invalidity of the chosen distributions, effectively biasing the uncertainty quantification and sensitivity results. In this work, the intervals for all model coefficients were informed by experimental or numerical results, or else by the turbulence modelers themselves. These intervals are discussed in detail in Chapter 3.

1.6. THESIS OUTLINE

This thesis is broken down into several chapters. In Chapter 2, the flow solvers and CFD problems are discussed. The turbulence models used in this work are described in Chapter 3. Next, in Chapter 4 an overview of the uncertainty quantification approach is presented. The results of the main study and the case study are included in Chapters 5 and 6 respectively. Finally in Chapter 7, conclusions are made and some suggestions for future work are presented.

2. FLOW SOLVERS AND CFD PROBLEMS

Two flow solvers were employed in this work: FUN3D and BCFD. The details of each solver are provided in Sections 2.1 and 2.2 respectively. Next, information is given for the freestream conditions and computational grids of the axisymmetric transonic bump and RAE 2822 airfoil CFD problems.

2.1. FUN3D

The primary flow solver used in this work was a modified form of FUN3D version 12.4 [19]. FUN3D is an unstructured, node-based, three-dimensional, finite-volume RANS code capable of solving steady and unsteady laminar or turbulent flows with subsonic to hypersonic speeds. The modifications to the code were performed to allow changes to the values of turbulence model closure coefficients in the uncertainty analyses. All solutions used a Roe, second-order flux differencing scheme with second-order spatial accuracy for the viscous terms. The CFL numbers for the mean flow and turbulence model equations were ramped from 10 to 50 and from 5 to 30, respectively, across 500 iterations, and then the CFL numbers were fixed at their maximum values until steady-state convergence was achieved. All of the results in the main study were obtained using FUN3D. In the case study, results were obtained using FUN3D for all three turbulence models with the coarse, fine, med-tri, and unstr-m grids.

2.2. BCFD

The second flow solver used in this work was a modifed form of BCFD alpha version 8.0. The modifications to the code were performed to allow changes to the values of the SA turbulence model closure coefficients in the uncertainty analyses. Baseline solutions for each grid were obtained in the following manner: First, the solver was run in laminar mode for 250 iterations; next, the laminar solution was

restarted using a first order flux differencing scheme and run for 500 iterations; finally, the first order solution was restarted using a HLLE++, second order flux differencing scheme with second-order spacial accuracy for the viscous terms, and it was run until steady-state convergence was achieved. Subsequent cases for each grid were restarted from the converged baseline solution. The CFL number was allowed to automatically adjust for improved convergence time, with a maximum allowable value of 500. BCFD was not used in the main study. In the case study, results were obtained using BCFD for the SA model with the original medium, unstr-m, and unstr-f grids.

2.3. PROBLEM 1: AXISYMMETRIC TRANSONIC BUMP

The first CFD problem considered in this work is an axisymmetric transonic bump validation case from Bachalo and Johnson [20]. The test article in the experiment consisted of a thin-walled cylinder that extended 61 cm upstream of the bump's leading edge, and the cylinder had an outside diameter of 15.2 cm with a bump chord of 20.32 cm. The flow has freestream $M = 0.875$, $T = 540^\circ$ R, and $Re = 2.763 \times 10^6$ (based on the bump length of $c = 1$). All flow solutions were obtained by using the 721 x 321 grid from the NASA Langley Research Center turbulence modeling resource website [1]. The mesh contains 462,882 nodes, 1,155,121 edges, and 230,400 hexahedral cells. It consists of a 1° wedge rotated about the x-axis. The sides of the mesh are treated as periodic interfaces; they are periodic with each other and rotated through 1° in order to simulate axisymmetry. The normal wall distance is 6×10^{-6} grid units, and the minimum and maximum y^+ values on the bump surface are 0.045 and 0.590 respectively (calculated from the baseline solution with the Spalart-Allmaras model). The surface of the bump and cylinder has a solid wall boundary condition, and all other boundary conditions are farfield Riemann. A graphical overview of the axisymmetric transonic bump problem is included in

Fig. 2.1. The circles below the mesh in the figure represent the axisymmetry about the x-axis. An example pressure contour plot is included in Fig. 2.2 for the transonic bump case obtained with the SA baseline model.

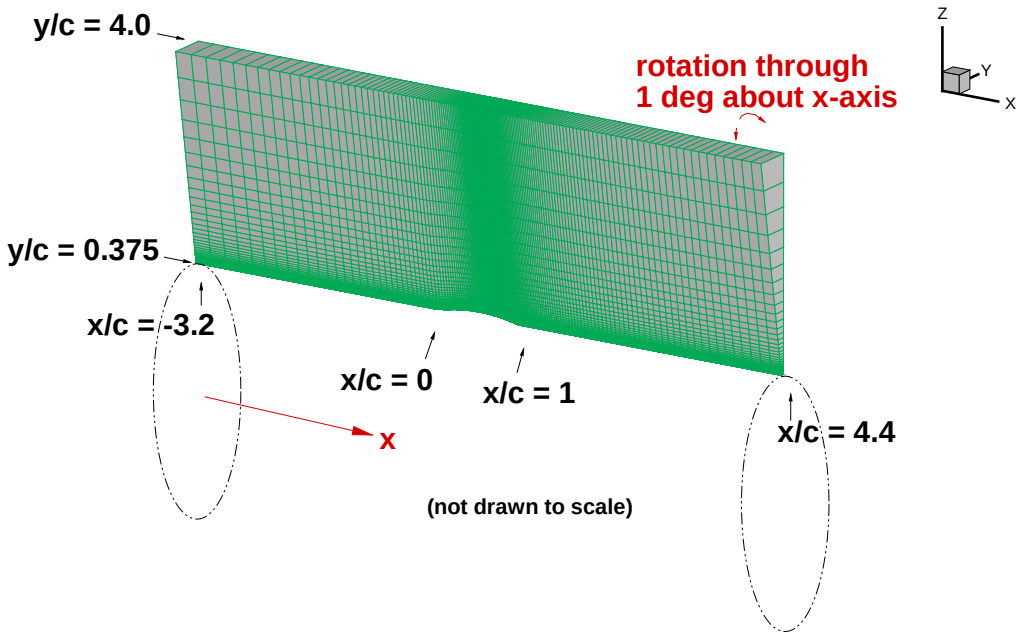

Figure 2.1: Axisymmetric transonic bump overview from Ref. 1.

2.4. PROBLEM 2: RAE 2822 TRANSONIC AIRFOIL

The second CFD problem considered in this work is the RAE 2822 transonic airfoil at a lift coefficient of 0.744. The experimental data for this case is from Cook et al [21]. The flow has freestream $M = 0.729$, $T = 540°$ R, and $Re = 6.5 \times 10^6$ (based on the airfoil chord of $c = 1$). Numerical integration of the experimental pressure coefficient data yields a lift coefficient of $C_L = 0.744$; the angle of attack was adjusted for each baseline turbulence model to match this value, and all subsequent

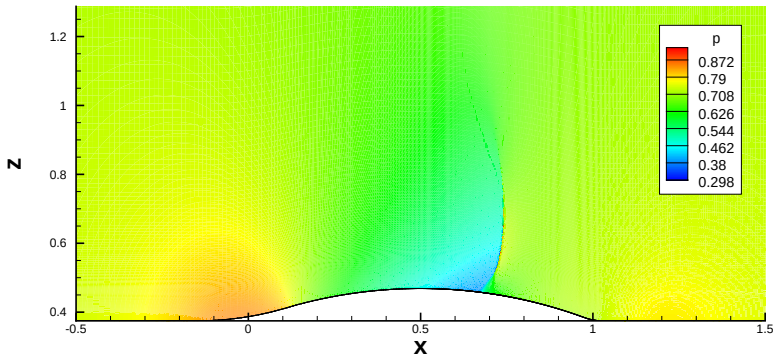

Figure 2.2: Non-dimensional pressure contours (scaled with the maximum value) of axisymmetric transonic bump.

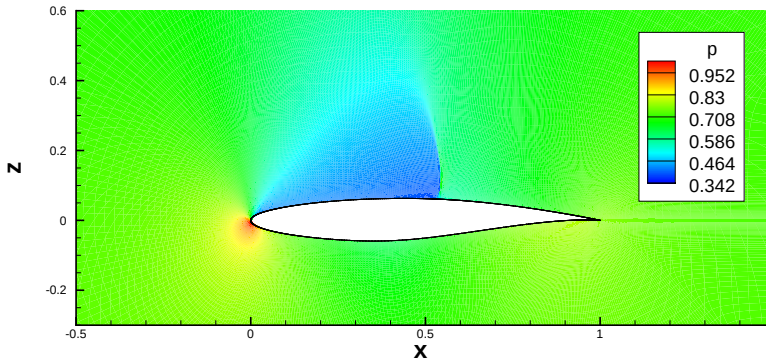

Figure 2.3: Non-dimensional pressure contours (scaled with the maximum value) of RAE 2822 airfoil.

simulations for each model used the same angle of attack as the one found for the baseline. An example pressure contour plot for the RAE 2822 is included in Fig. 2.3, which was obtained with the SA baseline model.

The RAE 2822 flow solutions in the main study were obtained by using a 513 x 161 grid containing 206,272 nodes, 514,208 edges, and 102,400 hexahedral cells. The grid used in the main study (hereafter referred to as the "original medium grid") is a 2D C-mesh extruded one unit in the y-direction with y-symmetry boundary

conditions on either side and with a solid wall boundary condition on the airfoil surface. All other boundary conditions are farfield Riemann. The original medium grid started as a structured PLOT3D grid, and it was converted to the unstructured AFLR3 format for use in FUN3D and BCFD.

Five additional grids were generated based on the original medium grid. These include a coarse grid, a fine grid, a tri-diagonalized medium grid, and two new unstructured grids. All of the additional grids were created using MADCAP, a grid generation software developed by The Boeing Company.

The coarse grid was created by coarsening the original medium grid by one level. It employs the same geometry definition, but with every other point skipped. The coarse grid contains 51,936 nodes, 129,104 edges, and 25,600 hexahedral cells.

The fine grid was created by refining the original medium grid by one level. It employs the same geometry definition, but with new points spaced halfway between each of the original points on the wall. The fine grid contains 822,144 nodes, 2,052,416 edges, and 409,600 hexahedral cells.

The tri-diagonalized medium grid (hereafter referred to as "med-tri") was created by splitting all of the quadralaterals on one 2D face of the original medium grid into triangles, and then re-extruding by one grid unit. The extrusion results in a grid consisting of all prism cells, as opposed to the previous grids which consist of hexahedral cells. The med-tri grid employs the same geometry definition as the original medium grid. Wall spacing was kept the same at 5×10^{-6} grid units. The med-tri grid contains 206,272 nodes, 719,008 edges, and 204,800 prism cells.

The first unstructured grid (hereafter referred to as "unstr-m") employs the same geometry definition as the original medium grid. It consists of hexahedral cells near the wall and prism cells further away. Wall spacing was kept the same at 5×10^{-6} grid units. The unstr-m grid consists of 120,866 nodes, 353,179 edges, 34,270 hexahedral cells, and 51,670 prism cells.

The second unstructured grid (hereafter referred to as "unstr-f") employs the same geometry definition as the fine grid. Like unstr-m, unstr-f consists of hexahedral cells near the wall and prism cells further away. Wall spacing was halved to 2.5×10^{-6} grid units. The unstr-f grid consists of 220,778 nodes, 630,333 edges, 70,027 hexahedral cells, and 79,556 prism cells.

A summary of the grids is presented in Table 2.1. The normal wall distance (in grid units), $y^+_{\min}$, and $y^+_{\max}$ are included in Table 2.2. The values of y^+ were determined from baseline solutions with the Spalart-Allmaras model at the first grid point off the wall. Images of the RAE 2822 grids are included in Figs. 2.4 and 2.5.

Table 2.1: Summary of RAE 2822 computational grids.

Grid	Nodes	Edges	Hex. Cells	Prism Cells	Total Cells
Original Medium	206,272	514,208	102,400	0	102,400
Coarse	51,936	129,104	25,600	0	25,600
Fine	822,144	2,052,416	409,600	0	409,600
Med-Tri	206,272	719,008	0	204,800	204,800
Unstr-m	120,866	353,179	34,270	51,670	85,940
Unstr-f	220,778	630,333	70,027	79,556	149,583

Table 2.2: RAE 2822 grid wall spacing information.

Grid	Normal Wall Distance	$y^+_{\min}$	$y^+_{\max}$
Original Medium	5.0×10^{-6}	0.185	2.016
Coarse	1.0×10^{-5}	0.440	4.153
Fine	2.5×10^{-6}	0.078	1.016
Med-Tri	5.0×10^{-6}	0.082	2.066
Unstr-m	5.0×10^{-6}	0.167	2.014
Unstr-f	2.5×10^{-6}	0.085	1.039

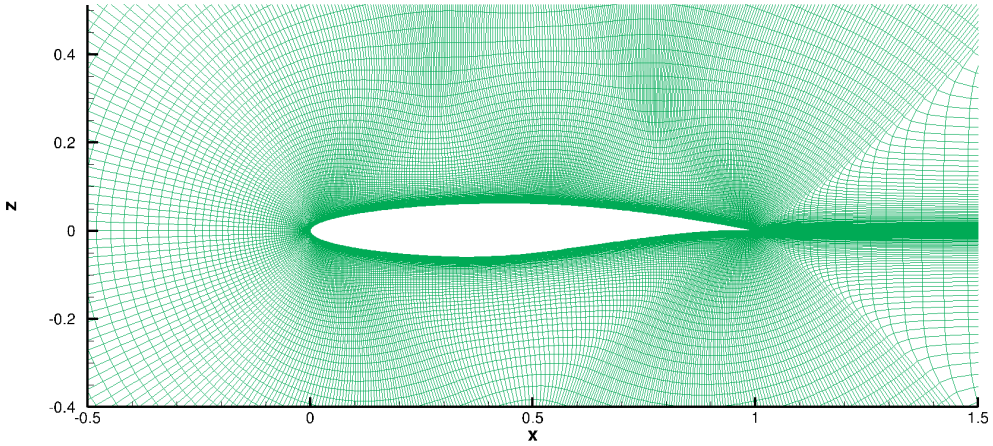

(a) Original medium grid

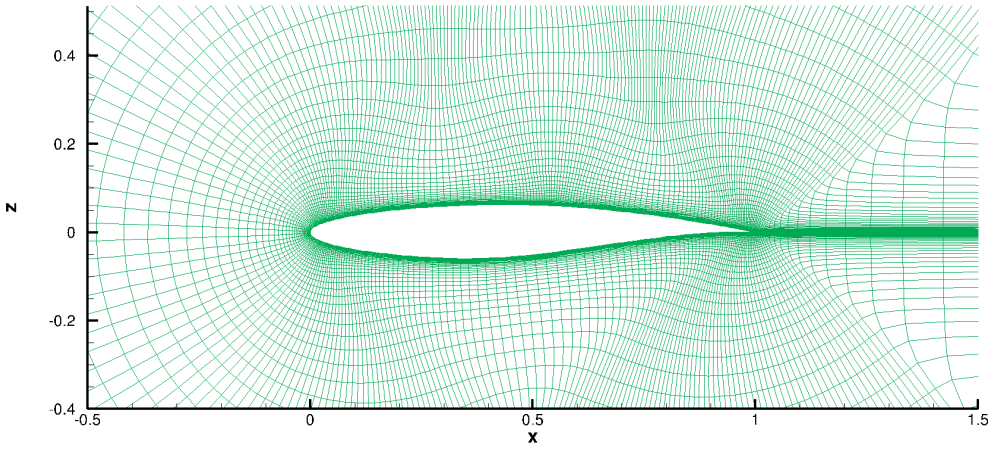

(b) Coarse grid

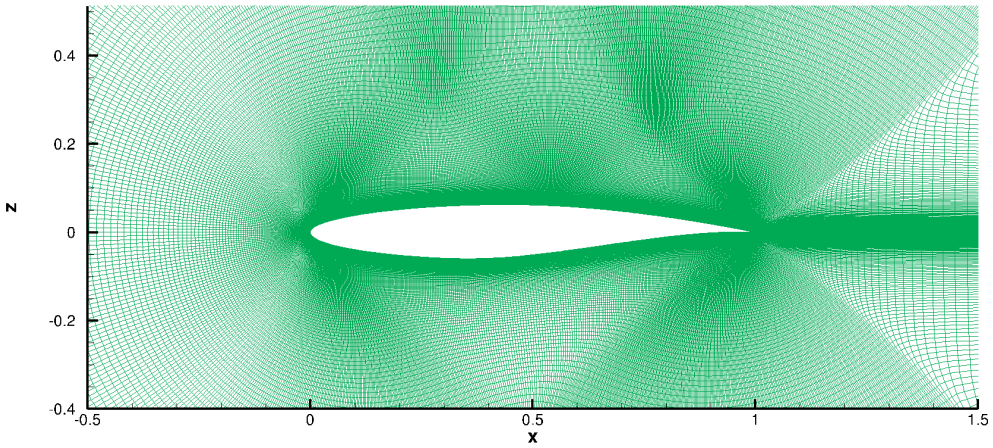

(c) Fine grid

Figure 2.4: Computational grids for RAE 2822 airfoil (orig. med., coarse, and fine).

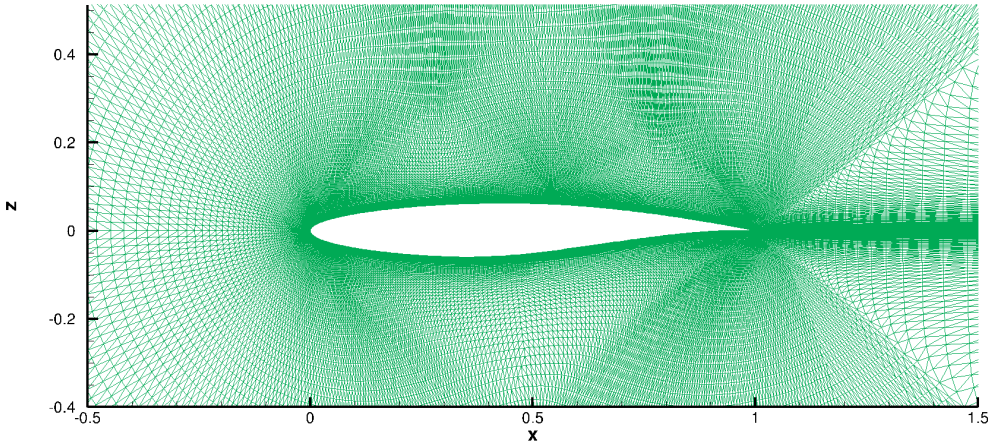

(a) Med-tri grid

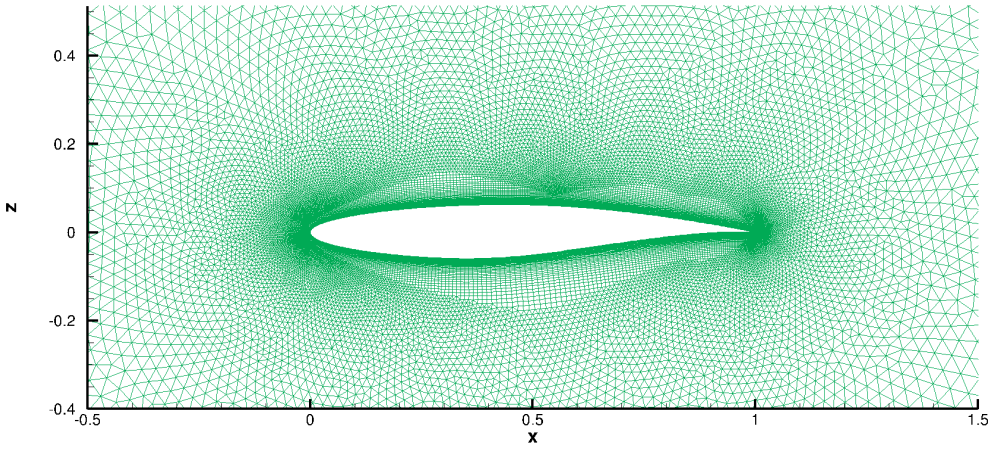

(b) Unstr-m grid

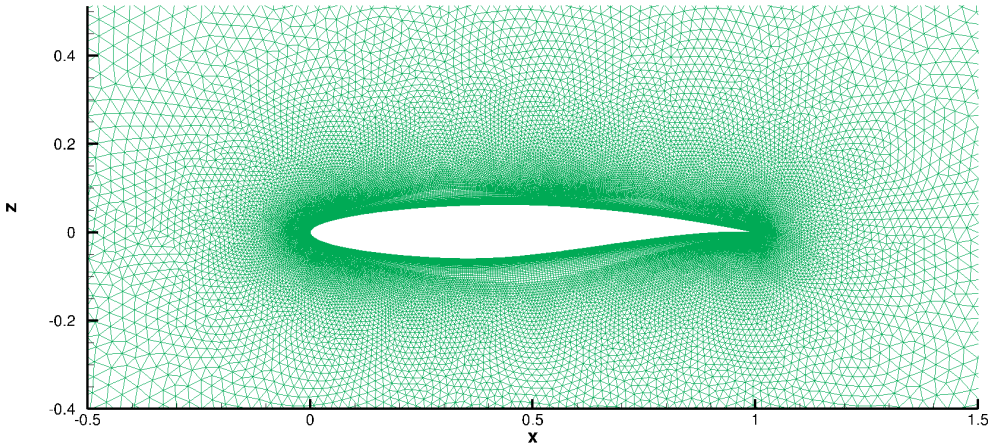

(c) Unstr-f grid

Figure 2.5: Computational grids for RAE 2822 airfoil (med-tri, unstr-m, and unstr-f).

3. TURBULENCE MODELS

In this chapter, the details of the turbulence models employed in this work are outlined. Each section contains an overview of a turbulence model, its closure coefficient values, and estimates of the epistemic intervals for each closure coefficient. Note that the two-equation turbulence model equations are written in conserved variable form, but the flow solutions are calculated with primitive variable form in FUN3D. Also note that in this work, the nomenclature from the NASA LaRC turbulence modeling website [1] is used.

3.1. SPALART-ALLMARAS ONE-EQUATION MODEL (SA)

The SA model was developed as an evolution of the Nee-Kovasznay model [22], but with several near-wall and compressibility corrections [16]. It is simpler, less computationally expensive, and more computationally robust than multi-equation models, and it is widely used for aerodynamic flows in engineering applications. The model is given by

$$\begin{aligned}\frac{\partial \hat{\nu}}{\partial t} + u_j \frac{\partial \hat{\nu}}{\partial x_j} = c_{b1}\left(1 - f_{t2}\right)\hat{S}\hat{\nu} - \left[c_{w1} f_w - \frac{c_{b1}}{\kappa^2} f_{t2}\right]\left(\frac{\hat{\nu}}{d}\right)^2 \\ + \frac{1}{\sigma}\left[\frac{\partial}{\partial x_j}\left(\left(\nu + \hat{\nu}\right)\frac{\partial \hat{\nu}}{\partial x_j}\right) + c_{b2}\frac{\partial \hat{\nu}}{\partial x_i}\frac{\partial \hat{\nu}}{\partial x_i}\right]\end{aligned} \tag{1}$$

The full formulation of the model is given by Spalart and Allmaras [16]. The closure coefficients and their suggested values are given in Table 3.1. The closure coefficients also include

$$c_{w1} = \frac{c_{b1}}{\kappa^2} + \frac{1 + c_{b2}}{\sigma} \tag{2}$$

The turbulent eddy viscosity is computed from:

$$\mu_t = \rho\hat{\nu} f_{v1} \tag{3}$$

where

$$f_{v1} = \frac{\chi^3}{\chi^3 + c_{v1}^3}, \quad \chi = \frac{\hat{\nu}}{\nu} \tag{4}$$

and ρ is the density, $\nu = \mu/\rho$ is the molecular kinematic viscosity, and μ is the molecular dynamic viscosity. Additional definitions are given by the following equations:

$$\hat{S} = \Omega + \frac{\hat{\nu}}{\kappa^2 d^2} f_{\nu 2} \tag{5}$$

where $\Omega = \sqrt{2W_{ij}W_{ij}}$ is the magnitude of the vorticity, d is the distance from the field point to the nearest wall, and

$$\begin{aligned} f_{v2} &= 1 - \frac{\chi}{1 + \chi f_{\nu 1}}, \qquad f_w = g\left[\frac{1 + c_{w3}^6}{g^6 + c_{w3}^6}\right]^{1/6}, \qquad g = r + c_{w2}\left(r^6 - r\right) \\ r &= \min\left[\frac{\hat{\nu}}{\hat{S}\kappa^2 d^2},\ 10\right], \quad f_{t2} = c_{t3}\exp\left(-c_{t4}\chi^2\right), \quad W_{ij} = \frac{1}{2}\left(\frac{\partial u_i}{\partial x_j} - \frac{\partial u_j}{\partial x_i}\right) \end{aligned} \tag{6}$$

According to Spalart and Allmaras [16], the following constraints should be enforced:

$$\sigma \in [0.6, 1.0] \tag{7}$$

$$c_{t1} \in [0.1, 10] \tag{8}$$

$$c_{t3} > 1.0 \tag{9}$$

$$c_{v1} > 6.9 \tag{10}$$

Spalart and Allmaras also note in Ref. 16 that c_{t2} is "not a candidate for much adjustment," and that c_{t4} can be decreased some, but that "values much smaller than 1 would start affecting the results in the turbulent region." Bailey et al. [23] determined that $\kappa = 0.40 \pm 0.02$ in their turbulent pipe flow experiments, and this range of κ was used for all of the turbulence models examined in this work. In private communication with the author [24], Spalart recommended using the bounds of Fig. 1 in Ref. 16 to determine the epistemic intervals of c_{b1}, c_{b2}, and c_{w2}. Spalart also recommended that

$$c_{w3} \in [1.75, 2.5] \tag{11}$$

In total, eleven closure coefficients were varied in the UQ analysis for SA. A summary of the SA closure coefficients to be varied, and their associated epistemic intervals are included in Table 3.1. Brief descriptions of each coefficient are included in Table 3.2.

Table 3.1: SA Closure Coefficients and Associated Epistemic Intervals.

Coefficient	Standard Value	Lower Bound	Upper Bound
σ	2/3	0.6	1.0
κ	0.41	0.38	0.42
c_{v1}	7.1	6.9	7.3
c_{w3}	2.0	1.75	2.5
c_{t1}	1.0	0.1	10.0
c_{t2}	2.0	1.9	2.1
c_{t3}	1.2	1.0	2.0
c_{t4}	0.5	0.3	0.7
c_{b1}	0.1355	0.12893	0.13700
c_{b2}	0.622	0.60983	0.68750
c_{w2}	0.3	0.05500	0.35250

Table 3.2: SA Closure Coefficient Descriptions.

Coefficient	Description
σ	Turbulent Prandtl number, part of diffusion term
κ	Von Kármán's constant Calibrates the log layer slope $\rightarrow \chi = \kappa y^+$
c_{v1}	Used in turbulent eddy viscosity calculation and production term Helps control the log law intercept
c_{w3}	Part of the f_w function (in destruction term), which speeds up the decay rate of the destruction term in the outer region of the BL
c_{t1}	Value empirically selected to control trip location
c_{t2}	Value empirically selected to control trip location
c_{t3}	Part of f_{t2} function (in production and destruction terms), which helps transition prediction by attracting $\hat{\nu} = 0$ as a solution
c_{t4}	Part of f_{t2} function (in production and destruction terms), which helps transition prediction by attracting $\hat{\nu} = 0$ as a solution
c_{b1}	Calibrates the growth of ν_t, which grows as $\exp(c_{b1} St)$
c_{b2}	Ensures that the integral of $\nu_t^{1+c_{b2}}$ can only increase, and smooths out velocity profile if $(1 + c_{b2})/\sigma > 2$
c_{w2}	Part of g function, which controls the slope of f_w in destruction Calibrated to match skin friction coefficient of flat plate

3.2. WILCOX (2006) k-ω TWO-EQUATION MODEL (W2006)

The k-ω model utilizes two equations to model a turbulent kinetic energy and length scale determining variable. The first equation is for turbulent kinetic energy, k, and the second equation is for the dissipation per unit turbulence kinetic energy, ω. In 2006, Wilcox introduced a new version of the k-ω model which greatly improved its accuracy for free shear flows and strongly separated flows by introducing a cross-

diffusion term and a built-in stress-limiter [25]. The W2006 model is given by

$$\frac{\partial(\rho k)}{\partial t} + \frac{\partial(\rho u_j k)}{\partial x_j} = P - \beta^* \rho \omega k + \frac{\partial}{\partial x_j}\left[\left(\mu + \sigma_k \frac{\rho k}{\omega}\right)\frac{\partial k}{\partial x_j}\right] \tag{12}$$

$$\frac{\partial(\rho \omega)}{\partial t} + \frac{\partial(\rho u_j \omega)}{\partial x_j} = \frac{\gamma \omega}{k} P - \beta \rho \omega^2 + \frac{\partial}{\partial x_j}\left[\left(\mu + \sigma_w \frac{\rho k}{\omega}\right)\frac{\partial \omega}{\partial x_j}\right] + \frac{\rho \sigma_d}{\omega}\frac{\partial k}{\partial x_j}\frac{\partial \omega}{\partial x_j} \tag{13}$$

The full formulation of the model is given by Wilcox [17]. The closure coefficients and their suggested values are given in Table 3.3. The closure coefficients also include

$$\gamma = \frac{\beta_0}{\beta^*} - \sigma_w \frac{\kappa^2}{\sqrt{\beta^*}} \tag{14}$$

Definitions of the terms in the model include:

$$P = \tau_{ij}\frac{\partial u_i}{\partial x_j} \tag{15}$$

$$\tau_{ij} = \mu_t\left(2S_{ij} - \frac{2}{3}\frac{\partial u_k}{\partial x_k}\delta_{ij}\right) - \frac{2}{3}\rho k \delta_{ij} \tag{16}$$

$$S_{ij} = \frac{1}{2}\left(\frac{\partial u_i}{\partial x_j} + \frac{\partial u_j}{\partial x_i}\right) \tag{17}$$

and the turbulent eddy viscosity is computed from:

$$\mu_t = \frac{\rho k}{\hat{\omega}} \tag{18}$$

where:

$$\hat{\omega} = \max\left[\omega,\ C_{lim}\sqrt{\frac{2\bar{S}_{ij}\bar{S}_{ij}}{\beta^*}}\right] \tag{19}$$

$$\bar{S}_{ij} = S_{ij} - \frac{1}{3}\frac{\partial u_k}{\partial x_k}\delta_{ij} \tag{20}$$

The auxiliary functions are

$$\chi_\omega = \left| \frac{\Omega_{ij}\Omega_{jk}\hat{S}_{ki}}{(\beta^*\omega)^3} \right|, \qquad f_\beta = \frac{1+85\chi_\omega}{1+100\chi_\omega}$$

$$\hat{S}_{ki} = S_{ki} - \frac{1}{2}\frac{\partial u_m}{\partial x_m}\delta_{ki}, \quad \Omega_{ij} = \frac{1}{2}\left(\frac{\partial u_i}{\partial x_j} - \frac{\partial u_j}{\partial x_i}\right) \tag{21}$$

$$\sigma_d = \begin{cases} 0, & \dfrac{\partial k}{\partial x_j}\dfrac{\partial \omega}{\partial x_j} \leq 0 \\ \sigma_{do}, & \dfrac{\partial k}{\partial x_j}\dfrac{\partial \omega}{\partial x_j} > 0 \end{cases}$$

In Ref. 25, Wilcox states that $\tau_{xy}/k \approx 3/10$, so $\beta^* = (\tau_{xy}/k)^2 \approx 9/100$. From this description, the author assumed that $\tau_{xy}/k \in [0.28, 0.32]$, yielding $\beta^* \in [0.0784, 0.1024]$. Wilcox also states that $\beta^*/\beta_0 = 1.25 \pm 0.06$ and that the following inequalities must hold true:

$$\sigma_{do} > \sigma_k - \sigma_w \tag{22}$$

$$\sigma_k > \sigma_{do} \tag{23}$$

In this study, the standard value of 1/8 was used for σ_{do} in all flow solutions. Acceptable ranges for σ_w and σ_k were established from inequalities (22) and (23) and from Figs. 4.16 and 4.17 in Ref. 25. In private communication with the author [26], Wilcox stated that the standard value of C_{lim} was chosen mainly for applications with Mach number greater than two. For the transonic range, Wilcox recommended a value of C_{lim} closer to one.

In total, six closure coefficients were varied in the UQ analysis for W2006. A summary of the W2006 closure coefficients to be varied and their epistemic intervals are included in Table 3.3. Brief descriptions of each coefficient are included in Table 3.4.

Table 3.3: W2006 Closure Coefficients and Associated Epistemic Intervals.

Coefficient	Standard Value	Lower Bound	Upper Bound
β^*	0.09	0.0784	0.1024
C_{lim}	0.875	0.75	1.0
κ	0.40	0.38	0.42
β^*/β_0	1.2712	1.19	1.31
σ_w	0.5	0.5	0.7
σ_k	0.6	0.5	0.6

Table 3.4: W2006 Closure Coefficient Descriptions.

Coefficient	Description
β^*	Relates (τ_{xy}/k), which equals ≈ 0.3 in the log layer Multiplies $k\omega$ in k-equation of the model
C_{lim}	Stress-limiter which improves model accuracy for shear flows and strongly separated flows
κ	Von Kármán's constant Involved in log layer calibration $\rightarrow \gamma = \beta_0/\beta^* - \sigma_w\kappa^2/\sqrt{\beta^*}$
β^*/β_0	β_0 used in the calculation of β for ω-equation; ratio approximates the time decay of homogeneous isotropic turbulence experiments
σ_w	Multiplies (k/ω) in ω-equation; value chosen to match empirical decay rate behavior of k and ν_T as wall distance increases
σ_k	Multiplies (k/ω) in k-equation; value chosen to match empirical decay rate behavior of k and ν_T as wall distance increases

3.3. MENTER SHEAR-STRESS TRANSPORT TWO-EQUATION MODEL (SST)

Menter's SST model uses blending functions to combine the k-ω and k-ϵ models [18]. The objective is to use the k-ω model in the near wall region where it is most accurate, and to take advantage of the freestream independence of the k-ϵ

model in the outer part of the boundary layer. The model is given by

$$\frac{\partial(\rho k)}{\partial t} + \frac{\partial(\rho u_j k)}{\partial x_j} = P - \beta^* \rho \omega k + \frac{\partial}{\partial x_j}\left[(\mu + \sigma_k \mu_t)\frac{\partial k}{\partial x_j}\right] \tag{24}$$

$$\begin{aligned}\frac{\partial(\rho \omega)}{\partial t} + \frac{\partial(\rho u_j \omega)}{\partial x_j} = \frac{\gamma}{\nu_t} P - \beta \rho \omega^2 + \frac{\partial}{\partial x_j}\left[(\mu + \sigma_w \mu_t)\frac{\partial \omega}{\partial x_j}\right] \\ + 2(1 - F_1)\frac{\rho \sigma_{w2}}{\omega}\frac{\partial k}{\partial x_j}\frac{\partial \omega}{\partial x_j}\end{aligned} \tag{25}$$

The full formulation of the model is given by Menter [18]. The closure coefficients and their suggested values are given in Table 3.5. The closure coefficients also include

$$\gamma_1 = \frac{\beta_1}{\beta^*} - \sigma_{w1}\frac{\kappa^2}{\sqrt{\beta^*}} \tag{26}$$

$$\gamma_2 = \frac{\beta_2}{\beta^*} - \sigma_{w2}\frac{\kappa^2}{\sqrt{\beta^*}} \tag{27}$$

As in the W2006 model, P, τ_{ij}, and S_{ij} are given by:

$$P = \tau_{ij}\frac{\partial u_i}{\partial x_j} \tag{28}$$

$$\tau_{ij} = \mu_t\left(2S_{ij} - \frac{2}{3}\frac{\partial u_k}{\partial x_k}\delta_{ij}\right) - \frac{2}{3}\rho k \delta_{ij} \tag{29}$$

$$S_{ij} = \frac{1}{2}\left(\frac{\partial u_i}{\partial x_j} + \frac{\partial u_j}{\partial x_i}\right) \tag{30}$$

but the turbulent eddy viscosity is computed from:

$$\mu_t = \frac{\rho a_1 k}{\max(a_1 \omega,\ \Omega F_2)} \tag{31}$$

Each of the constants is a blend of an inner (1) and outer (2) constant, blended via

$$\phi = F_1 \phi_1 + (1 - F_1)\phi_2 \tag{32}$$

where ϕ_1 represents constant 1 and ϕ_2 represents constant 2. Additional functions are given by

$$\begin{aligned}
F_1 &= \tanh(arg_1^4), \qquad arg_1 = \min\left[\max\left(\frac{\sqrt{k}}{\beta^*\omega d}, \frac{500\nu}{d^2\omega}\right), \frac{4\rho\sigma_{\omega 2}k}{CD_{k\omega}d^2}\right] \\
\nu_t &= \frac{\mu_t}{\rho}, \qquad\qquad CD_{k\omega} = \max\left(2\rho\sigma_{\omega 2}\frac{1}{\omega}\frac{\partial k}{\partial x_j}\frac{\partial \omega}{\partial x_j}, 10^{-20}\right) \\
F_2 &= \tanh(arg_2^2), \qquad arg_2 = \max\left(2\frac{\sqrt{k}}{\beta^*\omega d}, \frac{500\nu}{d^2\omega}\right) \\
\Omega &= \sqrt{2W_{ij}W_{ij}}, \qquad W_{ij} = \frac{1}{2}\left(\frac{\partial u_i}{\partial x_j} - \frac{\partial u_j}{\partial x_i}\right)
\end{aligned} \tag{33}$$

where ρ is the density, ν_t is the turbulent kinematic viscosity, μ is the dynamic viscosity, d is the distance from the field point to the nearest wall, and Ω is the vorticity magnitude.

Menter states that, "It has been the author's experience that small changes (5-10%) in modeling constraints can lead to a significant improvement (or deterioration) of model predictions" [18]. Unfortunately, little more information is available regarding plausible domains for SST closure coefficients. Many of the SST closure coefficients are shared with W2006, and in these cases the same epistemic intervals from W2006 were employed for SST. Georgiadis and Yoder [27] determined that $a_1 \in [0.31, 0.40]$. Menter agreed with this assessment in private communication with the author [28], stating that "One can only increase a_1 — decreasing it interferes with the log layer calibration."

In total, nine closure coefficients were varied in the UQ analysis for SST. A summary of the SST closure coefficients to be varied and their epistemic intervals is included in Table 3.5. Brief descriptions of each coefficient are included in Table 3.6.

Table 3.5: SST Closure Coefficients and Associated Epistemic Intervals.

Coefficient	Standard Value	Lower Bound	Upper Bound
σ_{k1}	0.85	0.7	1.0
σ_{k2}	1.0	0.8	1.2
σ_{w1}	0.5	0.3	0.7
σ_{w2}	0.856	0.7	1.0
β^*/β_1	1.20	1.19	1.31
β^*/β_2	1.0870	1.05	1.45
β^*	0.09	0.0784	0.1024
κ	0.41	0.38	0.42
a_1	0.31	0.31	0.40

Table 3.6: SST Closure Coefficient Descriptions.

Coefficient	Description
σ_{k1}, σ_{k2}	Blended and multiplied by (k/ω) in k-equation; values chosen to match empirical decay rate of k and ν_T as wall distance increases
σ_{w1}, σ_{w2}	Blended and multiplied by (k/ω) in ω-equation; values chosen to match empirical decay rate of k and ν_T as wall distance increases
β^*/β_1, β^*/β_2	Blend of β_1 and β_2 used in the calculation of β for ω-equation Blended ratio approximates the time decay of homogeneous isotropic turbulence experiments
β^*	Relates (τ_{xy}/k), which equals ≈ 0.3 in the log layer Multiplies $k\omega$ in k-equation of the model
κ	Von Kármán's constant Involved in log layer calibration (γ_1 and γ_2 calculations)
a_1	Used in turbulent eddy viscosity definition

4. UNCERTAINTY QUANTIFICATION APPROACH

Uncertainties in computational models fall into two categories: aleatory and epistemic. Aleatory uncertainties represent inherent variations in a system, whereas epistemic uncertainties arise due to lack of knowledge. (For example, the outcome of a coin flip is aleatory because it is due to inherent chance; however if a coin is placed on a table and covered up, the uncertainty in heads/tails is epistemic because it is due to a lack of knowledge.) In this work, all closure coefficients are treated as epistemic uncertain variables due to the lack of a complete physical understanding of turbulence. Section 4.1 of this chapter describes the point-collocation non-intrusive polynomial chaos method employed to characterize this uncertainty. Sobol indices are used as a sensitivity measure, and in Section 4.2 a description and derivation of Sobol indices is presented.

4.1. POINT-COLLOCATION NON-INTRUSIVE POLYNOMIAL CHAOS

Rather than resorting to Monte Carlo simulations for uncertainty quantification, stochastic expansions based on point-collocation non-intrusive polynomial chaos (NIPC) were employed to reduce computational expense [2]. The strategy of point-collocation NIPC is to create a surrogate model via least squares approach (i.e., polynomial response surface) by using the CFD output obtained at a number of Latin Hypercube sample points for the propagation of uncertainty. An explanation of point-collocation NIPC given by West et al. [7] follows. With the polynomial chaos approach, a stochastic response function α^* (e.g., drag coefficient, pressure or skin friction coefficient at a given point in the flow field) can be decomposed into separable

deterministic and stochastic components within a series expansion:

$$\alpha^*(\boldsymbol{x}, \boldsymbol{\xi}) \approx \sum_{i=0}^{P} \alpha_i(\boldsymbol{x}) \Psi_i(\boldsymbol{\xi}) \tag{34}$$

where α_i is the deterministic component and Ψ_i is the random variable basis functions corresponding to the i^{th} mode. α^* is assumed to be a function of a deterministic vector $\boldsymbol{x}$, which includes the spatial coordinates and deterministic parameters of the problem, and of the n-dimensional standard random variable vector $\boldsymbol{\xi}$. In theory, the series in Eq. (34) is infinite, but for practical implementation of the polynomial chaos expansions it is truncated and a discrete sum is taken over a number of output modes, $(P + 1)$. Further details on polynomial chaos theory are given by Ghanem [11] and Eldred [12].

There are three parameters that determine the number of samples required to generate the response surface: the number of uncertain variables, n; the order of the response surface polynomial, p; and the oversampling ratio, n_p. The total number of samples, N_s, is then given by

$$N_s = n_p \cdot (P + 1) = n_p \left[\frac{(n + p)!}{n!p!} \right] \tag{35}$$

The Point-Collocation NIPC method starts with replacing a stochastic response or random function with its polynomial chaos expansion in Eq. (34). Then, N_s vectors are chosen in random space and the deterministic code (the CFD flow solver in this case) is evaluated at these points; this is the left-hand side of Eq. (34). Finally a linear system of N_s equations is formulated and solved for the spectral modes of the

random variables. This system is given by:

$$\begin{pmatrix} \alpha^*(\boldsymbol{x}, \boldsymbol{\xi}_0) \\ \alpha^*(\boldsymbol{x}, \boldsymbol{\xi}_1) \\ \vdots \\ \alpha^*(\boldsymbol{x}, \boldsymbol{\xi}_{(N_s-1)}) \end{pmatrix} = \begin{pmatrix} \Psi_0(\boldsymbol{\xi}_0) & \Psi_1(\boldsymbol{\xi}_0) & \dots & \Psi_P(\boldsymbol{\xi}_0) \\ \Psi_0(\boldsymbol{\xi}_1) & \Psi_1(\boldsymbol{\xi}_1) & \dots & \Psi_P(\boldsymbol{\xi}_1) \\ \vdots & \vdots & \ddots & \vdots \\ \Psi_0(\boldsymbol{\xi}_{(N_s-1)}) & \Psi_1(\boldsymbol{\xi}_{(N_s-1)}) & \dots & \Psi_P(\boldsymbol{\xi}_{(N_s-1)}) \end{pmatrix} \begin{pmatrix} \alpha_0 \\ \alpha_1 \\ \vdots \\ \alpha_P \end{pmatrix} \tag{36}$$

An oversampling ratio of 1.0 yields the minimum number of samples required to produce a response surface. Hosder et al. [29] demonstrated that an oversampling ratio of $n_p = 2.0$ gives a better approximation to the statistics at each polynomial degree they considered. For this reason, $n_p = 2.0$ was used for all of the UQ analyses in this work. Given $n_p > 1.0$, Eq. (36) is overdetermined and can be solved using a least squares approach. In the current work, a polynomial order of two ($p = 2$) was used for all UQ analyses.

Due to the bounded nature of epistemic input uncertainties, Legendre polynomials are used in this study as the basis functions. Although stochastic response surfaces created with the NIPC approach allow the calculation of confidence intervals along with various statistics of the output for probabilistic (aleatory) input, in this study only the maximum and the minimum of the response will be calculated from the response surface to determine the epistemic interval for each uncertain output.

4.2. SOBOL INDICES

Sobol indices (global nonlinear sensitivity indices) were used to rank the relative contributions of each closure coefficient to the total uncertainty in the output quantities of interest. Sobol indices can be derived via Sobol Decomposition, which

is a variance-based global sensitivity analysis method. This derivation utilizes the polynomial chaos expansion coefficients calculated in Eq. (36). First, the total variance, D, can be written in terms of the PCE as shown in Eq. (37).

$$D = \sum_{j=1}^{P} \alpha_j^2(t, \vec{x}) \left\langle \Psi_j^2(\vec{\xi}) \right\rangle \tag{37}$$

Then, as shown by Sudret [3] and Crestaux et al. [30], the total variance can be decomposed as:

$$D = \sum_{i=1}^{i=n} D_i + \sum_{1 \le i < j \le n}^{i=n-1} D_{i,j} + \sum_{1 \le i < j < k \le n}^{i=n-2} D_{i,j,k} + \cdots + D_{1,2,\ldots,n} \tag{38}$$

where the partial variances ($D_{i_1,\ldots,i_s}$) are given by:

$$D_{i_1,\ldots,i_s} = \sum_{\beta \in \{i_1,\ldots,i_s\}} \alpha_\beta^2 \left\langle \Psi_\beta^2(\vec{\xi}) \right\rangle, \qquad 1 \le i_1 < \ldots < i_s \le n \tag{39}$$

Then the Sobol indices ($S_{i_1 \cdots i_s}$) are defined as,

$$S_{i_1 \cdots i_s} = \frac{D_{i_1,\ldots,i_s}}{D} \tag{40}$$

which satisfy the following equation:

$$\sum_{i=1}^{i=n} S_i + \sum_{1 \le i < j \le n}^{i=n-1} S_{i,j} + \sum_{1 \le i < j < k \le n}^{i=n-2} S_{i,j,k} + \cdots + S_{1,2,\ldots,n} = 1.0 \tag{41}$$

The Sobol indices provide a sensitivity measure due to individual contribution from each input uncertain variable (S_i), as well as the mixed contributions ($\{S_{i,j}\}, \{S_{i,j,k}\}, \cdots$). As shown by Sudret [3] and Ghaffari et al. [31], the total (combined) effect (S_{T_i}) of an input parameter i is defined as the summation of the partial Sobol indices that include the particular parameter:

$$S_{T_i} = \sum_{L_i} \frac{D_{i_1,\ldots,i_s}}{D}; \quad L_i = \{(i_1, \ldots, i_s) : \exists\, k,\ 1 \leq k \leq s,\ i_k = i\} \tag{42}$$

For example, with $n = 3$, the total contribution to the overall variance from the first uncertain variable ($i = 1$) can be written as:

$$S_{T_1} = S_1 + S_{1,2} + S_{1,3} + S_{1,2,3} \tag{43}$$

From these formulations, it can be seen that the Sobol indices can be used to provide a relative ranking of each input uncertainty to the overall variation in the output with the consideration of nonlinear correlation between input variables and output quantities of interest.

5. RESULTS OF MAIN STUDY

The results of the main study uncertainty quantification analyses are presented in this chapter. The axisymmetric, transonic bump is discussed in Sections 5.1 and 5.2; and the RAE 2822 transonic airfoil is discussed in Sections 5.3 and 5.4. A comparison of the results from both CFD problems is discussed in Section 5.5.

5.1. AXISYMMETRIC TRANSONIC BUMP - ORIGINAL ANALYSES

The purpose of the original uncertainty quantification analyses was to identify the closure coefficients that contribute significantly to uncertainty in the output quantities of interest. These coefficients were later used in reduced-dimensionality analyses. For the transonic bump, the output quantities of interest include drag coefficient (C_D); pressure and skin friction coefficient distributions (C_p and C_f); and separation bubble size.

Sobol indices were used to rank the relative contributions of each closure coefficient to the overall uncertainty in C_D. Coefficients with higher Sobol indices contribute more to the uncertainty than coefficients with lower Sobol indices. The Sobol indices of the closure coefficients for each turbulence model for C_D are presented in Table 5.1, where they are ranked from highest to lowest. The largest contributors to uncertainty in each model are typed in blue. Coefficients with Sobol indices of less than 3.0×10^{-2} were not considered to be significant. The closure coefficients retained for each turbulence model with this approach account for at least 95% of the total uncertainty in the output quantity of interest (Table 5.1).

The largest contributors to uncertainty in C_D for the SA model are κ, σ, and c_{v1}. The largest contributors for W2006 are σ_w, C_{lim}, and β^*. The largest contributors for SST are β^*, σ_{w1}, β^*/β_1, and β^*/β_2. Note that β^* is shared by both the W2006

and SST models. Also note that σ_{w1} in the SST model is the equivalent of σ_w in the W2006 model. Von Kármán's constant (κ) is included in all three models, but it is only significant to uncertainty in C_D for the SA model.

Response surfaces for pressure coefficient (C_p) and skin friction coefficient (C_f) were generated at each axial location across the bump. Sobol indices for these coefficients were also calculated at each axial location. Plots of the Sobol indices for C_p and C_f versus x were generated so that the closure coefficients significant to these quantities at points in the flow could be identified. These plots are included in Fig. 5.1. For clarity, only the Sobol indices of coefficients with significant contributions to uncertainty in C_p are shown in the plots.

The largest contributors to uncertainty in C_p and C_f for the SA model are σ, κ, c_{v1}, c_{w3}, c_{b1}, and c_{w2}. The largest contributors for the W2006 model are β^*, C_{lim}, and σ_w. The largest contributors for the SST model are σ_{w1}, β^*/β_1, β^*/β_2, β^*, and a_1.

Table 5.1: Sobol Indices of Closure Coefficients for C_D.

SA		W2006		SST	
Coefficient	Sobol Index	Coefficient	Sobol Index	Coefficient	Sobol Index
κ	8.50×10^{-1}	σ_w	7.75×10^{-1}	β^*	8.03×10^{-1}
σ	5.99×10^{-2}	C_{lim}	1.42×10^{-1}	σ_{w1}	9.24×10^{-2}
c_{v1}	5.38×10^{-2}	β^*	1.26×10^{-1}	β^*/β_1	7.79×10^{-2}
c_{w2}	2.59×10^{-2}	σ_k	2.12×10^{-2}	β^*/β_2	3.54×10^{-2}
c_{b1}	1.11×10^{-2}	κ	1.99×10^{-2}	σ_{w2}	1.85×10^{-3}
c_{b2}	4.66×10^{-4}	β^*/β_0	7.46×10^{-3}	σ_{k2}	1.21×10^{-3}
c_{w3}	5.33×10^{-5}			a_1	8.25×10^{-4}
c_{t3}	9.71×10^{-6}			σ_{k1}	4.91×10^{-4}
c_{t1}	8.91×10^{-6}			κ	1.24×10^{-4}
c_{t4}	8.57×10^{-6}				
c_{t2}	5.13×10^{-6}				

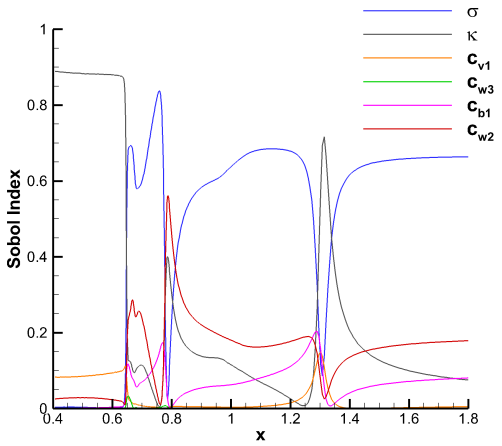

(a) Sobol indices for C_p versus x (SA).

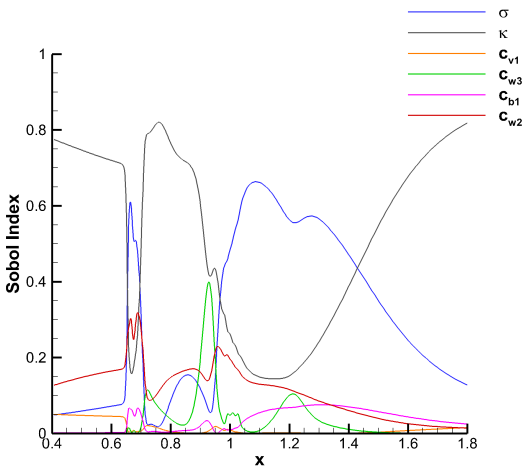

(b) Sobol indices for C_f versus x (SA).

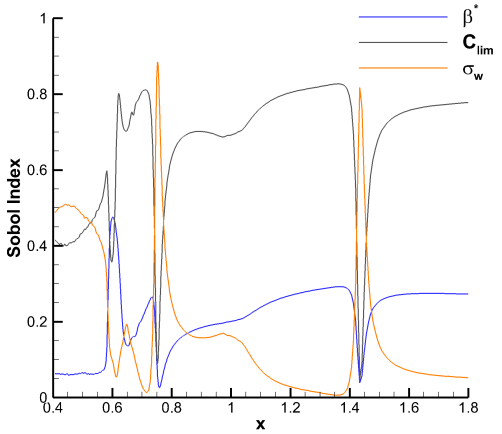

(c) Sobol indices for C_p versus x (W2006).

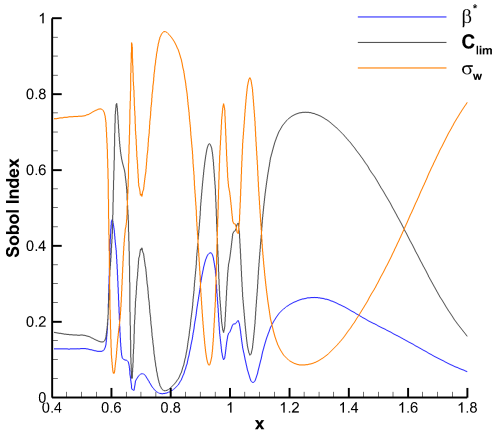

(d) Sobol indices for C_f versus x (W2006).

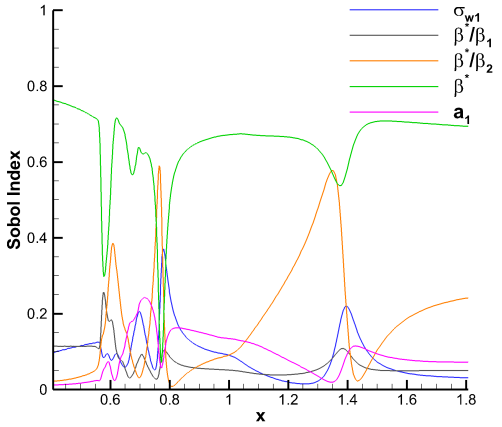

(e) Sobol indices for C_p versus x (SST).

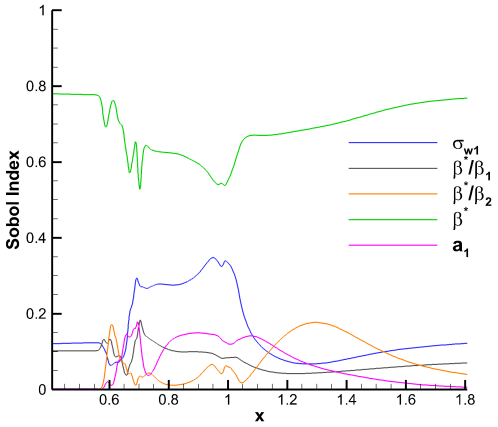

(f) Sobol indices for C_f versus x (SST).

Figure 5.1: Sobol index distributions for transonic bump (Original Analyses).

Table 5.2: Sobol Indices of Closure Coefficients for Separation Bubble Size.

SA		W2006		SST	
Coefficient	Sobol Index	Coefficient	Sobol Index	Coefficient	Sobol Index
σ	5.58×10^{-1}	C_{lim}	7.26×10^{-1}	β^*	6.49×10^{-1}
κ	1.82×10^{-1}	β^*	2.57×10^{-1}	σ_{w1}	1.15×10^{-1}
c_{w2}	1.54×10^{-1}	σ_w	1.03×10^{-1}	a_1	1.06×10^{-1}
c_{b1}	6.74×10^{-2}	σ_k	1.46×10^{-2}	β^*/β_2	9.48×10^{-2}
c_{w3}	3.71×10^{-2}	κ	9.92×10^{-3}	β^*/β_1	9.24×10^{-2}
c_{v1}	1.87×10^{-3}	β^*/β_0	5.51×10^{-3}	σ_{k2}	2.09×10^{-2}
c_{t3}	6.76×10^{-4}			κ	1.70×10^{-2}
c_{t4}	6.05×10^{-4}			σ_{w2}	1.36×10^{-2}
c_{t2}	5.98×10^{-4}			σ_{k1}	9.77×10^{-3}
c_{b2}	5.68×10^{-4}				
c_{t1}	5.56×10^{-4}				

The separation bubble size for each case of each model was taken as the difference between the x-coordinate of the zero-intersection points in the C_f versus x curves. Using the same process as before, stochastic response surfaces were created for the separation bubble size for each model. The Sobol indices of the closure coefficients for separation bubble size are given in Table 5.2.

The largest contributors to uncertainty in separation bubble size for the SA model are σ, κ, c_{w2}, c_{b1}, and c_{w3}. The largest contributors for the W2006 model are C_{lim}, β^*, and σ_w. The largest contributors for the SST model are β^*, σ_{w1}, a_1, β^*/β_2, and β^*/β_1.

In sum, six closure coefficients were found to contribute significantly to at least one output quantity of interest for the SA model; three closure coefficients for the W2006 model; and five coefficients for the SST model. This information is summarized in Table 5.3.

Table 5.3: Closure Coefficients with Significant Contributions to Transonic Bump.

SA	W2006	SST
σ	β^*	σ_{w1}
κ	C_{lim}	β^*/β_1
c_{v1}	σ_w	β^*/β_2
c_{w2}		β^*
c_{b1}		a_1
c_{w3}		

5.2. AXISYMMETRIC TRANSONIC BUMP - REDUCED DIMENSIONALITY ANALYSES

To further increase the accuracy of the uncertainty analysis by creating the stochastic response surface with a smaller number of uncertain variables, a reduced dimensionality analysis (RDA) was performed for the axisymmetric transonic bump with each turbulence model by using only the significant closure coefficients found in Table 5.3.

A baseline case was run with the standard set of closure coefficients for each turbulence model. Stochastic polynomial response surfaces of C_D were obtained with NIPC on the uncertain domain. The minimum and maximum values of drag coefficient (C_D) for each model were calculated from these response surfaces. To verify the accuracy of each response surface, additional CFD solutions were generated by using the sets of closure coefficients that produced the minimum and maximum values of C_D on the response surface; the C_D comparison between the response surfaces and the CFD is summarized in Table 5.4. In each case, the response surface is within 4.07% or less of the CFD. The difference values reported in Table 5.4 indicate an acceptable level of accuracy for epistemic uncertainty analyses.

In the experiment, Bachalo and Johnson estimated the separation and reattachment points to be $x = 0.70$ and $x = 1.1$ respectively. This yields a separation bubble size of $0.40(x/c)$ (based on the bump length of $c = 1$). The separation

Table 5.4: Drag Coefficient Results, in Drag Counts (RDA).

	Baseline C_D	Min C_D			Max C_D		
Model	CFD	Resp. Surf.	CFD	Difference	Resp. Surf.	CFD	Difference
SA	2.232	2.148	2.130	0.85%	2.270	2.288	0.79%
W2006	2.226	2.116	2.098	0.86%	2.243	2.224	0.85%
SST	2.284	1.813	1.890	4.07%	2.647	2.612	1.34%

Table 5.5: Separation Bubble Size Results (RDA).

Model	Baseline Size CFD	Min Size Resp. Surf.	Max Size Resp. Surf.
SA	0.467	0.441	0.507
W2006	0.535	0.522	0.672
SST	0.507	0.000	0.903

bubble size results for the UQ analyses are included in Table 5.5. Originally, the SST response surface for separation bubble size yielded a negative minimum bubble size. This was due to the fact that for certain samples there was a very small, or even no separation region, yielding negative values for the response. Since this is not physical, the minimum value is set to zero.

The Sobol indices for C_D and separation bubble size agree well with the Sobol indices in the original analyses. These values are included in Tables 5.6 and 5.7. The ranking of importance is mostly the same between the original and reduced-dimensionality analyses. Even when the ranking of importance is not the same, the actual numeric values of the Sobol indices in the reduced-dimensionality analyses are still reasonably close to their corresponding values in the original analyses.

Table 5.6: Sobol Indices of Closure Coefficients for C_D (RDA).

SA		W2006		SST	
Coefficient	Sobol Index	Coefficient	Sobol Index	Coefficient	Sobol Index
κ	8.51×10^{-1}	σ_w	7.26×10^{-1}	β^*	7.95×10^{-1}
σ	6.08×10^{-2}	β^*	2.07×10^{-1}	σ_{w1}	9.19×10^{-2}
c_{v1}	5.35×10^{-2}	C_{lim}	1.89×10^{-1}	β^*/β_1	7.96×10^{-2}
c_{w2}	2.56×10^{-2}			β^*/β_2	4.86×10^{-2}
c_{b1}	1.08×10^{-2}			a_1	3.01×10^{-3}
c_{w3}	3.17×10^{-5}				

Table 5.7: Sobol Indices of Closure Coefficients for Separation Bubble Size (RDA).

SA		W2006		SST	
Coefficient	Sobol Index	Coefficient	Sobol Index	Coefficient	Sobol Index
σ	5.79×10^{-1}	C_{lim}	7.49×10^{-1}	β^*	6.27×10^{-1}
κ	1.84×10^{-1}	β^*	2.71×10^{-1}	β^*/β_1	1.86×10^{-1}
c_{w2}	1.45×10^{-1}	σ_w	7.63×10^{-2}	σ_{w1}	1.37×10^{-1}
c_{b1}	5.91×10^{-2}			β^*/β_2	1.24×10^{-1}
c_{w3}	3.27×10^{-2}			a_1	7.99×10^{-2}
c_{v1}	3.65×10^{-3}				

Response surfaces for pressure coefficient (C_p) and skin friction coefficient (C_f) were generated at each axial location across the bump. Sobol indices for these coefficients were also calculated at each axial location. The minimum and maximum possible values of C_p and C_f were calculated at each axial location from the response surfaces.

Plots of C_p versus x were generated for all of the cases used in the UQ analysis, for each turbulence model. This was done to verify the physical feasibility of the solutions. Each plot contains data for the baseline case; UQ training cases (green lines); minimum and maximum C_p bounds; and experimental data from Bachalo and Johnson [20]. It should be emphasized that Bachalo and Johnson did not report any

experimental uncertainty in their results, so the experimental data in these figures should be considered as reference only. A proper comparison with experiment should take into account the uncertainty both in the numerical model and experimental data, and the difference should be quantified with appropriate metrics for the validation of the numerical model.

The C_p versus x plots are included in Figs. 5.2a, 5.2c, and 5.2e. The Sobol indices for C_p versus x are included in Figs. 5.2b, 5.2d, and 5.2f. For clarity, only the Sobol indices of coefficients with significant contributions to uncertainty in C_p are shown in the figures. For each model, additional cases were run at the corners of the hypercube defined by the epistemic interval bounds of only the most significant closure coefficients; this was done to eliminate the effect of discontinuities in the response surfaces near the shock and to determine the epistemic uncertainty interval for the output in the shock region only. The C_p minimum and maximum curves in Figs. 5.2a, 5.2c, and 5.2e are piece-wise combinations of the NIPC response surfaces and these hypercube cases in the shock region.

Note that each of the minimum and maximum C_p curves may not in general correspond to one flow solution each, because each point along each curve is calculated from either the response surface generated by using the C_p values of each UQ case at that specific x-location, or by one of the hypercube corner cases. While there exist flow solutions that pass through or very near to the minimum and maximum C_p curves at each point, there is no flow solution that passes through all of the minimum or all of the maximum points.

Plots of skin friction coefficient at each axial location were created in a similar fashion as the plots of pressure coefficient. Plots of C_f versus x for each UQ case are included in Figs. 5.3a, 5.3c, and 5.3e. As before, the minimum and maximum C_f curves in these figures are piece-wise combinations of the NIPC response surfaces at each axial location and hypercube corner samples in the shock region. The vertical

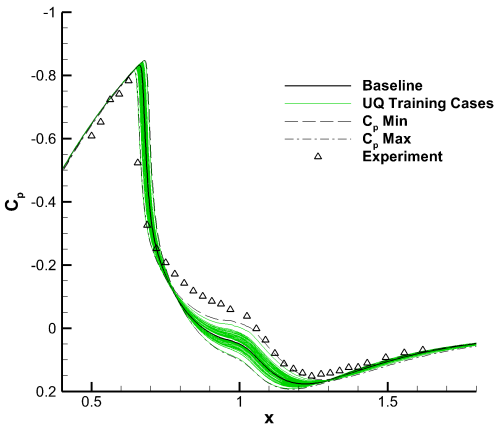

(a) C_p versus x (SA).

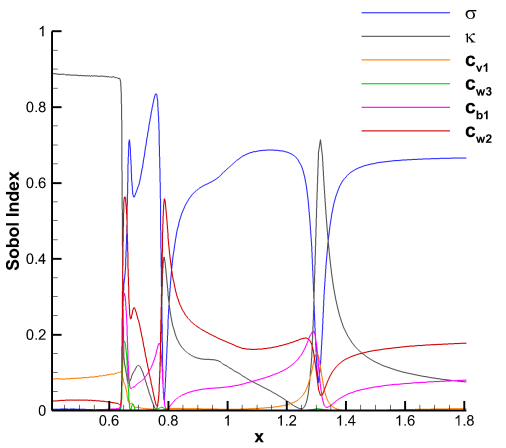

(b) Sobol indices for C_p versus x (SA).

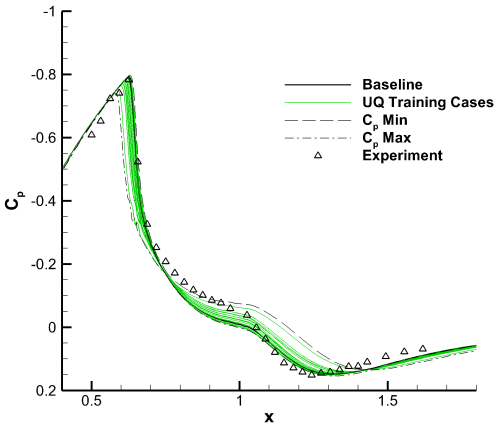

(c) C_p versus x (W2006).

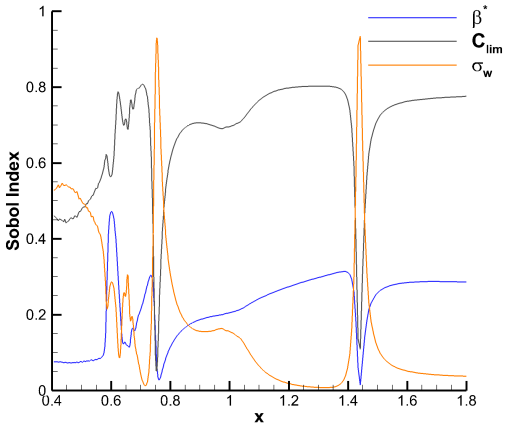

(d) Sobol indices for C_p versus x (W2006).

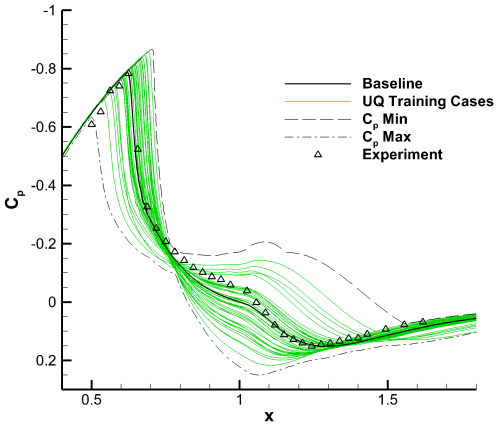

(e) C_p versus x (SST).

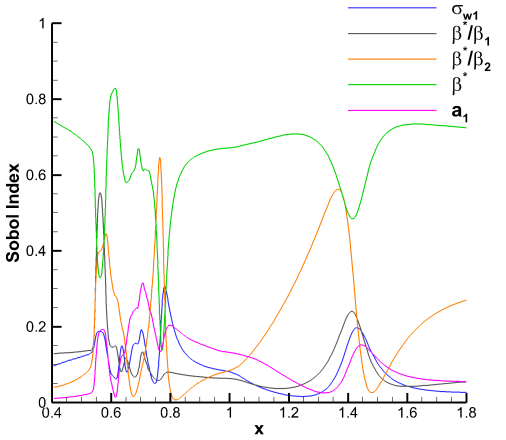

(f) Sobol indices for C_p versus x (SST).

Figure 5.2: Pressure coefficient results for transonic bump.

lines in the plots are the separation and reattachment point locations reported by Bachalo and Johnson [20]. The Sobol indices for C_f at each axial location are shown in Figs. 5.3b, 5.3d, and 5.3f.

Based on the reduced-dimensionality results, all of the coefficients found to be significant to the axisymmetric transonic bump in Section 5.1 are indeed significant to their respective turbulence models, even in the absence of possible numerical "noise" caused by the insignificant coefficients in the original analyses. Of the three turbulence models, the SST model is most sensitive to changes in its closure coefficients; this is evidenced by large variations in the model's values for C_D and separation bubble size, as well as the large solution bands for C_p and C_f. The SA and W2006 models are roughly equally sensitive to changes in their closure coefficients. All of the models are most sensitive to changes in their closure coefficients in the shock and separated regions of the flow, particularly so in the latter region. None of the models exhibit large uncertainties in C_p upstream of the shock or downstream of the reattachment point, however the uncertainty in C_f remains large in these regions.

5.3. RAE 2822 AIRFOIL - ORIGINAL ANALYSES

As with the original analyses of the transonic bump, the purpose of the original analyses of the RAE 2822 airfoil was to identify the closure coefficients that contribute significantly to uncertainty in the output quantities of interest. For the RAE 2822, the output quantities of interest include the lift coefficient (C_L), drag coefficient due to pressure ($C_{D_{\text{press}}}$), drag coefficient due to skin friction ($C_{D_{\text{sf}}}$), and pressure coefficient distribution (C_p). The skin friction coefficient distribution was not investigated for the RAE 2822 because no separation bubble was observed in the baseline case solutions.

In the same manner as for the transonic bump, Sobol indices were calculated for the output quantities of interest of the RAE 2822. The results for C_L, $C_{D_{\text{press}}}$, and $C_{D_{\text{sf}}}$ are included in Tables 5.8, 5.9, and 5.10 respectively.

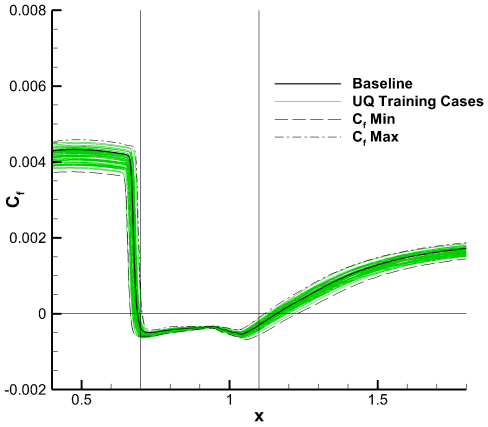

(a) C_f versus x (SA).

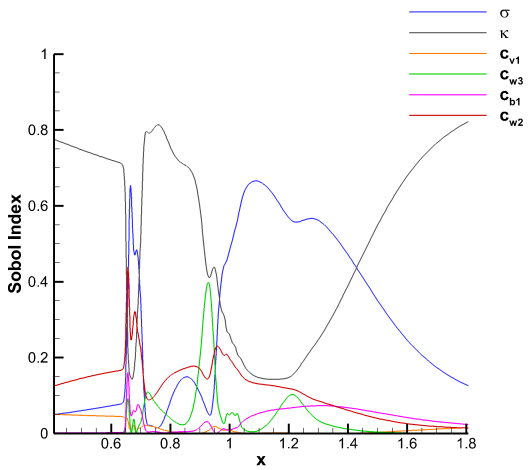

(b) Sobol indices for C_f versus x (SA).

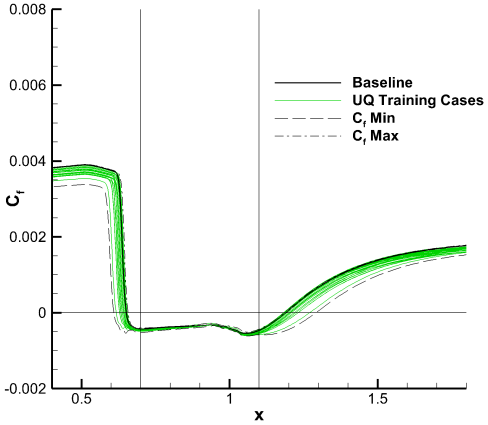

(c) C_f versus x (W2006).

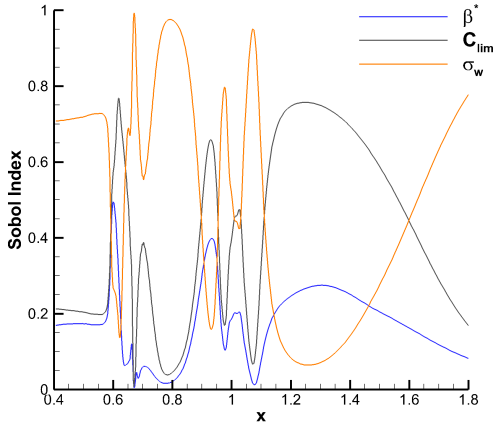

(d) Sobol indices for C_f versus x (W2006).

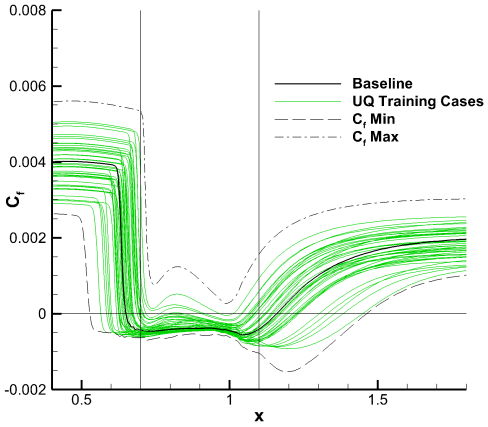

(e) C_f versus x (SST).

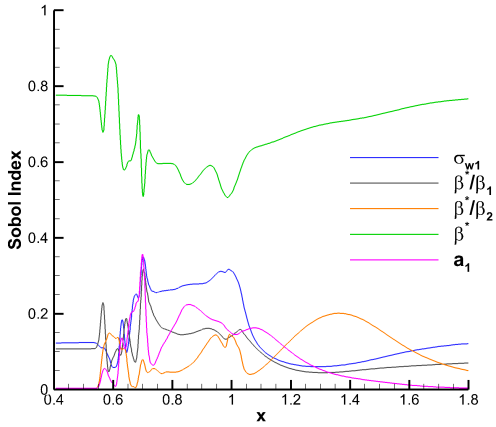

(f) Sobol indices for C_f versus x (SST).

Figure 5.3: Skin friction coefficient results for transonic bump.

Table 5.8: Sobol Indices of Closure Coefficients for C_L of RAE 2822.

SA		W2006		SST	
Coefficient	Sobol Index	Coefficient	Sobol Index	Coefficient	Sobol Index
κ	5.07×10^{-1}	C_{lim}	8.55×10^{-1}	β^*/β_2	4.22×10^{-1}
c_{t4}	2.34×10^{-1}	β^*	9.57×10^{-2}	a_1	4.13×10^{-1}
c_{t3}	1.82×10^{-1}	σ_w	4.23×10^{-2}	β^*	2.50×10^{-1}
c_{v1}	7.30×10^{-2}	κ	1.83×10^{-2}	σ_{w2}	2.37×10^{-2}
c_{b1}	3.18×10^{-2}	β^*/β_0	1.27×10^{-2}	σ_{w1}	1.64×10^{-2}
c_{w2}	1.78×10^{-2}	σ_k	1.19×10^{-2}	β^*/β_1	1.59×10^{-2}
σ	1.55×10^{-2}			σ_{k2}	1.11×10^{-2}
c_{b2}	1.51×10^{-2}			σ_{k1}	9.95×10^{-3}
c_{w3}	9.52×10^{-3}			κ	8.63×10^{-3}
c_{t1}	8.12×10^{-3}				
c_{t2}	6.13×10^{-3}				

Table 5.9: Sobol Indices of Closure Coefficients for $C_{D_{\text{press}}}$.

SA		W2006		SST	
Coefficient	Sobol Index	Coefficient	Sobol Index	Coefficient	Sobol Index
σ	4.64×10^{-1}	C_{lim}	6.62×10^{-1}	β^*	6.30×10^{-1}
c_{w2}	2.13×10^{-1}	σ_w	2.14×10^{-1}	β^*/β_2	2.36×10^{-1}
c_{b1}	1.91×10^{-1}	β^*	1.71×10^{-1}	a_1	1.34×10^{-1}
c_{t4}	7.10×10^{-2}	β^*/β_0	4.81×10^{-3}	β^*/β_1	3.22×10^{-2}
c_{v1}	2.90×10^{-2}	κ	2.46×10^{-3}	σ_{w1}	1.18×10^{-2}
κ	2.74×10^{-2}	σ_k	2.32×10^{-3}	σ_{w2}	1.11×10^{-2}
c_{t3}	2.07×10^{-2}			σ_{k2}	4.99×10^{-3}
c_{b2}	1.25×10^{-2}			σ_{k1}	4.71×10^{-3}
c_{t2}	7.16×10^{-3}			κ	1.95×10^{-3}
c_{t1}	5.01×10^{-3}				
c_{w3}	3.90×10^{-3}				

For the SA model, the largest contributors to uncertainty in C_L are κ, c_{t4}, c_{t3}, c_{v1}, and c_{b1}. The largest contributors to uncertainty in $C_{D_{\text{press}}}$ are σ, c_{w2}, c_{b1}, and c_{t4}; and the largest contributors to uncertainty in $C_{D_{\text{sf}}}$ are κ, σ, c_{w2}, c_{t4}, c_{t3}, and c_{v1}.

Table 5.10: Sobol Indices of Closure Coefficients for $C_{D_{\text{sf}}}$.

SA		W2006		SST	
Coefficient	Sobol Index	Coefficient	Sobol Index	Coefficient	Sobol Index
κ	5.65×10^{-1}	σ_w	6.41×10^{-1}	β^*	7.75×10^{-1}
σ	2.36×10^{-1}	C_{lim}	2.39×10^{-1}	σ_{w1}	1.22×10^{-1}
c_{w2}	8.50×10^{-2}	β^*	1.56×10^{-1}	β^*/β_1	9.50×10^{-2}
c_{t4}	4.30×10^{-2}	κ	1.07×10^{-2}	a_1	9.84×10^{-3}
c_{t3}	3.58×10^{-2}	σ_k	9.71×10^{-3}	β^*/β_2	5.32×10^{-3}
c_{v1}	3.06×10^{-2}	β^*/β_0	3.59×10^{-3}	σ_{w2}	1.17×10^{-3}
c_{b1}	1.97×10^{-2}			σ_{k1}	8.58×10^{-4}
c_{b2}	1.65×10^{-3}			σ_{k2}	8.34×10^{-4}
c_{t1}	1.36×10^{-3}			κ	1.30×10^{-4}
c_{w3}	1.17×10^{-3}				
c_{t2}	6.17×10^{-4}				

For the W2006 model, the largest contributors to uncertainty in all three integrated quantities are C_{lim}, β^*, and σ_w. The order of importance is different for C_L, $C_{D_{\text{press}}}$, and $C_{D_{\text{sf}}}$, but the important coefficients are the same for each quantity.

For the SST model, the largest contributors to uncertainty in C_L are β^*/β_2, a_1, and β^*. The largest contributors to uncertainty in $C_{D_{\text{press}}}$ are β^*, β^*/β_2, a_1, and β^*/β_1; and the largest contributors to uncertainty in $C_{D_{\text{sf}}}$ are β^*, σ_{w1}, and β^*/β_1.

Response surfaces for C_p were generated at each x-location on the top and bottom surface of the airfoil so that the closure coefficients with significant contributions to C_p at any given point in the flow could be identified. These plots are included in Fig. 5.4. In Fig. 5.4a, the largest contributor to uncertainty in C_p for the majority of the x domain in the SA model is κ. There are also spikes in the Sobol indices of c_{t3}, c_{t4}, and σ, indicating that these coefficients are also important in some parts of the flow; particularly, spikes appear near the shock on the upper surface and near the high-pressure region at the leading edge on the lower surface. In Fig. 5.4b, the uncertainty in C_p for the W2006 model is almost completely dominated by C_{lim},

Table 5.11: Closure Coefficients with Significant Contributions to RAE 2822.

SA	W2006	SST
σ	β^*	σ_{w1}
κ	C_{lim}	β^*/β_1
c_{v1}	σ_w	β^*/β_2
c_{t3}		β^*
c_{t4}		a_1
c_{b1}		
c_{w2}		

with only a few minor contributions from β^* and σ_2. In Fig. 5.4c, the uncertainty in C_p for the SST model is mostly attributed to β^*/β_2, β^*, and a_1. At $x \approx 0.6$, σ_{w1} also has a minor contribution.

In sum, seven closure coefficients were found to contribute significantly to at least one output quantity of interest for the SA model; three coefficients for the W2006 model; and five coefficients for the SST model. This information is summarized in Table 5.11.

5.4. RAE 2822 AIRFOIL - REDUCED DIMENSIONALITY ANALYSES

As with the transonic bump, a reduced-dimensionality analysis was performed on the RAE 2822 for each of the turbulence models to further improve the accuracy of the response surfaces used in the uncertainty analyses. A baseline case was run with each of the original, unchanged turbulence models for the RAE 2822 airfoil. The response surfaces of drag coefficient and lift coefficient for the RAE 2822 were verified in the same manner as the response surfaces of the drag coefficient of the transonic bump; the minimum and maximum values of C_D and C_L were first calculated from the response surfaces, and then CFD simulations were run by using the closure coefficients that produced these minimum and maximum values. The comparison between the

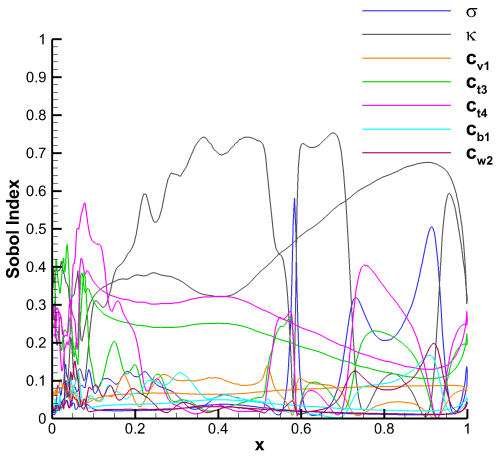

(a) Sobol indices for C_p versus x (SA).

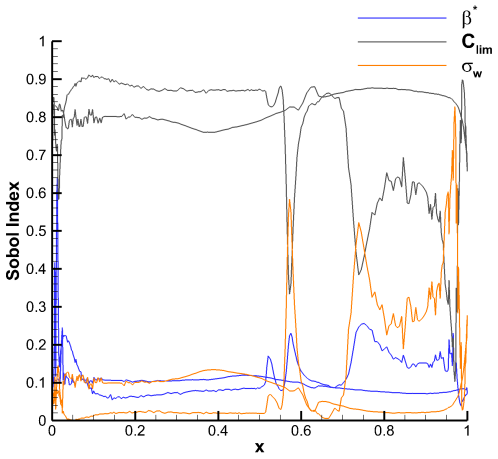

(b) Sobol indices for C_p versus x (W2006).

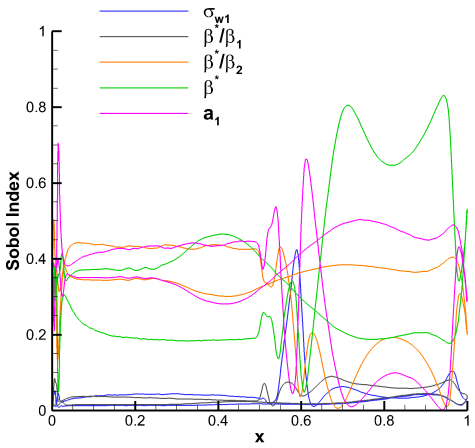

(c) Sobol indices for C_p versus x (SST).

Figure 5.4: Sobol index distributions for RAE 2822 airfoil (Original Analyses).

response surfaces and CFD is summarized in Tables 5.12 and 5.13. All of the C_D response surfaces are within 4.37% or less of the CFD, and the C_L response surfaces are within 1.18% or less of the CFD.

The Sobol indices for C_L, $C_{D_{\text{press}}}$, and $C_{D_{\text{sf}}}$ agree well with the Sobol indices in the original analyses. The results for the reduced-dimensionality analyses are included in Tables 5.14, 5.15, and 5.16. As with the transonic bump, the ranking of importance of the closure coefficients for each quantity is mostly the same between the original and reduced-dimensionality analyses. Even when the ranking of importance is not the same, the actual numeric values of the Sobol indices in the reduced-dimensionality analyses are still reasonably close to their corresponding values in the original analyses.

Pressure coefficient plots were generated for each turbulence model. Each of the plots contains data for the baseline case; UQ training cases (green lines); the minimum and maximum C_p bounds; and experimental data from Cook et al. [21]. Cook et al. did not report any experimental uncertainty, so the experimental results are included

Table 5.12: RAE 2822 Drag Coefficient Results, in Drag Counts (RDA).

	Baseline C_D		Min C_D		Max C_D		
Model	CFD	Resp. Surf.	CFD	Difference	Resp. Surf.	CFD	Difference
SA	146.0	134.7	135.8	0.81%	152.8	151.2	1.06%
W2006	142.3	130.2	128.5	1.32%	144.4	144.4	0.00%
SST	128.5	107.2	112.1	4.37%	183.0	182.8	0.11%

Table 5.13: RAE 2822 Lift Coefficient Results (RDA).

	Baseline C_L		Min C_L		Max C_L		
Model	CFD	Resp. Surf.	CFD	Difference	Resp. Surf.	CFD	Difference
SA	0.744	0.735	0.739	0.57%	0.769	0.764	0.69%
W2006	0.744	0.733	0.738	0.68%	0.749	0.748	0.13%
SST	0.744	0.710	0.719	1.18%	0.778	0.774	0.45%

Table 5.14: Sobol Indices of Closure Coefficients for C_L of RAE 2822 (RDA).

SA		W2006		SST	
Coefficient	Sobol Index	Coefficient	Sobol Index	Coefficient	Sobol Index
κ	5.09×10^{-1}	C_{lim}	8.96×10^{-1}	a_1	5.21×10^{-1}
c_{t4}	2.18×10^{-1}	β^*	9.93×10^{-2}	β^*/β_2	3.27×10^{-1}
c_{t3}	1.81×10^{-1}	σ_w	1.84×10^{-2}	β^*	2.81×10^{-1}
c_{v1}	1.03×10^{-1}			β^*/β_1	1.10×10^{-1}
σ	2.83×10^{-2}			σ_{w1}	4.48×10^{-2}
c_{b1}	2.60×10^{-2}				
c_{w2}	2.23×10^{-2}				

Table 5.15: Sobol Indices of Closure Coefficients for $C_{D_{\text{press}}}$ of RAE 2822 (RDA).

SA		W2006		SST	
Coefficient	Sobol Index	Coefficient	Sobol Index	Coefficient	Sobol Index
σ	4.55×10^{-1}	C_{lim}	7.01×10^{-1}	β^*	6.64×10^{-1}
c_{b1}	2.24×10^{-1}	β^*	1.82×10^{-1}	β^*/β_2	2.02×10^{-1}
c_{w2}	2.23×10^{-1}	σ_w	1.64×10^{-1}	a_1	1.77×10^{-1}
c_{t4}	5.26×10^{-2}			β^*/β_1	5.15×10^{-2}
κ	4.27×10^{-2}			σ_{w1}	2.19×10^{-2}
c_{v1}	3.19×10^{-2}				
c_{t3}	2.17×10^{-2}				

as reference only. The C_p versus x plots are included in Figs. 5.5a, 5.5c, and 5.5e; and the Sobol indices for C_p versus x are included in Figs. 5.5b, 5.5d, and 5.5f. For clarity, only the Sobol indices of coefficients with significant contributions to uncertainty in C_p are shown in the figures. Similarly to the transonic bump, the minimum and maximum C_p curves Figs. 5.5a, 5.5c, and 5.5e are piece-wise combinations of the NIPC response surfaces and cases run at the corners of the hypercubes defined by the epistemic bounds of the closure coefficients in the shock region.

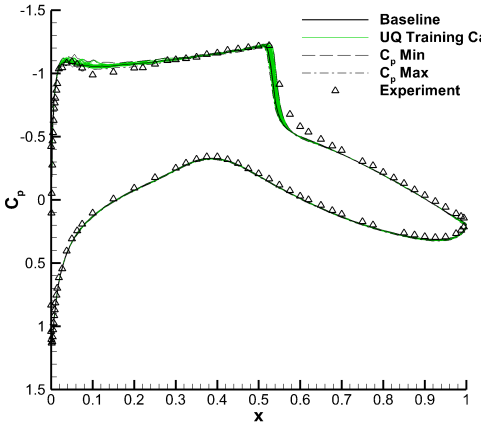

(a) C_p versus x (SA).

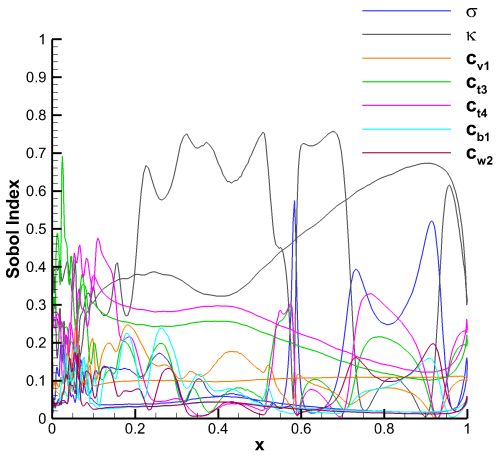

(b) Sobol indices for C_p versus x (SA).

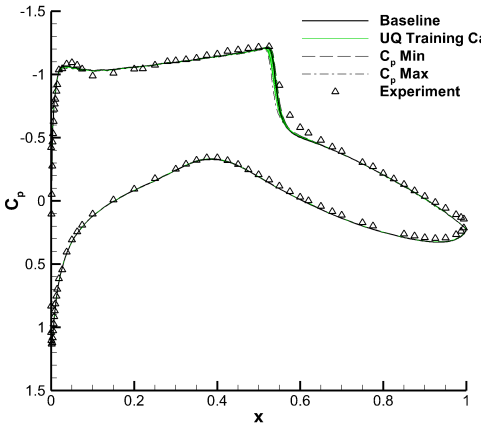

(c) C_p versus x (W2006).

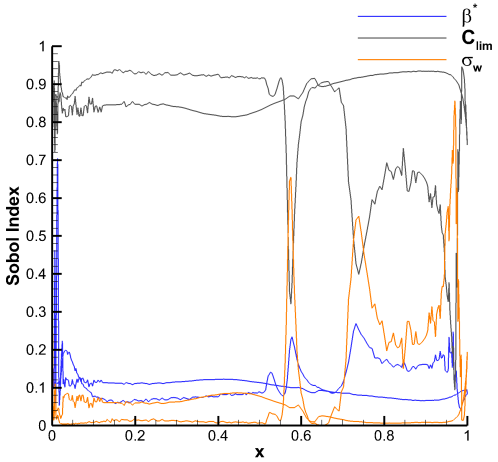

(d) Sobol indices for C_p versus x (W2006).

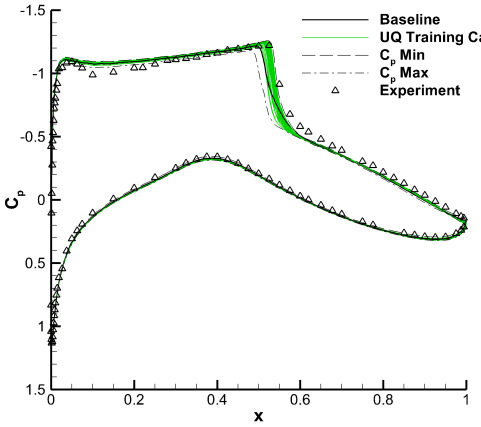

(e) C_p versus x (SST).

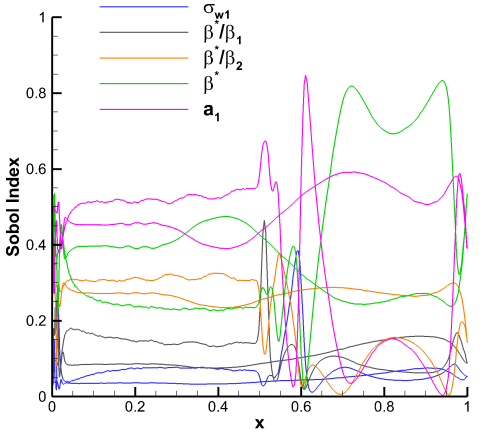

(f) Sobol indices for C_p versus x (SST).

Figure 5.5: Pressure coefficient results for RAE 2822.

Table 5.16: Sobol Indices of Closure Coefficients for $C_{D_{\text{sf}}}$ of RAE 2822 (RDA).

SA		W2006		SST	
Coefficient	Sobol Index	Coefficient	Sobol Index	Coefficient	Sobol Index
κ	5.69×10^{-1}	σ_w	6.92×10^{-1}	β^*	7.91×10^{-1}
σ	2.33×10^{-1}	C_{lim}	2.10×10^{-1}	σ_{w1}	1.15×10^{-1}
c_{w2}	8.30×10^{-2}	β^*	1.45×10^{-1}	β^*/β_1	9.10×10^{-2}
c_{t4}	4.25×10^{-2}			a_1	1.09×10^{-2}
c_{v1}	4.05×10^{-2}			β^*/β_2	3.68×10^{-3}
c_{t3}	3.52×10^{-2}				
c_{b1}	1.89×10^{-2}				

Based on the reduced-dimensionality results, all of the coefficients found to be significant to the RAE 2822 airfoil in Section 5.3 are indeed significant to their respective turbulence models. Of the three models, the SST model is most sensitive to changes in its closure coefficients, as evidenced by its larger variations in C_L, $C_{D_{\text{press}}}$, and $C_{D_{\text{sf}}}$, and by its larger solution band for C_p compared to the SA and W2006 models. The SA and W2006 models are roughly equally sensitive to changes in their closure coefficients, with the latter particularly insensitive. All of the models are most sensitive to changes in their closure coefficients in the shock region; everywhere else, there is very little uncertainty in C_p.

5.5. COMPARISON OF UNCERTAINTY QUANTIFICATION RESULTS BETWEEN THE TWO CFD CASES

The uncertainty quantification and sensitivity results of the axisymmetric transonic bump and RAE 2822 airfoil are consistent with one another. For the W2006 and SST models, every closure coefficient which is significant to at least one output quantity of interest for the transonic bump is also significant to at least one output quantity of interest for the RAE 2822 and vice versa. This agreement is nearly observed by the SA model as well, with only one coefficient significant to the transonic

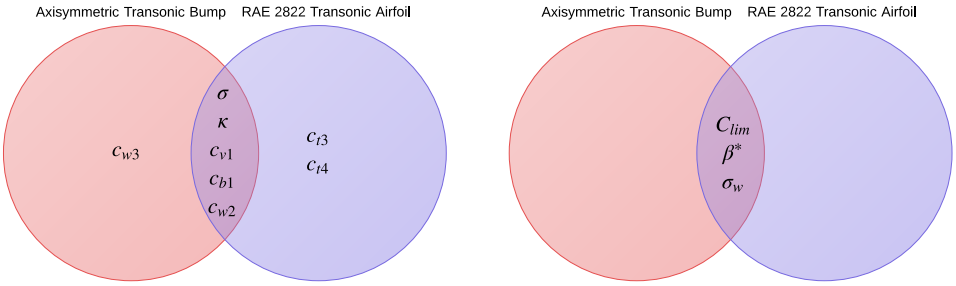

(a) SA - Significant closure coefficients. (b) W2006 - Significant closure coefficients.

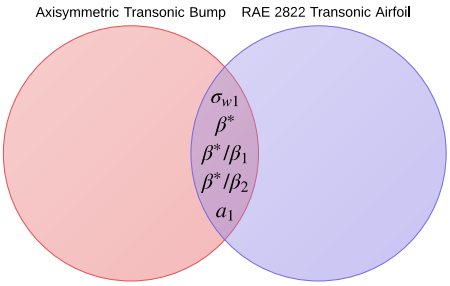

(c) SST - Significant closure coefficients.

Figure 5.6: Closure coefficients significant to uncertainty in at least one output quantity of interest for each CFD problem and for each turbulence model.

bump but not the RAE 2822, and only two coefficients significant to the RAE 2822, but not the transonic bump. A summary of all of the significant closure coefficients is included in Fig. 5.6.

Note that for the SA model, c_{w3} was only significant to uncertainty in the separation bubble size for the transonic bump. Also, in the Sobol index distribution for C_f with the SA model (Fig. 5.1b), the peak in the Sobol index of c_{w3} occurs at the same x-location as the local maximum of C_f within the separation bubble. The RAE 2822 does not feature a separation bubble; this explains why c_{w3} was not significant for that problem. The significance of c_{t3} and c_{t4} to uncertainty for the RAE 2822 is explained in Section 6.9 of the case study.

Compared to the transonic bump results, the RAE 2822 results are much less sensitive to changes in all three turbulence models' closure coefficients. The same trends still apply however; the SST model is most sensitive to changes in its closure coefficients, and the SA and W2006 models are roughly equally sensitive to changes in their closure coefficients. Uncertainties in C_p are particularly large in the shock region of each flow for all three turbulence models.

The information presented in this chapter is expected to be of interest to the CFD community because it demonstrates that large changes in turbulence model behavior can be observed by changing specific sets of closure coefficients. In particular, there are two main results that can enable the advancement of turbulence models used in RANS simulations. The first result is that if improved matching between CFD and experiments (i.e., the data representing the real physical phenomena) is desired, the Sobol indices presented in this chapter for certain output quantities of interest give clues for which closure coefficients to modify first. The second result is that if the aerospace community can reduce the uncertainty in only a certain set of closure coefficients (whether through experimentation, LES/DES, etc.), the uncertainty in turbulence model predictions can be greatly reduced. For example, the uncertainty in the value of Von Kármán's constant in the SA model was responsible for approximately 85% of the uncertainty in C_D of the axisymmetric transonic bump. If more information were known about the true value of κ, the results of the SA model would be much less uncertain.

If improved accuracy is desired, a good starting point may be to first consider the integrated quantities; that is, C_D for the axisymmteric transonic bump, and C_L, $C_{D_{\text{press}}}$, and $C_{D_{\text{sf}}}$ for the RAE 2822 airfoil. Referring back to Tables 5.6, 5.14, 5.15, and 5.16, a small number of closure coefficients can be identified for each turbulence model which consistently contribute to very large amounts to uncertainty in the output quantities of interest. These coefficients include κ and σ for the SA model; C_{lim} and

σ_w for the W2006 model; and β^* for the SST model. This result is in agreement with the work done by Godfrey and Cliff [5], Edeling et al. [13], and Papadimitriou and Papadimitriou [14]. It is suggested that these coefficients be considered first in future refinements of the turbulence models discussed here.

6. RESULTS OF CASE STUDY

In this chapter, the results of all RAE 2822 uncertainty quantification analyses for the case study are presented. These results were obtained during a summer internship at The Boeing Company, and they have been cleared for release under RROI 15-00615-EOT. The FUN3D results for the coarse, fine, med-tri, and unstr-m grids are presented in Sections 6.1-6.4 respectively. The BCFD results for the SA model with the original medium, unstr-m, and unstr-f grids are presented in Sections 6.5-6.7 respectively. A summary of the case study results is included in Section 6.8. All results are compared to the FUN3D results for the original medium grid in Section 5.4. The SA model results require additional explanation, which is included in Section 6.9. Only the coefficients found to contribute most significantly to uncertainty for the RAE 2822 in the main study are treated as uncertain in the proceeding analyses; recall that these coefficients are listed in Table 5.11.

As in the main study, Sobol indices were used in the case study to rank the relative contributions of each closure coefficient to the overall uncertainty in the output quantities of interest for the RAE 2822, which include the lift coefficient (C_L), drag coefficient due to pressure ($C_{D_{\text{press}}}$), and drag coefficient due to skin friction ($C_{D_{\text{sf}}}$). Recall that coefficients with higher Sobol indices contribute more to the uncertainty than coefficients with lower Sobol indices.

Pressure coefficient plots were also generated for each analysis, and are included in the proceeding sections. Each of the plots contains data for the baseline case (with the original set of closure coefficients); UQ training cases (green lines); the minimum and maximum C_p bounds; and experimental data from Cook et al. [21]. The minimum and maximum C_p bounds were calculated from response surfaces at each chord-wise

position along the airfoil. Sobol index distributions for C_p were also calculated and plotted from these response surfaces. Cook et al. did not report any experimental uncertainty, so the experimental results are included as reference only.

In some analyses, additional CFD cases were run at the corners of the hypercube defined by the epistemic interval bounds of only the most significant closure coefficients; this was done to eliminate the effect of discontinuities in the response surfaces near the shock and to determine the epistemic uncertainty interval for C_p in the shock region only. In these instances, the C_p minimum and maximum curves are piece-wise combinations of the NIPC response surface and the hypercube cases in the shock region.

6.1. COARSE GRID (FUN3D)

The Sobol indices for C_L, $C_{D_{\text{press}}}$, and $C_{D_{\text{sf}}}$ with the coarse grid are included in Tables A.1, A.2, and A.3 of Appendix A respectively. The C_p distributions and corresponding Sobol index distributions are included in Fig. 6.1.

For the SA model, the most significant coefficients for the integrated quantities from the original medium grid remain as the most significant for the coarse grid; however c_{t3} and c_{t4} have significantly decreased importance. The general shape of the coarse grid C_p Sobol index distribution remains similar to that of the original medium grid. Although the curves for c_{t3} and c_{t4} are noticably smaller, the regions where κ and σ contribute significantly to uncertainty in C_p are the same; κ dominates uncertainty until just aft of the shock, where σ has a large spike near $x = 0.6$. Then κ rises again until approximately $x = 0.7$, where σ has increased significance until approximately $x = 0.9$.

For the W2006 model, the results for the integrated quantities with the coarse grid are consistent with the results from the original medium grid. The distributions of Sobol indices for C_p are also very similar.

For the SST model, the results for the coarse grid are inconsistent with the results from the original medium grid. Note that the sum of the Sobol indices for each integrated quantity for the SST model is much larger than one; this indicates significant mixed contributions to uncertainty between coefficients. Although the C_p distribution for the coarse grid appears to be similar to the C_p distribution for the original medium grid, the Sobol index distributions for C_p are completely different. One possible reason for the discrepancy between results is that the SST model is known to be sensitive to near-wall spacing [32]. Furthermore, Menter recommends $\Delta y^+ < 3$ to simulate a smooth wall boundary condition [18]; however the maximum value of y^+ for the coarse grid is larger than four.

6.2. FINE GRID (FUN3D)

The Sobol indices for C_L, $C_{D_{\text{press}}}$, and $C_{D_{\text{sf}}}$ with the fine grid are included in Tables A.4, A.5, and A.6 of Appendix A respectively. The C_p distributions and corresponding Sobol index distributions are included in Fig. 6.2.

For the SA model, c_{t3} and c_{t4} have significantly increased importance for the integrated quantities. This observation is explained in Section 6.9. Note that in Fig. 6.2a a small number of UQ samples is set apart from the others in the shock region; it was determined that these cases feature c_{t3} and c_{t4} near their maximum and minimum epistemic bounds respectively, yielding large values for f_{t2}. The Sobol index distribution for C_p with the fine grid is completely dominated by c_{t3}, then c_{t4}.

For the W2006 and SST models, the results for the integrated quantities with the fine grid are consistent with the results from the original medium grid. The distributions of Sobol indices for C_p are also very similar.

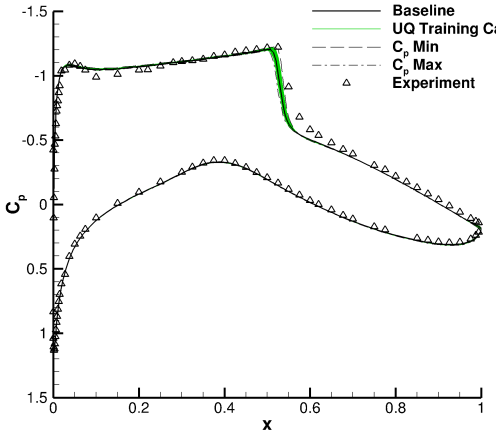

(a) C_p versus x (SA).

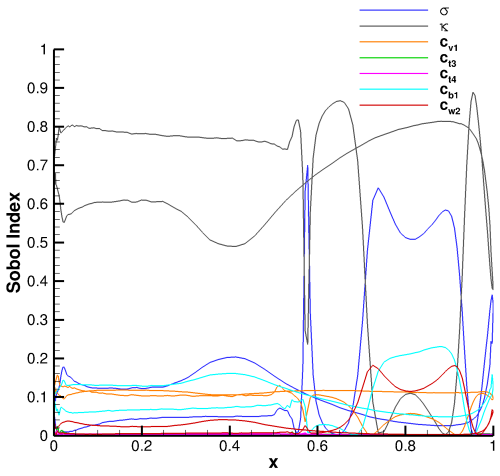

(b) Sobol indices for C_p versus x (SA).

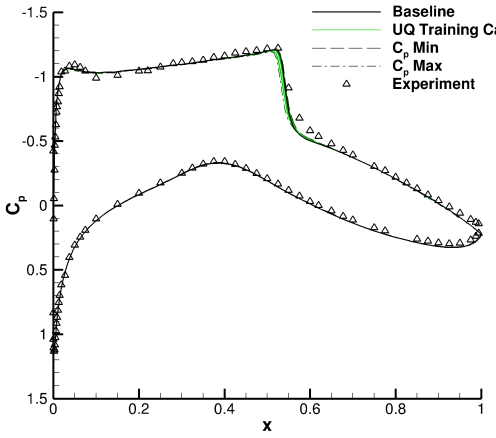

(c) C_p versus x (W2006).

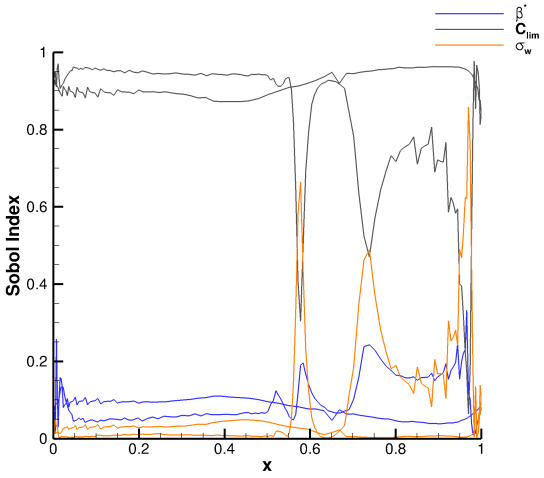

(d) Sobol indices for C_p versus x (W2006).

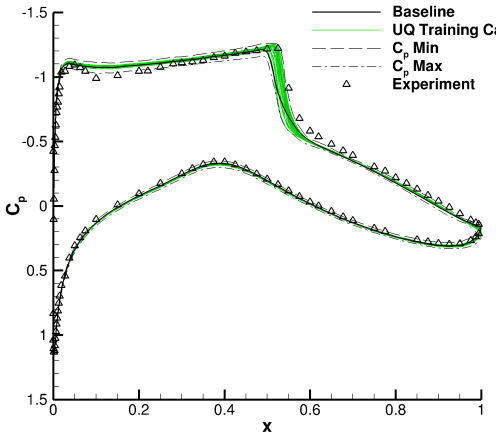

(e) C_p versus x (SST).

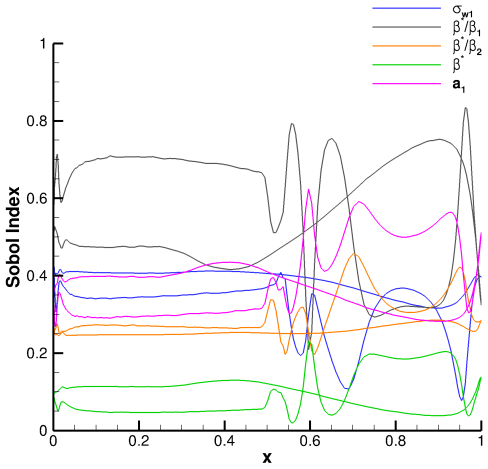

(f) Sobol indices for C_p versus x (SST).

Figure 6.1: Pressure coefficient results for RAE 2822, coarse grid (FUN3D)

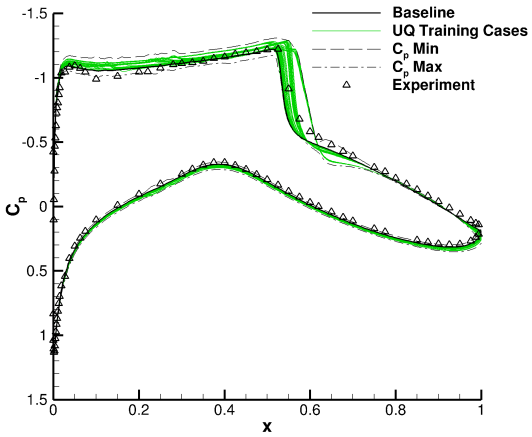

(a) C_p versus x (SA).

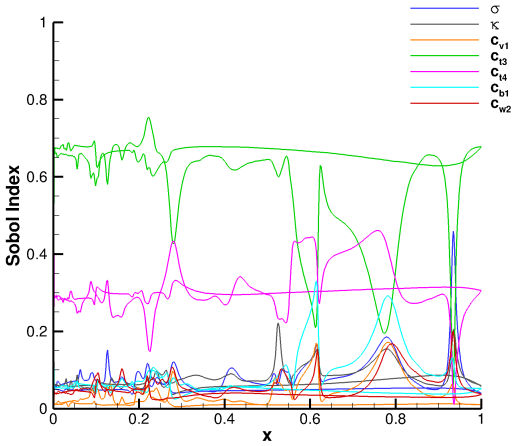

(b) Sobol indices for C_p versus x (SA).

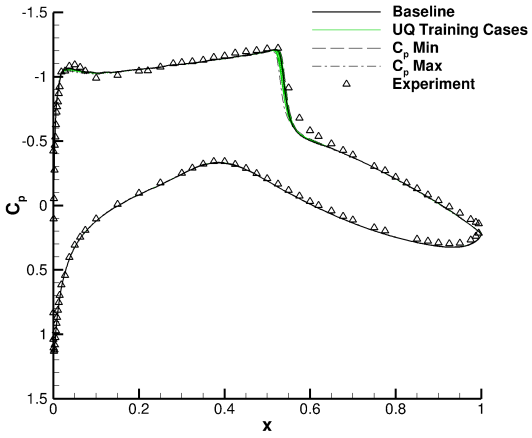

(c) C_p versus x (W2006).

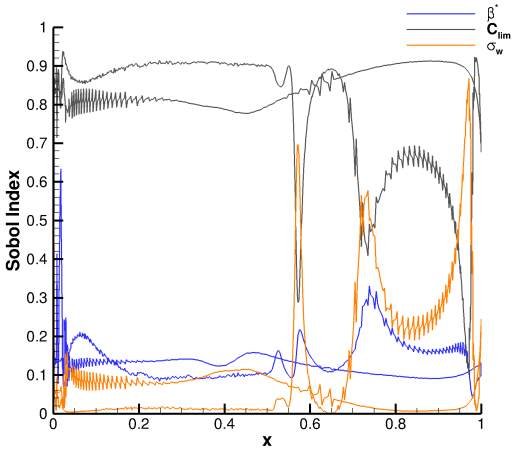

(d) Sobol indices for C_p versus x (W2006).

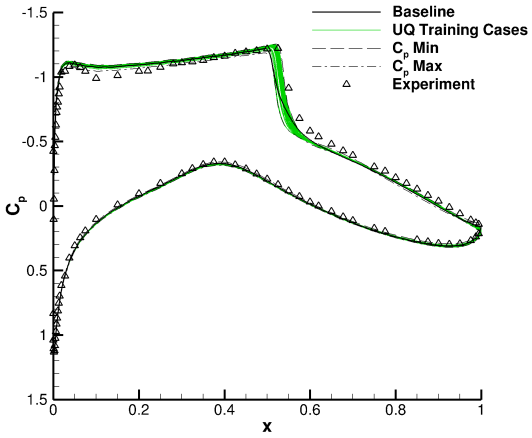

(e) C_p versus x (SST).

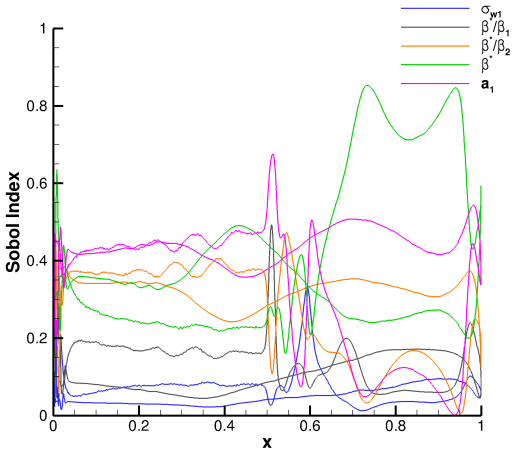

(f) Sobol indices for C_p versus x (SST).

Figure 6.2: Pressure coefficient results for RAE 2822, fine grid (FUN3D)

6.3. MED-TRI GRID (FUN3D)

The Sobol indices for C_L, $C_{D_{\text{press}}}$, and $C_{D_{\text{sf}}}$ with the med-tri grid are included in Tables A.7, A.8, and A.9 of Appendix A respectively. The C_p distributions and corresponding Sobol index distributions are included in Fig. 6.3.

For the SA model, the most significant coefficients for the integrated quantities with the original medium grid remain as the most significant coefficients with the med-tri grid; however c_{t4} has decreased importance. The C_p and corresponding Sobol index distributions for the med-tri grid are very similar to those of the original medium grid.

For the W2006 model, the results for the integrated quantities with the med-tri grid are consistent with the results from the original medium grid. The distributions of Sobol indices for C_p are also very similar.

For the SST model, the results for C_L and $C_{D_{\text{sf}}}$ with the med-tri grid are consistent with the results from original medium grid. The results for $C_{D_{\text{press}}}$ are also similar, except that a_1 has increased significance for the med-tri grid. The Sobol index distribution for C_p with med-tri grid is even more dominated by a_1 than the distribution with the original medium grid, but the rise in importance of β^* aft of the shock and back to the training edge is still present.

6.4. UNSTR-M GRID (FUN3D)

The Sobol indices for C_L, $C_{D_{\text{press}}}$, and $C_{D_{\text{sf}}}$ with the unstr-m grid are included in Tables A.10, A.11, and A.12 of Appendix A respectively. The C_p distributions and corresponding Sobol index distributions are included in Fig. 6.4.

For all three turbulence models, the results for the integrated quantities with the unstr-m grid are in very good agreement with the results from the original medium grid. In fact, the percent of the total uncertainty in each integrated quantity due to each coefficient only varies by approximately 2% at most between the two grids (see

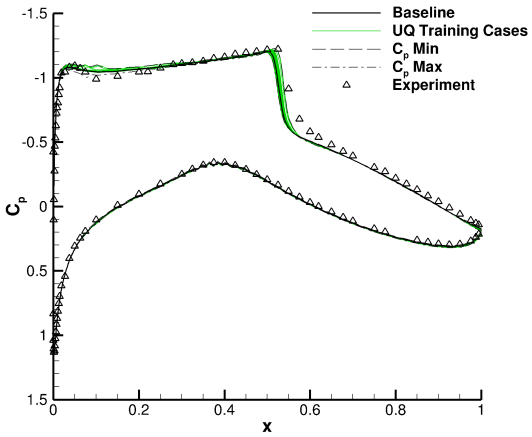

(a) C_p versus x (SA).

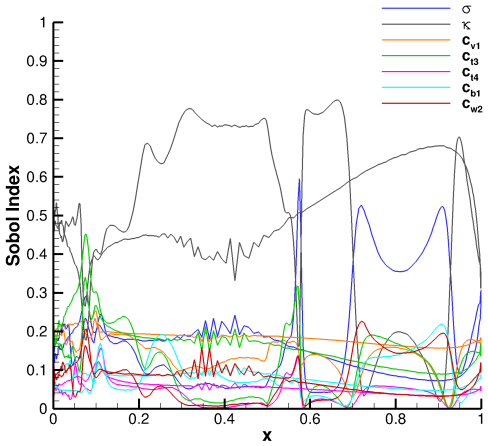

(b) Sobol indices for C_p versus x (SA).

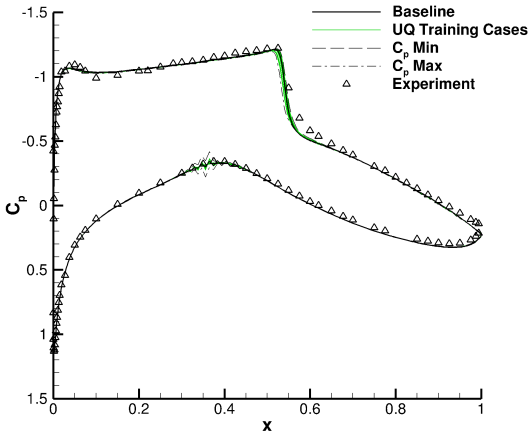

(c) C_p versus x (W2006).

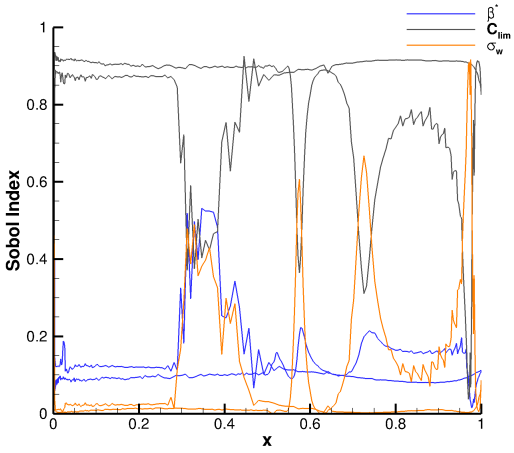

(d) Sobol indices for C_p versus x (W2006).

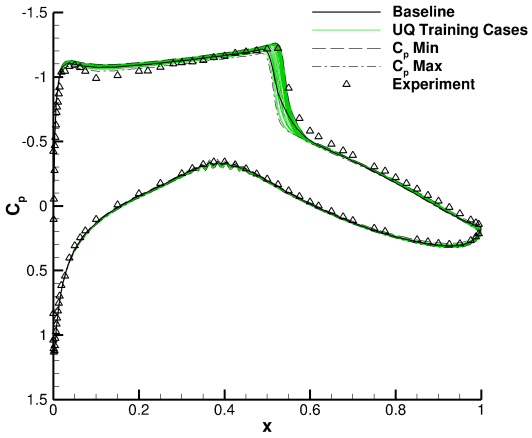

(e) C_p versus x (SST).

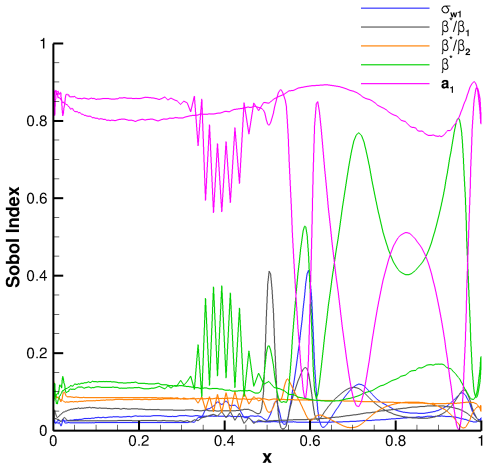

(f) Sobol indices for C_p versus x (SST).

Figure 6.3: Pressure coefficient results for RAE 2822, med-tri grid (FUN3D)

the $C_{D_{\text{press}}}$ values for C_{lim} in the W2006 model), and in most cases this variation is much less. The distributions of Sobol indices for C_p are also very similar between the unstr-m grid and the original medium grid, especially for the W2006 and SST models.

6.5. ORIGINAL MEDIUM GRID (BCFD)

The Sobol indices for C_L, $C_{D_{\text{press}}}$, and $C_{D_{\text{sf}}}$ with the original medium grid in BCFD are included in Table A.13 of Appendix A. Recall that only the the SA model was run in BCFD. The C_p distribution and corresponding Sobol index distribution are included in Fig. 6.5.

The most significant coefficients for the integrated quantities from the original medium grid in FUN3D remain as the most significant for the original medium grid in BCFD; however c_{t3} and c_{t4} have significantly decreased importance. Very good agreement is observed, however, between the integrated quantity results with coarse grid in FUN3D and the original medium grid in BCFD. The C_p and Sobol index distributions with the original medium grid in BCFD also agree well with those of the coarse grid in FUN3D . This agreement is explained in Section 6.9.

6.6. UNSTR-M GRID (BCFD)

The Sobol indices for C_L, $C_{D_{\text{press}}}$, and $C_{D_{\text{sf}}}$ with the unstr-m grid in BCFD are included in Table A.14 of Appendix A. The C_p distribution and corresponding Sobol index distribution are included in Fig. 6.6. The results for the unstr-m grid in BCFD are very similar for the results for the original medium grid in BCFD – although these results are different than results for the original medium grid in FUN3D , they are similar to the results for the coarse grid in FUN3D .

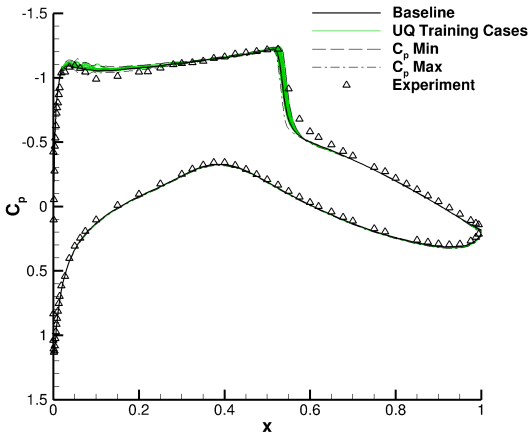

(a) C_p versus x (SA).

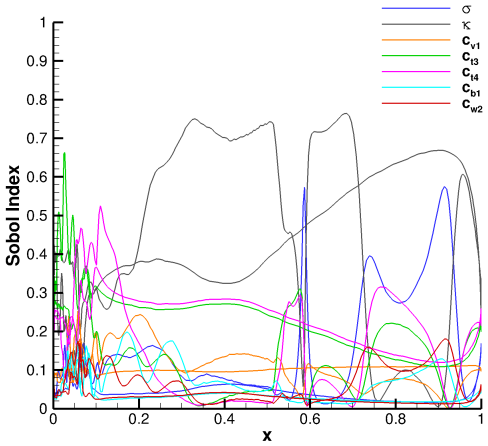

(b) Sobol indices for C_p versus x (SA).

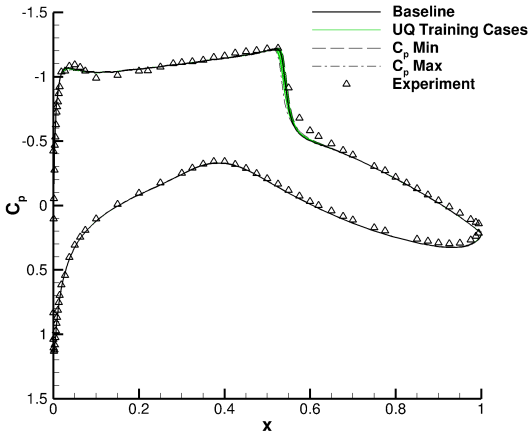

(c) C_p versus x (W2006).

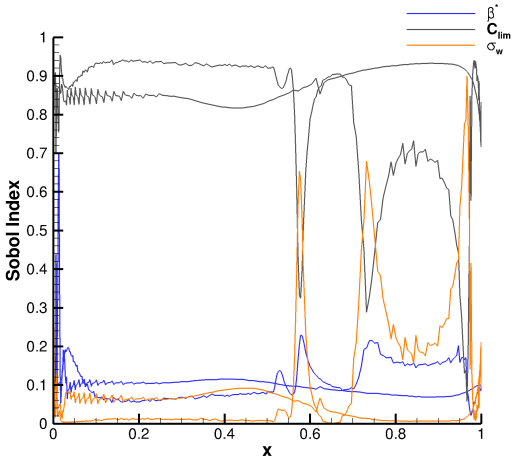

(d) Sobol indices for C_p versus x (W2006).

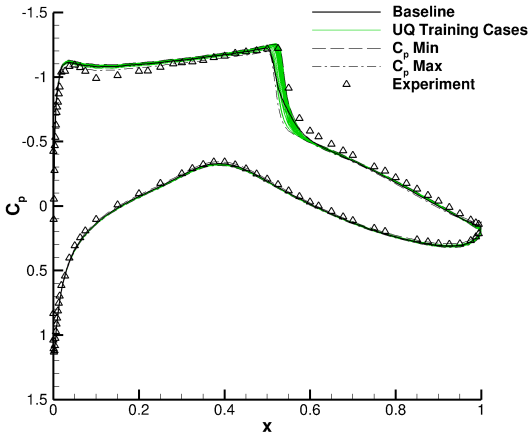

(e) C_p versus x (SST).

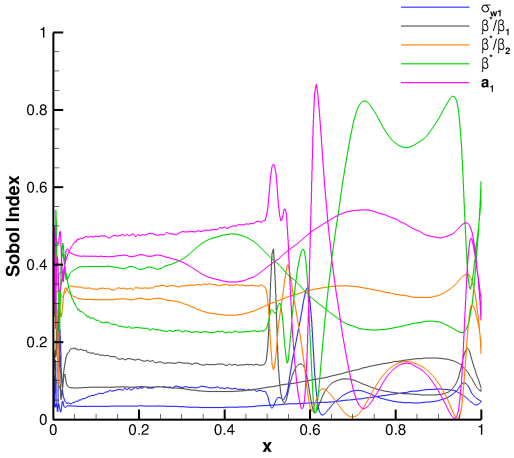

(f) Sobol indices for C_p versus x (SST).

Figure 6.4: Pressure coefficient results for RAE 2822, unstr-m grid (FUN3D)

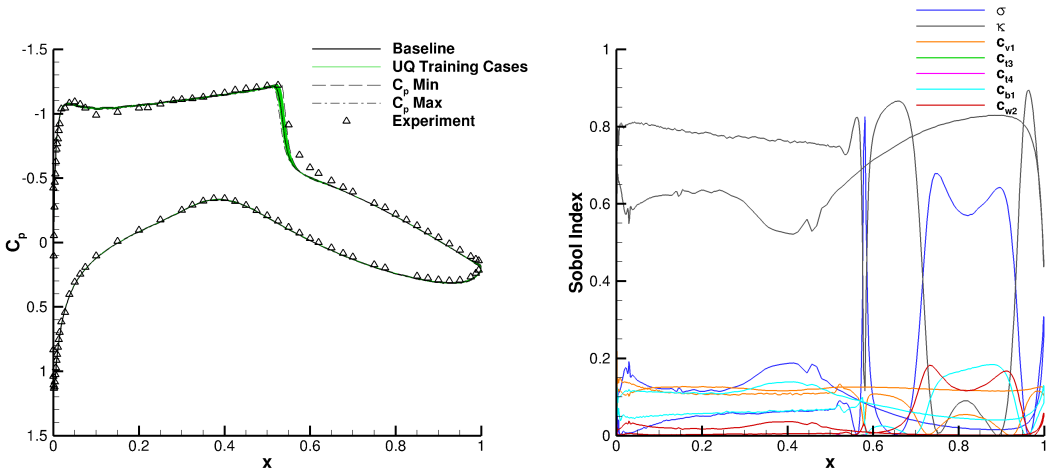

(a) C_p versus x (SA). (b) Sobol indices for C_p versus x (SA).

Figure 6.5: Pressure coefficient results for RAE 2822, original medium grid (BCFD)

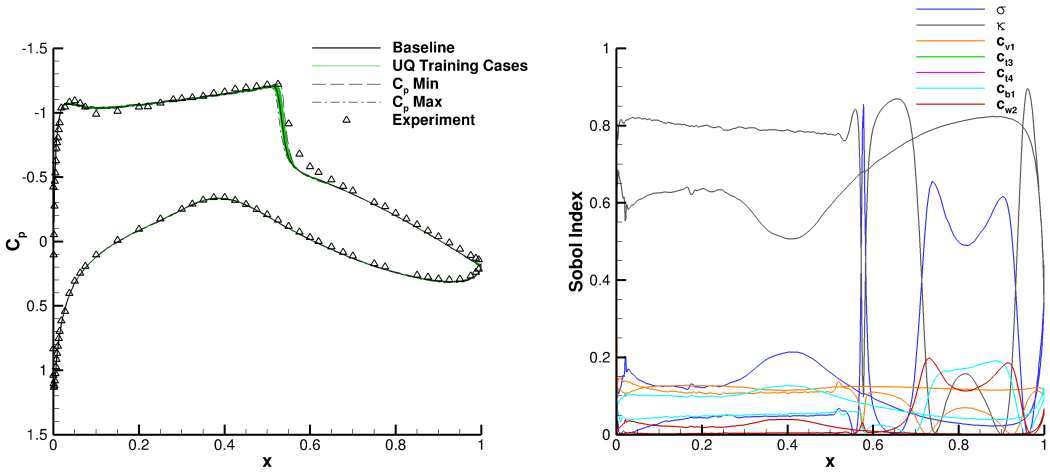

(a) C_p versus x (SA). (b) Sobol indices for C_p versus x (SA).

Figure 6.6: Pressure coefficient results for RAE 2822, unstr-m grid (BCFD)

6.7. UNSTR-F GRID (BCFD)

The Sobol indices for C_L, $C_{D_{\text{press}}}$, and $C_{D_{\text{sf}}}$ with the unstr-f grid in BCFD are included in Table A.15 of Appendix A. The C_p distribution and corresponding Sobol index distribution are included in Fig. 6.7. The results for the unstr-f grid in BCFD

are very similar for the results for the original medium and unstr-m grids in BCFD – although these results are different than results for the original medium grid in FUN3D , they are similar to the results for the coarse grid in FUN3D .

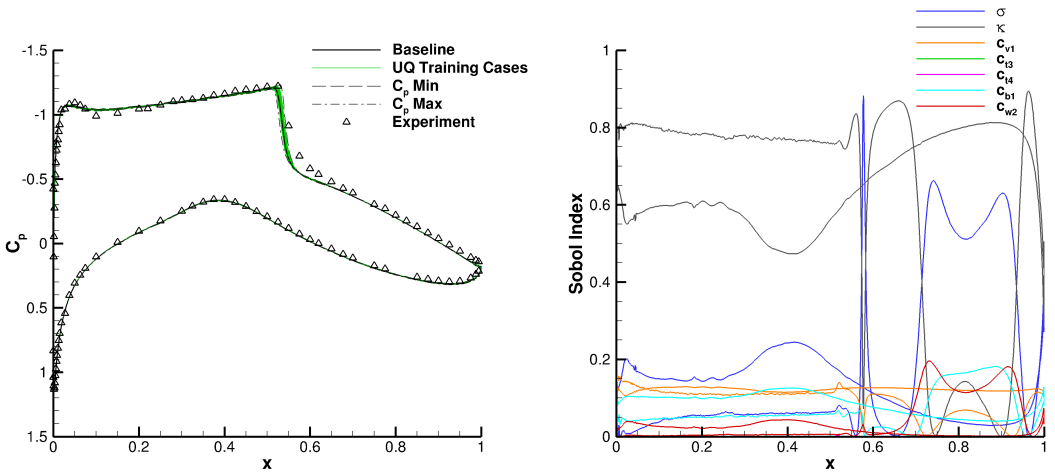

(a) C_p versus x (SA). (b) Sobol indices for C_p versus x (SA).

Figure 6.7: Pressure coefficient results for RAE 2822, unstr-f grid (BCFD)

6.8. SUMMARY OF CASE STUDY RESULTS

To better compare results across all grids, Figs. 6.8, 6.9, and 6.10 were created to show the Sobol indices of the integrated quantities for each turbulence model and for each grid. Each of the vertical lines in the figures shows the dispersion of Sobol indices for a particular flow quantity and turbulence model. Note the consistency of the results; for the SA model, only the fine grid features large discrepancies from the other SA results, and for the SST model, only the coarse grid features large discrepancies from the other SST results. There are no major differences between any of the W2006 results.

The main focus of the case study was to verify the sensitivity information presented in Section 5.4, however for completeness the minimum and maximum C_L and C_D calculated from the response surfaces of each grid and each turbulence model are included in Tables B.1 and B.2 of Appendix B. As expected, the minimum and maximum C_L and C_D results in Tables B.1 and B.2 that agree best with the original medium grid results correspond to analyses that have good agreement between Sobol indices.

Overall, the FUN3D results presented in the case study are in good agreement with the results from Section 5.4. Of all the results from the case study grids, the SST results from the coarse grid were most different than those of the original medium grid. This should be expected however, as the coarse grid is of the lowest quality of all the case study grids (specifically, it features very high aspect ratio cells near the wall). The results from the fine grid with the SA model indicate significantly increased importance of c_{t3} and c_{t4} compared to the original medium grid, and this finding is explained in Section 6.9.

The most significant coefficients for the SA model with the original medium grid in FUN3D remain as the most significant for all three of the grids run in BCFD; however c_{t3} and c_{t4} have decreased importance compared to the original results. The BCFD results are in good agreement with the results obtained with the coarse grid in FUN3D. These findings are also explained in Section 6.9.

6.9. EXPLANATION OF SA MODEL BEHAVIOR

Overall the case study results for the SA model are in good agreement; however there are clearly differences in the results of the fine grid with FUN3D compared to those of the original medium grid. Additionally, the coarse grid results show a slight decrease in the importance of c_{t3} and c_{t4} compared to the results of the original

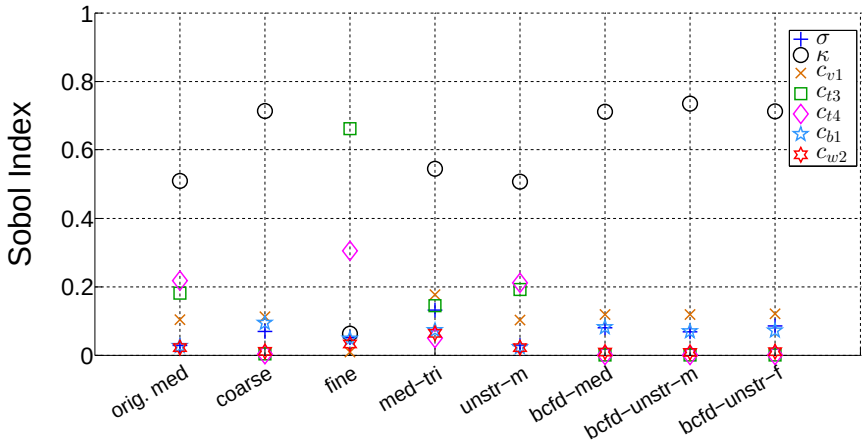

(a) Sobol Indices for C_L (SA).

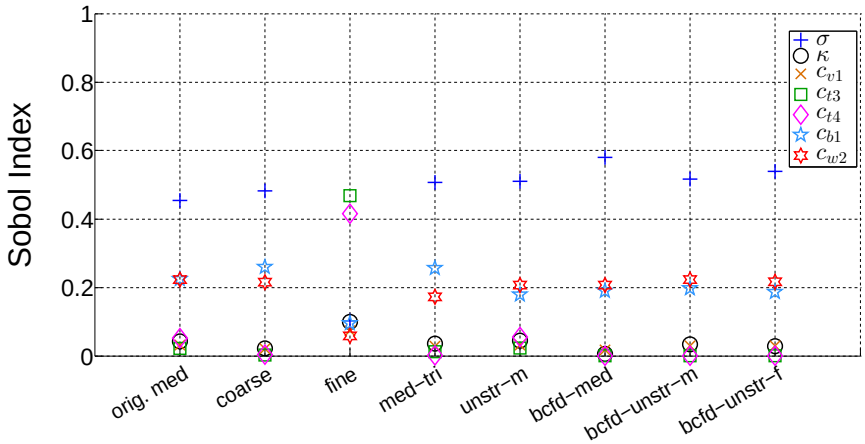

(b) Sobol Indices for $C_{D_{\text{press}}}$ (SA).

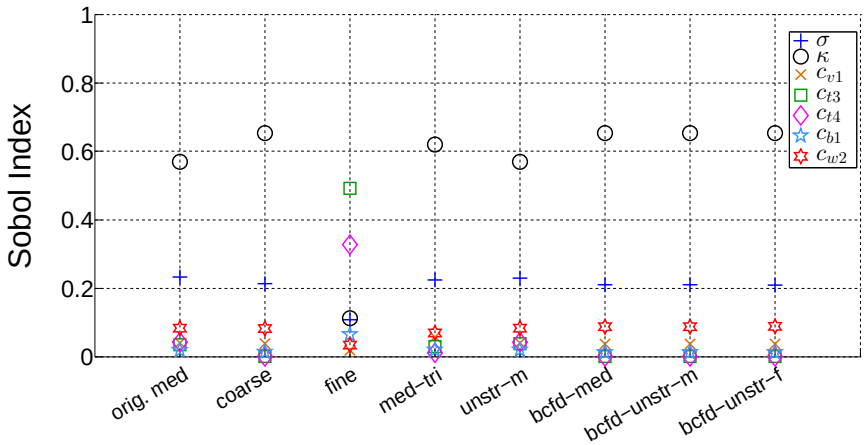

(c) Sobol Indices for $C_{D_{\text{sf}}}$ (SA).

Figure 6.8: Sobol indices of integrated quantities for all grids (SA).

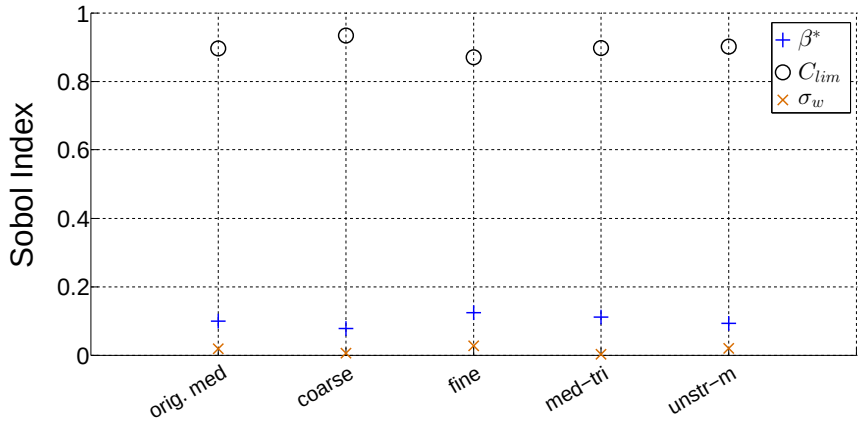

(a) Sobol Indices for C_L (W2006).

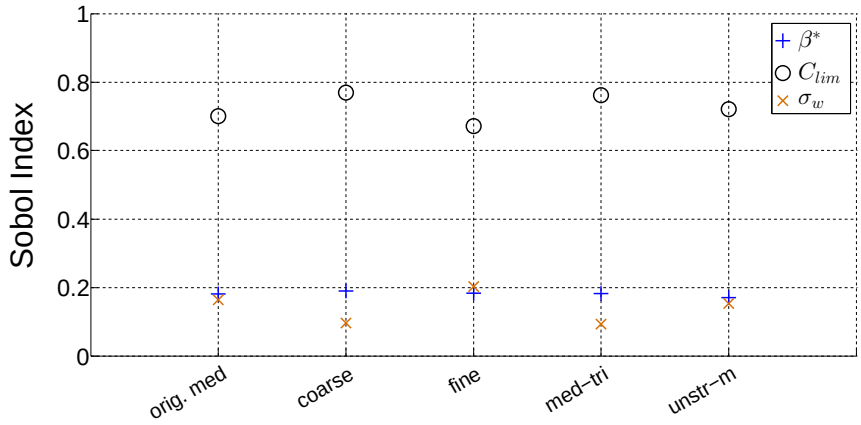

(b) Sobol Indices for $C_{D_{\text{press}}}$ (W2006).

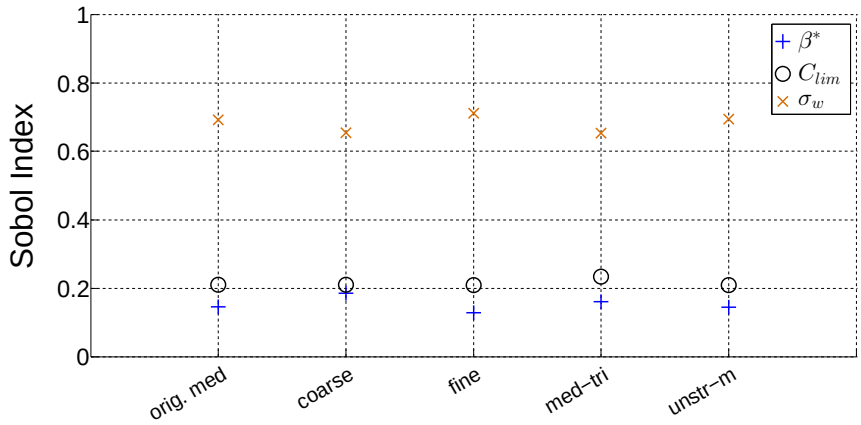

(c) Sobol Indices for $C_{D_{\text{sf}}}$ (W2006).

Figure 6.9: Sobol indices of integrated quantities for all grids (W2006).

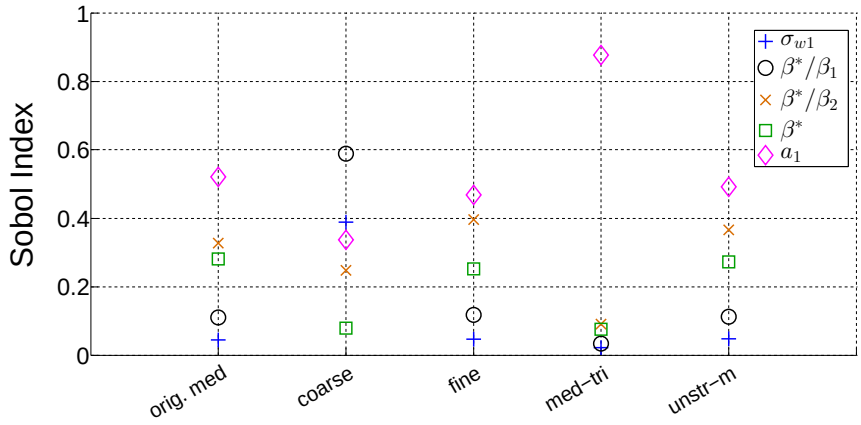

(a) Sobol Indices for C_L (SST).

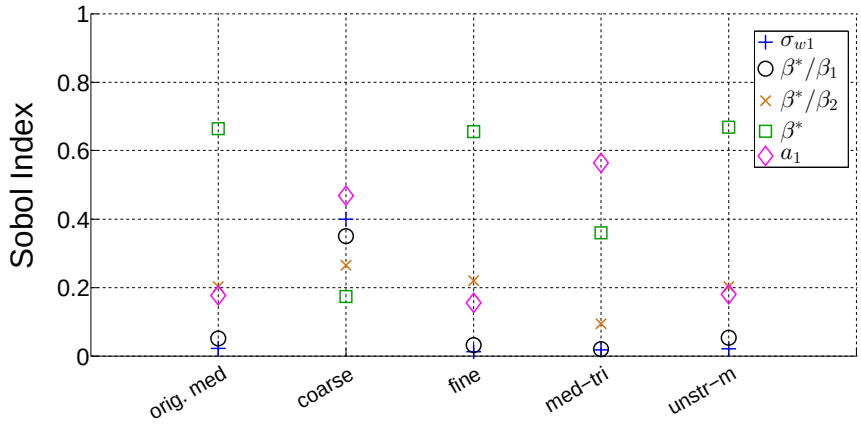

(b) Sobol Indices for $C_{D_{\text{press}}}$ (SST).

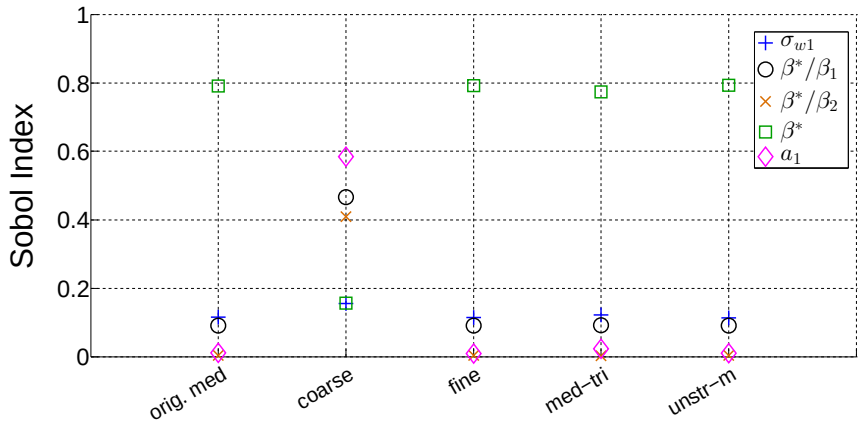

(c) Sobol Indices for $C_{D_{\text{sf}}}$ (SST).

Figure 6.10: Sobol indices of integrated quantities for all grids (SST).

medium grid, and this behavior is also observed in the BCFD results. All of these observations are explained by the f_{t2} function in the SA model, which appears in both the production and destruction terms.

FUN3D uses the "standard" implementation of the SA model as described by [1]. BCFD employs a slightly different, but very common implementation of the model in which f_{t2} is set to zero. The production and destruction terms are, respectively:

$$c_{b1}\left(1 - f_{t2}\right)\hat{S}\hat{\nu} \tag{44}$$

$$-\left[c_{w1}f_w - \frac{c_{b1}}{\kappa^2}f_{t2}\right]\left(\frac{\hat{\nu}}{d}\right)^2 \tag{45}$$

where

$$\hat{S} = \Omega + \frac{\hat{\nu}}{\kappa^2 d^2}f_{v2} \tag{46}$$

$$f_{t2} = c_{t3}\exp\left(-c_{t4}\chi^2\right) \tag{47}$$

Notice that both Eqns. (44) and (45) contain $(\hat{\nu}/d)^2$, where d is the normal wall distance; as d approaches zero, $(1/d)^2$ becomes very large. Also notice that on the edges of the epistemic intervals for c_{t3} and c_{t4} (see Table 3.1), f_{t2} can grow very large compared to its value with the baseline coefficients as χ increases in the boundary layer. A plot depicting the ratio of the perturbed f_{t2} to the baseline value for varying χ is included in Fig. 6.11.

The purpose of the f_{t2} function is to act as an attractor so that $\hat{\nu} = 0$ is a solution for the SA model ($\hat{\nu} = 0$ should be a solution at the wall). When f_{t2} is large and d is small, the attraction becomes so strong that the flow begins to laminarize. This is illustrated in Figure 6.12. For the baseline case in Fig. 6.12a, the non-dimensional values of $\hat{\nu}$ at the wall on the upper surface are larger than the freestream, indicating turbulent flow. Contrastingly, the non-dimensional values of $\hat{\nu}$ on the wall are the

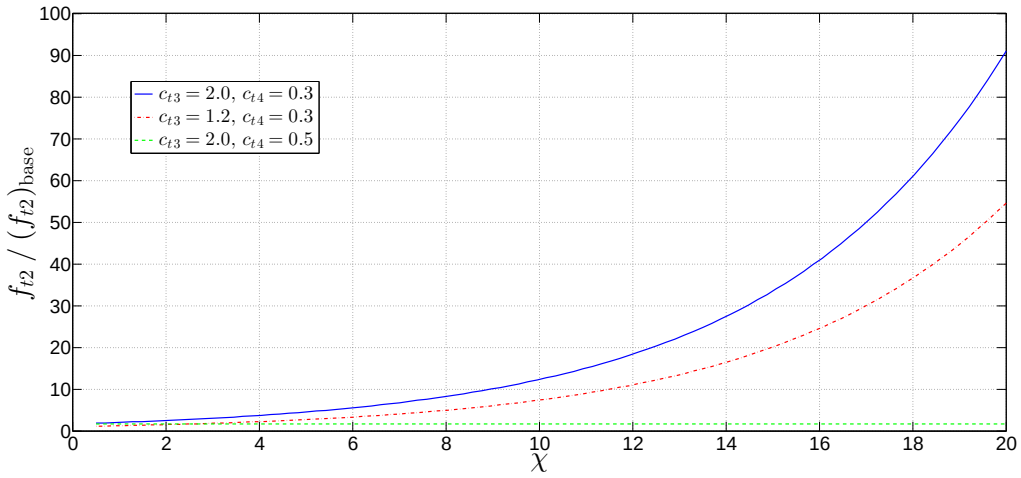

Figure 6.11: $f_{t2}/\left(f_{t2}\right)_{\text{baseline}}$ versus χ for combinations of c_{t3} and c_{t4}

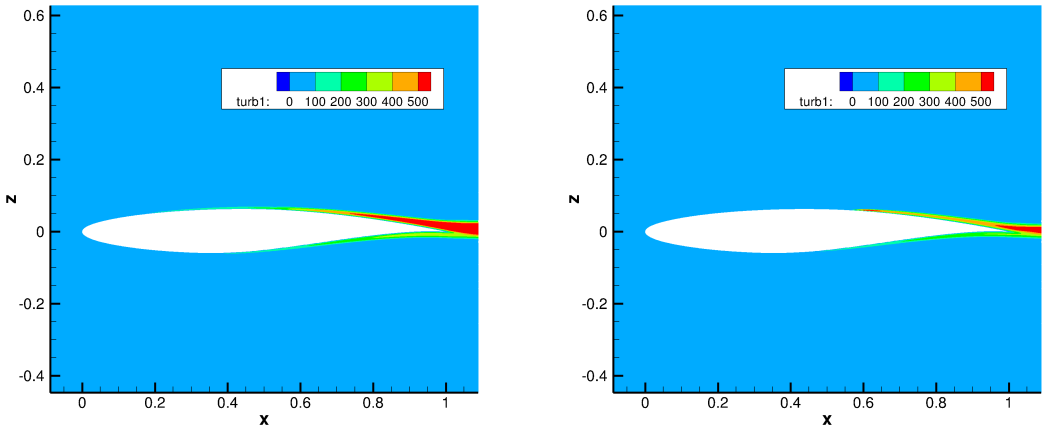

(a) Baseline case, fine grid.

(b) Case 9, fine grid.

Figure 6.12: Contours of $\hat{\nu}$ (non-dimensionalized) for fine grid.

same as the freestream for UQ Case 9 (Fig. 6.12b), indicating laminar flow before the shock at approximately $x = 0.6$. The fine grid has a small d because the first grid point is very close to the surface; Case 9 has a large c_{t3} and small c_{t4}.

The laminarization of Case 9 explains why the C_p plot in Fig. 6.2a features a small group of UQ cases set apart from the rest (recall that each of these cases has large c_{t3} and small c_{t4}). The rearward shifting of the shock and subsequent flat region are indicative of a laminar shock wave, which is in agreement with the observations made in Fig. 6.12.

Note that this laminarization can be observed for coarser grids as well. In additional CFD runs, laminarization started to occur near the leading edge for the original medium grid with very large c_{t3} (outside of the epistemic interval) and small c_{t4}. This observation explains the large contributions of c_{t3} and c_{t4} to uncertainty the C_p distribution near the leading edge of the original medium grid in Fig. 5.5b.

These findings explain why c_{t3} and c_{t4} have significantly larger Sobol indices for all output quantities of interest for the fine grid than for all other grids. As $(\hat{\nu}/d)$ grows large deep in the boundary layer, it is multiplied by f_{t2} which can also be large for large c_{t3} and small c_{t4}. For the fine grid, $(\hat{\nu}/d)$ becomes especially large because d is at least twice as small as for the other grids; thus laminarization occurs much more readily, and its occurrence is sensitive to c_{t3} and c_{t4}.

One way to avoid laminarization all together is to simply set $f_{t2} = 0$. Doing so should yield UQ and sensitivity results similar to those obtained with the coarse grid in FUN3D (where large d mitigates the effects of f_{t2}) and similar to the results of all grids in BCFD (where f_{t2} is already set to zero). To verify this statement, two additional UQ analyses were performed using FUN3D: one with the original medium grid and one with the fine grid. f_{t2} was set to zero in both analyses.

Figs. 6.13 and 6.14 show the pressure coefficient and corresponding Sobol index distributions for the original medium and fine grids with $f_{t2} = 0$. Figs. 6.13b and 6.14b have the same shape as Figs. 6.1b, 6.5b, 6.6b, and 6.7b; this confirms that setting f_{t2} to zero yields consistent UQ and sensitivity results. Furthermore,

Fig. 6.15 shows consistent integrated quantity results for the $f_{t2} = 0$ analyses when compared to the coarse grid in FUN3D and all grids in BCFD. The Sobol indices for the integrated quantities with $f_{t2} = 0$ in FUN3D are included in Tables A.16 and A.17 of Appendix A. The epistemic intervals of C_L and C_D are reported in Tables B.1 and B.2 of Appendix B respectively. The epistemic intervals for C_L and C_D for the analyses with $f_{t2} = 0$ are in very good agreement with each other, as well as with the coarse grid results.

Finally, the observations made in this section explain why c_{t3} and c_{t4} are significant to uncertainty for the RAE 2822, but not the transonic bump (see Fig. 5.6a). As d grows smaller, c_{t3} and c_{t4} grow more significant to uncertainty; the transonic bump has a wall spacing of 6×10^{-6} grid units, which is 20% larger than that of the original medium grid for the RAE 2822.

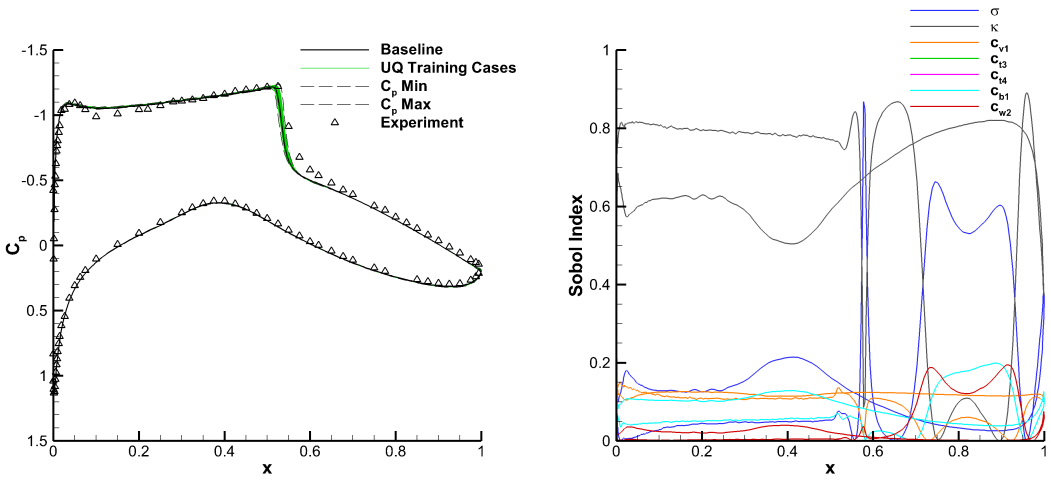

(a) C_p versus x (SA). (b) Sobol indices for C_p versus x (SA).

Figure 6.13: Pressure coefficient results for RAE 2822, original medium grid, $f_{t2} = 0$ (FUN3D).

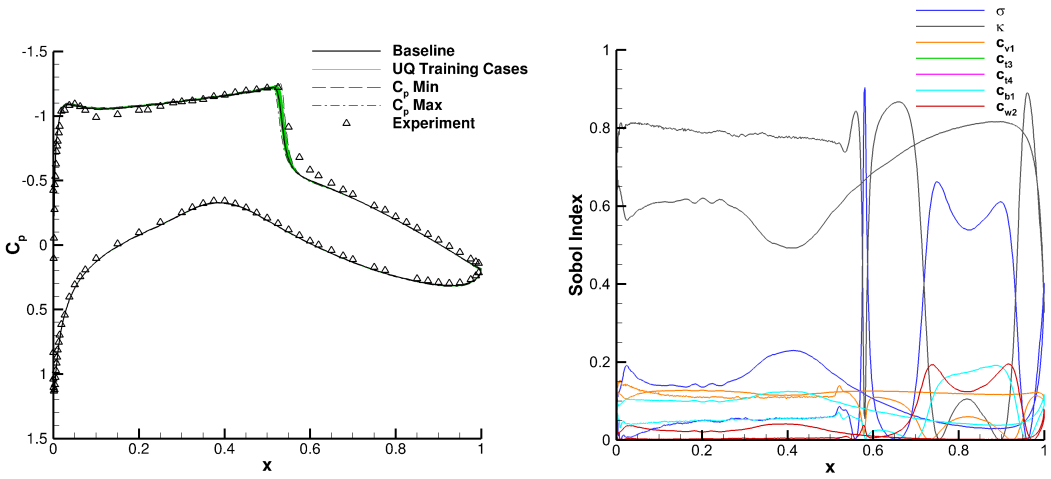

(a) C_p versus x (SA). (b) Sobol indices for C_p versus x (SA).

Figure 6.14: Pressure coefficient results for RAE 2822, fine grid, $f_{t2} = 0$ (FUN3D).

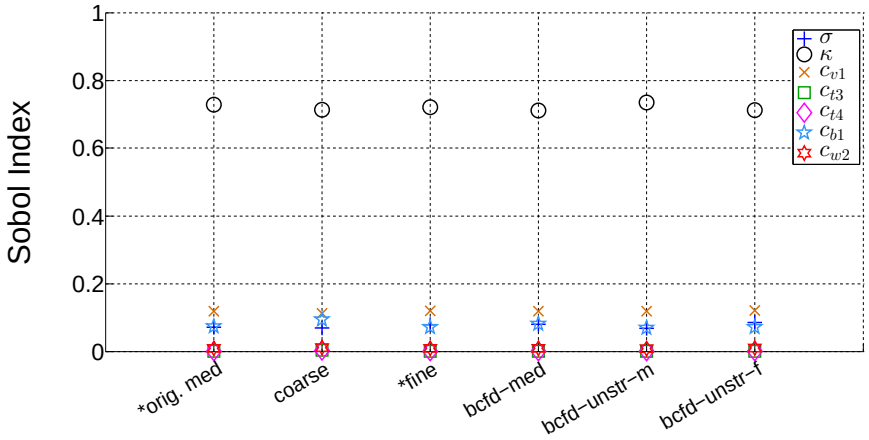

(a) Sobol Indices for C_L (SA).

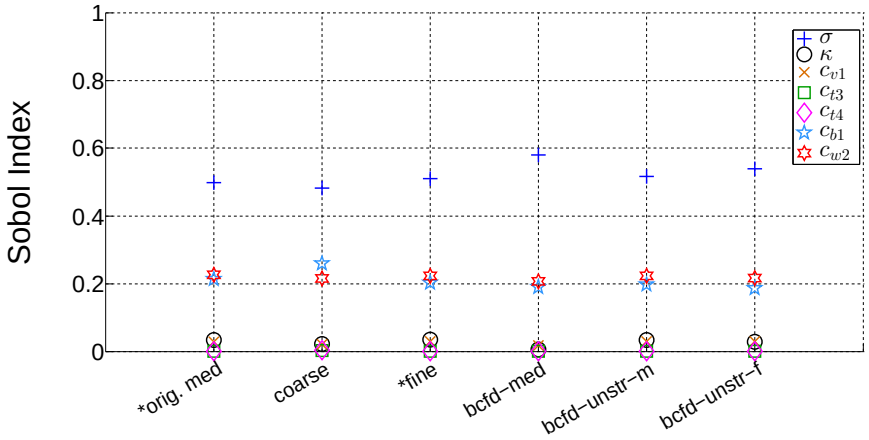

(b) Sobol Indices for $C_{D_{\text{press}}}$ (SA).

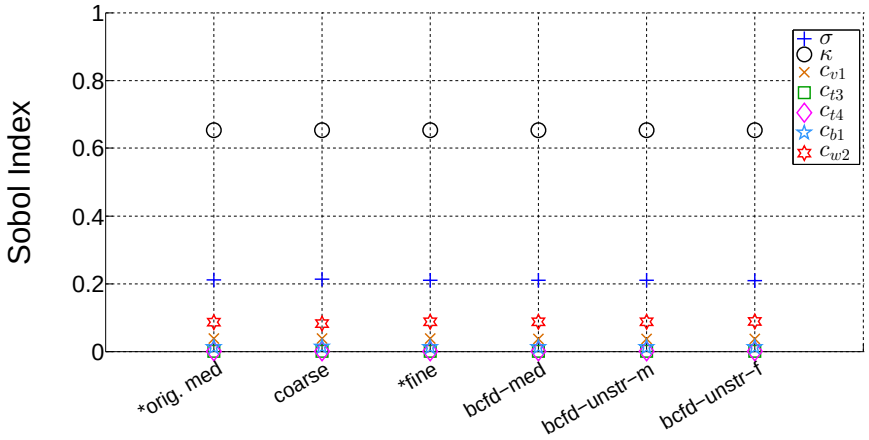

(c) Sobol Indices for $C_{D_{\text{sf}}}$ (SA).

*indicates a FUN3D analysis with f_{t2} set to zero

Figure 6.15: Sobol indices of integrated quantities with $f_{t2} = 0$ (SA).

7. CONCLUSIONS AND FUTURE WORK

Two studies were performed to quantify the uncertainty in commonly used turbulence models due to uncertainties in the values of their closure coefficients. The conclusions from these studies are presented in this chapter.

In the main study, two detailed uncertainty quantification analyses were performed on an axisymmetric transonic bump at zero degrees angle of attack and the RAE 2822 transonic airfoil at a lift coefficient of 0.744. The transonic bump has freestream $M = 0.875$ and $Re = 2.763 \times 10^6$, and the RAE 2822 has freestream $M = 0.729$ and $Re = 6.5 \times 10^6$. The turbulence models considered were the Spalart-Allmaras Model, Wilcox (2006) k-ω Model, and Menter Shear-Stress Transport Model. The uncertainty quantification employed stochastic expansions based on non-intrusive polynomial chaos as an efficient means of uncertainty propagation. The drag coefficient, wall pressure and skin friction coefficient distributions, and shock-induced separation bubble size were considered as uncertain outputs for the transonic bump. The lift coefficient, pressure and skin friction components of drag coefficient, and wall pressure coefficient distribution were considered as uncertain outputs for the RAE 2822. Sobol indices were used to rank the relative contributions of each closure coefficient to the total uncertainty in the output quantities of interest. This information can be used a potential starting point in the future advancement of the turbulence models considered here, and it is a first step towards quantifying model-form uncertainty.

Based on the results of the main study, the following conclusions can be made: For the SA model, the coefficients that contribute most to uncertainty in the output quantities of interest are σ, κ, c_{v1}, c_{b1}, c_{w2}, c_{t3}, c_{t4}, and c_{w3}. For the W2006 model, the coefficients that contribute most to uncertainty in the output quantities of interest

are β^*, C_{lim}, and σ_w. For the SST model, the coefficients that contribute most to uncertainty in the output quantities of interest are σ_{w1}, β^*/β_1, β^*/β_2, β^*, and a_1. With the exception of c_{w3}, c_{t3}, and c_{t4} in the SA model, all other closure coefficients were found to be significant to both the axisymmetric transonic bump and RAE 2822 transonic airfoil. For the SA model, c_{w3} was only significant to uncertainty in the separation bubble region of the transonic bump; the RAE 2822 does not have a separation region, which is why c_{w3} was not significant for that problem.

In the case study, several more UQ analyses were performed to confirm the RAE 2822 sensitivity results of the main study with computational grids of varying resolution and topology. The same UQ methodology was used in both the main study and the case study. The W2006 results of the case study are extremely consistent across all grids. The SST results are mostly consistent except for the results of the coarse grid; however the SST model is known to be sensitive to near-wall resolution. The SA results were mostly consistent except for the results of the fine grid, which had a sharp increase in the importance of c_{t3} and c_{t4}.

It was determined that for the SA model, the coupling of large c_{t3}, small c_{t4}, and small wall-normal spacing can lead to laminarization of the flow on the upper surface of the RAE 2822 before the shock. This led to the formation of a laminar shock wave in several UQ training cases, and it produced physically unrealistic results for the fine grid analysis. Laminarization increases as the wall-normal distance decreases; this explains why c_{t3} and c_{t4} were significant to uncertainty for the RAE 2822 airfoil, but not the transonic bump (which has a larger wall-normal spacing than the RAE 2822) in the main study. In the case study, it was demonstrated that by setting f_{t2} to zero, grid independence of the SA UQ and sensitivity results is achieved.

The consistency of the sensitivity results in the case study leads to the conclusion that, based on the epistemic intervals for the closure coefficients established here, there are a small subset of coefficients for each model that are responsible for the

majority of the uncertainty in the output quantities of interest, independent of grid resolution or topology. Future work should focus increasing knowledge of appropriate values for these coefficients, which includes κ and σ for the SA model; C_{lim} and σ_w for the W2006 model; and β^* for the SST model. Improved knowledge of the values of these particular closure coefficients will have the largest impact on reducing the uncertainty in integrated quantities of interest for the RANS simulations of wall-bounded transonic flows. Future work should also focus on determining why certain closure coefficients contribute more or less to uncertainty at different flow locations. For example, research should be done to determine why σ in the SA model becomes important to C_f for the transonic bump after the reattachment point, but not before. Finally, future work should include more CFD problems, particularly in three dimensions.

APPENDIX A

Sobol Indices of Integrated Quantities (Case Study)

This appendix includes the tabulated Sobol indices for C_L, $C_{D_{\text{press}}}$, and $C_{D_{\text{sf}}}$ with each of the case study grids, turbulence models, and flow solvers. Coefficients which contribute significantly to uncertainty are typset in blue.

Table A.1: Sobol indices for C_L, coarse grid (FUN3D).

SA		W2006		SST	
Coefficient	Sobol Index	Coefficient	Sobol Index	Coefficient	Sobol Index
κ	7.13×10^{-1}	C_{lim}	9.34×10^{-1}	β^*/β_1	5.89×10^{-1}
c_{v1}	1.12×10^{-1}	β^*	7.81×10^{-2}	σ_{w1}	3.89×10^{-1}
c_{b1}	9.43×10^{-2}	σ_w	6.04×10^{-3}	a_1	3.37×10^{-1}
σ	6.95×10^{-2}			β^*/β_2	2.48×10^{-1}
c_{w2}	1.10×10^{-2}			β^*	7.92×10^{-2}
c_{t3}	3.25×10^{-3}				
c_{t4}	3.04×10^{-3}				

Table A.2: Sobol indices for $C_{D_{\text{press}}}$, coarse grid (FUN3D).

SA		W2006		SST	
Coefficient	Sobol Index	Coefficient	Sobol Index	Coefficient	Sobol Index
σ	4.82×10^{-1}	C_{lim}	7.70×10^{-1}	a_1	4.68×10^{-1}
c_{b1}	2.60×10^{-1}	β^*	1.90×10^{-1}	σ_{w1}	3.99×10^{-1}
c_{w2}	2.15×10^{-1}	σ_w	9.65×10^{-2}	β^*/β_1	3.50×10^{-1}
κ	2.19×10^{-2}			β^*/β_2	2.65×10^{-1}
c_{v1}	2.10×10^{-2}			β^*	1.73×10^{-1}
c_{t4}	3.57×10^{-3}				
c_{t3}	2.88×10^{-3}				

Table A.3: Sobol indices for $C_{D_{\text{sf}}}$, coarse grid (FUN3D).

SA		W2006		SST	
Coefficient	Sobol Index	Coefficient	Sobol Index	Coefficient	Sobol Index
κ	6.54×10^{-1}	σ_w	6.54×10^{-1}	a_1	5.84×10^{-1}
σ	2.14×10^{-1}	C_{lim}	2.10×10^{-1}	β^*/β_1	4.66×10^{-1}
c_{w2}	8.26×10^{-2}	β^*	1.85×10^{-1}	β^*/β_2	4.09×10^{-1}
c_{v1}	3.85×10^{-2}			β^*	1.57×10^{-1}
c_{b1}	1.33×10^{-2}			σ_{w1}	1.56×10^{-1}
c_{t3}	4.27×10^{-5}				
c_{t4}	1.78×10^{-5}				

Table A.4: Sobol indices for C_L, fine grid (FUN3D).

SA		W2006		SST	
Coefficient	Sobol Index	Coefficient	Sobol Index	Coefficient	Sobol Index
c_{t3}	6.62×10^{-1}	C_{lim}	8.71×10^{-1}	a_1	4.68×10^{-1}
c_{t4}	3.05×10^{-1}	β^*	1.24×10^{-1}	β^*/β_2	3.96×10^{-1}
κ	6.31×10^{-2}	σ_w	2.76×10^{-2}	β^*	2.52×10^{-1}
σ	5.08×10^{-2}			β^*/β_1	1.17×10^{-1}
c_{b1}	4.82×10^{-2}			σ_{w1}	4.71×10^{-2}
c_{w2}	3.31×10^{-2}				
c_{v1}	8.76×10^{-3}				

Table A.5: Sobol indices for $C_{D_{\text{press}}}$, fine grid (FUN3D).

SA		W2006		SST	
Coefficient	Sobol Index	Coefficient	Sobol Index	Coefficient	Sobol Index
c_{t3}	4.68×10^{-1}	C_{lim}	6.72×10^{-1}	β^*	6.55×10^{-1}
c_{t4}	4.16×10^{-1}	σ_w	2.03×10^{-1}	β^*/β_2	2.20×10^{-1}
σ	1.03×10^{-1}	β^*	1.84×10^{-1}	a_1	1.56×10^{-1}
κ	9.95×10^{-2}			β^*/β_1	3.13×10^{-2}
c_{b1}	9.52×10^{-2}			σ_{w1}	1.23×10^{-2}
c_{v1}	7.34×10^{-2}				
c_{w2}	5.82×10^{-2}				

Table A.6: Sobol indices for $C_{D_{\text{sf}}}$, fine grid (FUN3D).

SA		W2006		SST	
Coefficient	Sobol Index	Coefficient	Sobol Index	Coefficient	Sobol Index
c_{t3}	4.92×10^{-1}	σ_w	7.11×10^{-1}	β^*	7.92×10^{-1}
c_{t4}	3.28×10^{-1}	C_{lim}	2.09×10^{-1}	σ_{w1}	1.14×10^{-1}
κ	1.12×10^{-1}	β^*	1.28×10^{-1}	β^*/β_1	9.07×10^{-2}
σ	1.08×10^{-1}			a_1	9.67×10^{-3}
c_{b1}	6.53×10^{-2}			β^*/β_2	3.82×10^{-3}
c_{w2}	3.37×10^{-2}				
c_{v1}	1.87×10^{-2}				

Table A.7: Sobol indices for C_L, med-tri grid (FUN3D).

SA		W2006		SST	
Coefficient	Sobol Index	Coefficient	Sobol Index	Coefficient	Sobol Index
κ	5.44×10^{-1}	C_{lim}	8.97×10^{-1}	a_1	8.77×10^{-1}
c_{v1}	1.77×10^{-1}	β^*	1.11×10^{-1}	β^*/β_2	9.10×10^{-2}
c_{t3}	1.44×10^{-1}	σ_w	2.83×10^{-3}	β^*	7.57×10^{-2}
σ	1.32×10^{-1}			β^*/β_1	3.33×10^{-2}
c_{b1}	7.23×10^{-2}			σ_{w1}	2.19×10^{-2}
c_{w2}	6.39×10^{-2}				
c_{t4}	5.02×10^{-2}				

Table A.8: Sobol indices for $C_{D_{\text{press}}}$, med-tri grid (FUN3D).

SA		W2006		SST	
Coefficient	Sobol Index	Coefficient	Sobol Index	Coefficient	Sobol Index
σ	5.07×10^{-1}	C_{lim}	7.62×10^{-1}	a_1	5.64×10^{-1}
c_{b1}	2.56×10^{-1}	β^*	1.82×10^{-1}	β^*	3.59×10^{-1}
c_{w2}	1.73×10^{-1}	σ_w	9.35×10^{-2}	β^*/β_2	9.45×10^{-2}
κ	3.63×10^{-2}			β^*/β_1	2.02×10^{-2}
c_{v1}	2.84×10^{-2}			σ_{w1}	1.75×10^{-2}
c_{t3}	1.22×10^{-2}				
c_{t4}	1.79×10^{-3}				

Table A.9: Sobol indices for $C_{D_{\text{sf}}}$, med-tri grid (FUN3D).

SA		W2006		SST	
Coefficient	Sobol Index	Coefficient	Sobol Index	Coefficient	Sobol Index
κ	6.20×10^{-1}	σ_w	6.53×10^{-1}	β^*	7.74×10^{-1}
σ	2.24×10^{-1}	C_{lim}	2.34×10^{-1}	σ_{w1}	1.23×10^{-1}
c_{w2}	6.91×10^{-2}	β^*	1.61×10^{-1}	β^*/β_1	9.15×10^{-2}
c_{v1}	5.79×10^{-2}			a_1	2.35×10^{-2}
c_{t3}	2.91×10^{-2}			β^*/β_2	2.77×10^{-3}
c_{b1}	1.95×10^{-2}				
c_{t4}	1.18×10^{-2}				

Table A.10: Sobol indices for C_L, unstr-m grid (FUN3D).

SA		W2006		SST	
Coefficient	Sobol Index	Coefficient	Sobol Index	Coefficient	Sobol Index
κ	5.07×10^{-1}	C_{lim}	9.01×10^{-1}	a_1	4.92×10^{-1}
c_{t4}	2.12×10^{-1}	β^*	9.27×10^{-2}	β^*/β_2	3.66×10^{-1}
c_{t3}	1.92×10^{-1}	σ_w	1.97×10^{-2}	β^*	2.73×10^{-1}
c_{v1}	1.02×10^{-1}			β^*/β_1	1.13×10^{-1}
σ	2.90×10^{-2}			σ_{w1}	4.79×10^{-2}
c_{b1}	2.36×10^{-2}				
c_{w2}	2.17×10^{-2}				

Table A.11: Sobol indices for $C_{D_{\text{press}}}$, unstr-m grid (FUN3D).

SA		W2006		SST	
Coefficient	Sobol Index	Coefficient	Sobol Index	Coefficient	Sobol Index
σ	5.10×10^{-1}	C_{lim}	7.21×10^{-1}	β^*	6.68×10^{-1}
c_{w2}	2.06×10^{-1}	β^*	1.70×10^{-1}	β^*/β_2	2.02×10^{-1}
c_{b1}	1.79×10^{-1}	σ_w	1.53×10^{-1}	a_1	1.80×10^{-1}
c_{t4}	5.52×10^{-2}			β^*/β_1	5.29×10^{-2}
κ	4.48×10^{-2}			σ_{w1}	2.15×10^{-2}
c_{v1}	3.16×10^{-2}				
c_{t3}	2.34×10^{-2}				

Table A.12: Sobol indices for $C_{D_{\text{sf}}}$, unstr-m grid (FUN3D).

SA		W2006		SST	
Coefficient	Sobol Index	Coefficient	Sobol Index	Coefficient	Sobol Index
κ	5.69×10^{-1}	σ_w	6.94×10^{-1}	β^*	7.93×10^{-1}
σ	2.29×10^{-1}	C_{lim}	2.09×10^{-1}	σ_{w1}	1.14×10^{-1}
c_{w2}	8.35×10^{-2}	β^*	1.45×10^{-1}	β^*/β_1	9.08×10^{-2}
c_{t4}	4.26×10^{-2}			a_1	9.80×10^{-3}
c_{v1}	4.00×10^{-2}			β^*/β_2	3.86×10^{-3}
c_{t3}	3.78×10^{-2}				
c_{b1}	1.98×10^{-2}				

Table A.13: Sobol indices for integrated quantities with original medium grid, SA model (BCFD).

C_L		$C_{D_{\text{press}}}$		$C_{D_{\text{sf}}}$	
Coefficient	Sobol Index	Coefficient	Sobol Index	Coefficient	Sobol Index
κ	7.12×10^{-1}	σ	5.80×10^{-1}	κ	6.53×10^{-1}
c_{v1}	1.19×10^{-1}	c_{w2}	2.07×10^{-1}	σ	2.10×10^{-1}
c_{b1}	8.14×10^{-2}	c_{b1}	1.90×10^{-1}	c_{w2}	8.80×10^{-2}
σ	8.03×10^{-2}	c_{v1}	1.82×10^{-2}	c_{v1}	3.76×10^{-2}
c_{w2}	9.04×10^{-3}	κ	6.17×10^{-3}	c_{b1}	1.27×10^{-2}
c_{t3}	2.94×10^{-5}	c_{t3}	3.31×10^{-4}	c_{t3}	3.32×10^{-5}
c_{t4}	2.27×10^{-5}	c_{t4}	2.69×10^{-4}	c_{t4}	1.64×10^{-5}

Table A.14: Sobol indices for integrated quantities with unstr-m grid, SA model (BCFD).

C_L		$C_{D_{\text{press}}}$		$C_{D_{\text{sf}}}$	
Coefficient	Sobol Index	Coefficient	Sobol Index	Coefficient	Sobol Index
κ	7.35×10^{-1}	σ	5.17×10^{-1}	κ	6.53×10^{-1}
c_{v1}	1.19×10^{-1}	c_{w2}	2.23×10^{-1}	σ	2.10×10^{-1}
c_{b1}	6.97×10^{-2}	c_{b1}	1.97×10^{-1}	c_{w2}	8.79×10^{-2}
σ	6.88×10^{-2}	κ	3.36×10^{-2}	c_{v1}	3.75×10^{-2}
c_{w2}	8.09×10^{-3}	c_{v1}	2.91×10^{-2}	c_{b1}	1.28×10^{-2}
c_{t4}	2.30×10^{-5}	c_{t4}	1.03×10^{-4}	c_{t3}	3.16×10^{-5}
c_{t3}	1.29×10^{-5}	c_{t3}	5.98×10^{-5}	c_{t4}	1.52×10^{-5}

Table A.15: Sobol indices for integrated quantities with unstr-f grid, SA model (BCFD).

C_L		$C_{D_{\text{press}}}$		$C_{D_{\text{sf}}}$	
Coefficient	Sobol Index	Coefficient	Sobol Index	Coefficient	Sobol Index
κ	7.12×10^{-1}	σ	5.39×10^{-1}	κ	6.54×10^{-1}
c_{v1}	1.21×10^{-1}	c_{w2}	2.17×10^{-1}	σ	2.09×10^{-1}
σ	8.54×10^{-2}	c_{b1}	1.86×10^{-1}	c_{w2}	8.82×10^{-2}
c_{b1}	7.16×10^{-2}	c_{v1}	3.00×10^{-2}	c_{v1}	3.76×10^{-2}
c_{w2}	1.00×10^{-2}	κ	2.89×10^{-2}	c_{b1}	1.29×10^{-2}
c_{t4}	3.35×10^{-5}	c_{t4}	1.55×10^{-4}	c_{t3}	3.23×10^{-5}
c_{t3}	2.72×10^{-5}	c_{t3}	1.48×10^{-4}	c_{t4}	1.46×10^{-5}

Table A.16: Sobol indices for integrated quantities with original medium grid, SA model, $f_{t2} = 0$ (FUN3D).

C_L		$C_{D_{\text{press}}}$		$C_{D_{\text{sf}}}$	
Coefficient	Sobol Index	Coefficient	Sobol Index	Coefficient	Sobol Index
κ	7.28×10^{-1}	σ	4.98×10^{-1}	κ	6.53×10^{-1}
c_{v1}	1.19×10^{-1}	c_{w2}	2.27×10^{-1}	σ	2.11×10^{-1}
c_{b1}	7.36×10^{-2}	c_{b1}	2.14×10^{-1}	c_{w2}	8.71×10^{-2}
σ	7.15×10^{-2}	κ	3.39×10^{-2}	c_{v1}	3.79×10^{-2}
c_{w2}	8.69×10^{-3}	c_{v1}	2.84×10^{-2}	c_{b1}	1.29×10^{-2}
c_{t4}	1.09×10^{-4}	c_{t3}	1.51×10^{-4}	c_{t3}	3.06×10^{-5}
c_{t3}	5.38×10^{-5}	c_{t4}	1.37×10^{-4}	c_{t4}	1.33×10^{-5}

Table A.17: Sobol indices for integrated quantities with fine grid, SA model, $f_{t2} = 0$ (FUN3D).

C_L		$C_{D_{\text{press}}}$		$C_{D_{\text{sf}}}$	
Coefficient	Sobol Index	Coefficient	Sobol Index	Coefficient	Sobol Index
κ	7.21×10^{-1}	σ	5.10×10^{-1}	κ	6.53×10^{-1}
c_{v1}	1.20×10^{-1}	c_{w2}	2.24×10^{-1}	σ	2.10×10^{-1}
σ	7.89×10^{-2}	c_{b1}	2.03×10^{-1}	c_{w2}	8.76×10^{-2}
c_{b1}	7.18×10^{-2}	κ	3.51×10^{-2}	c_{v1}	3.79×10^{-2}
c_{w2}	9.30×10^{-3}	c_{v1}	2.96×10^{-2}	c_{b1}	1.28×10^{-2}
c_{t4}	2.46×10^{-5}	c_{t4}	9.24×10^{-5}	c_{t3}	3.05×10^{-5}
c_{t3}	1.17×10^{-5}	c_{t3}	4.30×10^{-5}	c_{t4}	1.42×10^{-5}

APPENDIX B

Epistemic Intervals of Integrated Quantities (Case Study)

This appendix includes the tabulated epistemic intervals for C_L and C_D with each of the case study grids, turbulence models, and flow solvers.

Table B.1: Epistemic intervals for C_L (Case study).

		Baseline	Min	Max
coarse	SA	0.735	0.724	0.750
	W2006	0.742	0.730	0.747
	SST	0.738	0.669	0.809
fine	SA	0.746	0.681	0.862
	W2006	0.742	0.731	0.747
	SST	0.744	0.708	0.776
med-tri	SA	0.730	0.708	0.758
	W2006	0.743	0.730	0.749
	SST	0.739	0.707	0.782
unstr-m	SA	0.748	0.739	0.775
	W2006	0.746	0.737	0.753
	SST	0.749	0.714	0.781
bcfd-med	SA	0.738	0.729	0.753
bcfd-unstr-m	SA	0.733	0.724	0.747
bcfd-unstr-f	SA	0.734	0.725	0.748
*orig. med.	SA	0.744	0.735	0.758
*fine	SA	0.746	0.737	0.760

*indicates a FUN3D analysis with f_{t2} set to zero

Table B.2: Epistemic intervals for C_D, given in drag counts (Case study).

		Baseline	Min	Max
coarse	SA	147.1	137.8	153.6
	W2006	142.8	129.5	144.7
	SST	128.6	76.2	194.9
fine	SA	146.0	126.0	155.8
	W2006	142.8	129.8	144.0
	SST	128.6	109.7	183.9
med-tri	SA	141.4	128.4	147.5
	W2006	142.7	129.1	144.2
	SST	126.9	116.7	188.0
unstr-m	SA	148.0	136.0	156.3
	W2006	143.8	131.7	145.8
	SST	131.7	111.1	184.3
bcfd-med	SA	153.8	145.2	160.8
bcfd-unstr-m	SA	152.0	142.9	158.2
bcfd-unstr-f	SA	151.9	142.7	158.3
*orig. med.	SA	146.0	137.3	152.0
*fine	SA	146.0	137.0	152.2

*indicates a FUN3D analysis with f_{t2} set to zero

BIBLIOGRAPHY

[1] "NASA Langley Research Center Turbulence Modeling Resource," http://turbmodels.larc.nasa.gov [retrieved April 2015].

[2] Hosder, S., Walters, R. W., and Balch, M., "Point-Collocation Nonintrusive Polynomial Chaos Method for Stochastic Computational Fluid Dynamics," *AIAA Journal*, Vol. 48, No. 12, December 2010.

[3] Sudret, B., "Global sensitivity analysis using polynomial chaos expansion," *Reliability Engineering and System Safety*, Vol. 93, No. 7, 2008, pp. 964-979.

[4] Slotnick, J., Khodadoust, A., Alonso, J., Darmofal, D., Gropp, W., Lurie, E., and Mavriplis, D., "CFD Vision 2030 Study: A Path to Revolutionary Computational Aerosciences," NASA/CR-20140218178, March 2014.

[5] Godfrey, A. G., and Cliff, E. M., "Sensitivity Equations for Turbulent Flows," AIAA Paper 2001-1060, January 2001.

[6] Hosder, S., Grossman, B., Haftka, R. T., Mason, W. H., Watson, L. T., "Quantitative relative comparison of CFD simulation uncertainties for a transonic diffuser problem," *Computers and Fluids*, Vol. 35, pp. 1444-1458, August 2005.

[7] West, T. K. and Hosder, S., "Uncertainty Quantification of Hypersonic Reentry Flows with Sparse Sampling and Stochastic Expansions," *Journal of Spacecraft and Rockets*, Vol. 52, No. 1, January-February 2015, pp. 120-133.

[8] Adya, S., Han, D., and Hosder, S., "Uncertainty Quantification Integrated to the CFD Modeling of Synthetic Jet Actuators," AIAA Paper 2010-4411, June-July 2010.

[9] Hosder, S., Walters, R. W., and Balch, M., "Efficient Uncertainty Quantification Applied to the Aeroelastic Analysis of a Transonic Wing," AIAA Paper 2008-729, January 2008.

[10] Najm, H. N., "Uncertainty Quantification and Polynomial Chaos Techniques in Computational Fluid Dynamics," *Annual Review of Fluid Mechanics*, Vol. 41, pp. 35-52, 2009.

[11] Ghanem, R. G. and Spanos, P. D., "Stochastic Finite Elements: A Spectral Approach," Springer-Verlag, New York, 1991.

[12] Eldred, M. S., "Recent Advances in Non-Intrusive Polynomial Chaos and Stochastic Collocation Methods for Uncertainty Analysis and Design," AIAA Paper 2009-2274, May 2009.

[13] Edeling, W. N., Cinnella, P., and Dwight, R. P., "Predictive RANS Simulations via Bayesian Model-Scenario Averaging," *Journal of Computational Physics*, Vol. 275, June-July 2014, pp. 65-91.

[14] Papadimitriou, D. I. and Papadimitriou, C., "Bayesian uncertainty quantification of turbulence models based on high-order adjoint," *Computers and Fluids*, Vol. 120, pp. 82-97, July 2015.

[15] Levy, D. M., Zickuhr, T., Vassberg, J., Agarwal, S., Wahls, R. A., Pirzadeh, S., and Hemsch, M. J., "Data Summary from the First AIAA Computational Fluid Dynamics Drag Prediction Workshop," *AIAA Journal of Aircraft*, Vol. 40, No. 5, September-October 2003.

[16] Spalart, P. R. and Allmaras, S. R., "A One-Equation Turbulence Model for Aerodynamic Flows," *Recherche Aerospatiale*, No. 1, 1994, pp. 5-21.

[17] Wilcox, D. C., "Formulation of the k-omega Turbulence Model Revisited," *AIAA Journal*, Vol. 46, No. 11, 2008, pp. 2823-2828.

[18] Menter, F. R., "Two-Equation Eddy-Viscosity Turbulence Models for Engineering Applications," *AIAA Journal*, Vol. 32, No. 8, August 1994, pp. 1598-1605.

[19] Biedron, R. T., Derlaga, J. M., Gnoffo, P. A., Hammond, D. P., Jones, W. T., Kleb, B., Lee-Rausch, E. M., Nielsen, E. J., Park, M. A., Rumsey, C. L., Thomas, J. L., and Wood, W. A., "FUN3D Manual: 12.4," NASA/TM-2014-218179, March 2014.

[20] Bachalo, W. D. and Johnson, D. A., "Transonic, Turbulent Boundary-Layer Separation Generated on an Axisymmetric Flow Model," *AIAA Journal*, Vol. 24, No. 3, 1986, pp. 437-443.

[21] Cook, P.H., McDonald, M.A., and Firmin, M.C.P., "Aerofoil RAE 2822 - Pressure Distributions, and Boundary Layer and Wake Measurements," *Experimental Data Base for Computer Program Assessment*, AGARD Report AR 138, 1979.

[22] Nee, V. W. and Kovasznay, L. S. G., "The Calculation of the Incompressible Turbulent Boundary Layer by a Simple Theory," *Physics of Fluids*, Vol. 12, 1968, pp. 473.

[23] Bailey, S. C. C., Vallikivi, M., Hultmark, M., and Smits, A. J., "Estimating the value of von Kármán's constant in turbulent pipe flow," *Journal of Fluid Mechanics*, Vol. 749, 2014, pp. 79-98.

[24] Email correspondence between Philippe Spalart and John Schaefer, June-December 2014.

[25] Wilcox, D. C., *Turbulence Modeling for CFD*, 3rd edition, DCW Industries, Inc., La Cañada CA, 2006.

[26] Email correspondence between David Wilcox and John Schaefer, June 2014.

[27] Georgiadis, N. J. and Yoder, D. A., "Recalibration of the Shear Stress Transport Model to Improve Calculation of Shock Separated Flows," AIAA Paper 2013-0685, January 2013.

[28] Email correspondence between Florian Menter and John Schaefer, June 2014.

[29] Hosder, S., Walters, R. W., and Balch, M., "Efficient Sampling for Non-Intrusive Polynomial Chaos Applications with Multiple Input Uncertain Variables," AIAA-Paper 2007-1939, April 2007.

[30] Crestaux, T., Maitre, O. L., and Martinez, J.-M, "Polynomial chaos expansion for sensitivity analysis," *Reliability Engineering and System Safety*, 2009.

[31] Ghaffari, S., Magin, T., and Iaccarino, G., "Uncertainty Quantification of Radiative Heat Flux Modeling for Titan Atmospheric Entry," AIAA Paper 2010-239, January 2010.

[32] Mani, M., Rider, B. J., Sclafani, A. J., Winkler, C., Vassberg, J., Dorgan, A. J., Cary, A., and Tinoco, E. N., "RANS Technology for Transonic Drag Prediction: A Boeing Perspective of the 4th Drag Prediction Workshop," AIAA Paper 2010-4221, June 2010.

VITA

John Schaefer was born and raised in St. Louis, Missouri. He attended Lindbergh High School, where he graduated in 2010. In August of 2010 he began his collegiate career at the Missouri University of Science and Technology. As an undergraduate student, he was awarded a fellowship from the NASA Aeronautics Scholarship Program. In May of 2014 he graduated Summa Cum Laude with a Bachelor of Science degree in Aerospace Engineering. John was dual-enrolled in graduate school during the senior year of his B.S. degree, and he graduated with a Master of Science degree in Aerospace Engineering from the Missouri University of Science and Technology in December of 2015. During his time as a student he was involved in several organizations, including the Sigma Gamma Tau aerospace honors society and the Advanced Aero Vehicle Group student design team. In the summer semesters John participated in internship programs at the NASA Dryden (now Armstrong) Flight Research Center in Edwards, California; the NASA Langley Research Center in Hampton, Virginia; and The Boeing Company in St. Louis, Missouri. John was the first author on a conference paper published by The American Institute of Aeronautics and Astronautics in June 2015. He began working as a full time employee at The Boeing Company in St. Louis, Missouri in early 2016.